Mechanistic Studies of Rh(diphosphine)-Catalyzed Methanol Reductive Carbonylation

By

Sucheewin Chotchatchawankul

A dissertation submitted in partial fulfillment

of the requirements for the degree of

Doctor of Philosophy

(Chemistry)

at the

UNIVERSITY OF WISCONSIN – MADISON

2015

Date of final oral examination: 1/6/2015

The dissertation is approved by the following members of the Final Oral Committee:
Clark R. Landis, Professor, Inorganic Chemistry
Shannon S. Stahl, Professor, Inorganic Chemistry
Steven D. Burke, Professor, Organic Chemistry
Eric R. Strieter, Assistant Professor, Organic Chemistry
Jennifer M. Schomaker, Assistant Professor, Organic Chemistry

Table of Contents

Table of Figures

Table of Schemes

Table of Tables

Acknowledgments

I would like to thank my advisor, Professor Clark Landis, who helped me not only with my research project, but also my professional development. Clark encouraged me to take initiative while always guided me back when my proposal started to stray to the wrong direction. I learned a lot from Clark's incredible skill of being able to simplify and clarify complicated and difficult subjects, and was inspired to be a teacher as great as him. Landis group members, both previous and current, have provided me with supporting and entertaining working environment. Dr. Nicholas Beach builded the complicated WiHP-NMRR that is indispensable for my project. Dr. Spring Knapp has never stopped making the system easier and more pleasant to use. At the very end, Spring spent a lot of time to make this thesis more complete and readable. Anna Dunn also helped with the thesis editing, in addition to delighting me with her high-pitched laugh. Gene Wong will always be in my memory as a great mentor and a friend. Dr. Charlie Fry taught me everything from the basic NMR principles to how to set up very complicated experiments, and has never been tired of explaining.

The distance did not matter for Mom and Dad for being so supportive, understanding and great listeners when I complained about life and grad school. All my Thai friends in Madison made me feel like home from time to time. I would not graduate without a tremendous help from Annie Chantarojsiri who kept me laugh during the tough times.

Abstract

A chemical reaction involving carbon chain elongation from C_1 building blocks is a promising alternative to petroleum-based chemical production because it allows a wider range of carbon sources, including renewable biomass. Methanol reductive carbonylation (MRC) produces ethanol from synthesis gas, a mixture of H_2 and CO, and methanol, which is also produced from synthesis gas. Prior to the 1990s, industry-scale MRC was inhibited by the ineffectiveness of the existing catalysts. Wegman and Moloy reported that a Rh(dppp) complex (dppp = 1,3-bis(diphenylphosphino)propane) catalyzed MRC to above 80% selectivity at only 1000 psi of synthesis gas – relatively milder conditions than typical Co-based catalysts. Their proposed mechanism for Rh-catalyzed methanol carbonylation is not consistent with the recent observations that the catalytic rate is inhibited by iodide ions and CO. Additionally, dppp-based ligands modified with *ortho*-alkoxy groups on the phenyl rings have been found to perform better than the original dppp. Herein, we propose and explore a mechanism based on a Rh-catalyzed hydroformylation via a Rh-H intermediate. Interception of the proposed intermediates was not successful, but characterization of related complexes allows us to conclude that the reaction at ambient pressure and temperature occurs via formation of Rh-dppp dimeric species. That the essential hydrogenolysis step of this hydride mechanism does not occur under high pressure of synthesis gas further precludes the proposed mechanism from being operational. We then explore an alternative mechanism involving a cationic intermediate formed from dissociation of the iodide ligand. In order to study the reaction under high pressure, a recently developed high pressure NMR apparatus was utilized. Kinetic measurements of the reaction agree with the model where the reaction was inhibited by accumulated iodide ions produced in the reaction. The rate measurement

also demonstrates that the hydrogenolysis of the Rh-complex is rate-determining step and is where the Rh-dppp and Rh-dpppOEt (dpppOEt = 1,3-bis(di-2-ethoxyphenylphosphino)propane) catalysts are different, in accordance to the hypothesis that the *ortho*-alkoxy group promotes the ionization. Finally, we were able to directly observe Rh-dpppOEt ionized species with coordinating alkoxy group and propose a complete ionization-based mechanism based on these observations.

Chapter 1

Catalytic Methanol Reductive Carbonylation

1.1 Introduction

The ongoing depletion of petroleum reserves raises concerns about future sources of long-chain hydrocarbons. One solution is to synthesize longer carbon chains by the homologation of readily available "C_1" and "C_2" (one carbon and two carbon, respectively) sources such as methane, carbon monoxide, carbon dioxide, and ethanol. Especially attractive are renewable sources of carbon building blocks. For example, ethylene synthesis from ethanol, a "C_2" source, produced by sugar fermentation is economically favorable under some conditions. However, the fermentation is not cost-effective in many localities because of limited growing seasons, the cost of transporting large amounts of biomass, and energy-intensive distillation from low concentration aqueous media.[1,2]

Synthesis gas, a 1:1 mixture of CO and H_2, is an attractive source of both C_1 and reducing equivalents because it can be generated by gasification of a variety of sources, including renewable biomass.[2,3] One route to C_2 compounds from C_1 compounds is carbonylation of methanol (which can be made from hydrogen-rich synthesis gas) to form acetic acid, methyl acetate, and acetic anhydride. Methanol carbonylation is currently performed on commodity scale (17 B pounds per year) using the catalytic process generally referred to as the acetic acid process. However, formation of C_2 hydrocarbon products, such as ethanol, requires methanol reductive carbonylation (MRC), by which C-O bonds are converted into C-H bonds.[4]

Scheme 1.1. Catalytic methanol reductive carbonylation (MRC)

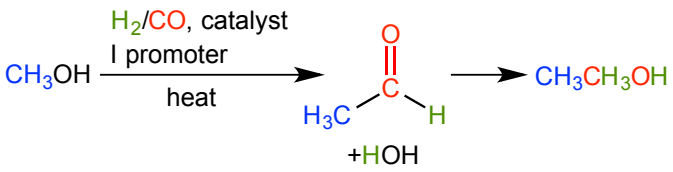

The simplest reductive carbonylation process converts methanol into ethanol in the presence of synthesis gas, with acetaldehyde as the critical intermediate. This process has not been commercialized due to limitations of the current processes.[§] For example, the low activity of the current reductive carbonylation catalysts requires high reaction pressures that increase the cost of production. Moreover, under these forcing conditions, product selectivity is poor, generating a mixture of compounds, including a variety of alcohols, ethers, and esters. The following sections provide a brief overview of catalytic systems that have been developed and studied for reductive carbonylation of alcohols.[4–6]

1.2 Co-Catalyzed Methanol Reductive Carbonylation

The first catalytic process for reductive carbonylation of methanol was reported by Wender et al. in 1951.[7] In this pioneering work, treatment of alcohols with synthesis gas under conditions similar to hydroformylation produces the homologous alcohol; the catalysts employed were $Co(OAc)_2$ or $[\{Co(CO)_4\}_2]$ at 160 – 185 °C and 3200 – 5100 psi of 1:1 H_2/CO. The carbonylation of methanol, which was found to react more rapidly than larger primary and secondary alcohols, produced only 39% yield of ethanol after 4 h along with esters, higher alcohols, and methane. Following this seminal work, numerous patents and publications reported modifications and studies based on this original system.[8–15]

1.2.1 Modifications and improvements on Co-catalysts

Berty et al. improved catalytic reductive carbonylation by introducing CH_3I as a promoter. Addition of methyl iodide to the cobalt-catalyzed process effected a three- to five-

[§] Thermodynamically, the process of converting synthesis gas to ethanol is more favorable than that of converting synthesis gas to methanol.[4]

fold increase in reaction rate at the same methanol conversion. It was found that I_2 and a number of iodide salts were effective promoters, with their role attributed to the conversion of methanol to more reactive CH_3I. The drawback of utilizing iodine promoters is increased acid/ester formation. In addition, too high of a I: Co ratio can decrease the reaction selectivity.[16–19]

Phosphine ligands also improve the Co-based catalysis. Although ligands reduce the catalyst activity in many systems, they significantly increase the selectivity to acetaldehyde or acetal products. In combination with iodine promoters, the catalytic activity can be kept at an acceptable level. For example, Loevenich determined that when triphenylphosphine was added to $Co(OAc)_2$ catalyst in a 3:1 ratio in the presence of HI, the molar selectivity toward ethanol/acetaldehyde/acetals was improved from 66.4% to 71.3%, while acetate and ether formation was reduced from 27.2% to 12.1%.[20,21]

Because the formation of ethanol is believed to proceed through acetaldehyde as an intermediate, combination of an MRC catalyst with an aldehyde hydrogenation catalyst improves selectivity for ethanol formation. Ruthenium salts were found to perform better than other metal co-catalysts, with complete conversion of acetaldehyde to ethanol, while acetaldehyde was present around 22 – 37 mol% of products in absence of co-catalyst or in presence of other metal co-catalysts.[22] However, the selectivity toward acetaldehyde and ethanol combined were not substantially different, suggesting that the sole role of the hydrogenation catalyst was to promote conversion of aldehyde to alcohol. Introduction of the second metal in the form of bimetallic clusters were also studied. It was found that $[Et_4N][RuCo_3(CO)_{12}]$ gave the best selectivity among other noble metals including Pd, Pt, and Rh. Interestingly, $[Bu_4N][FeCo_3(CO)_{12}]$ was also improved the activity and selectivity

over monometallic [$Fe(CO)_5$] or [$Co_2(CO)_8$], but the evidence suggested that this might be merely a stabilization effect (see below).[23]

In spite of many modifications—changing Co precursors, adding phosphine ligands, introducing iodine promoters, or using bimetallic systems, the activity and selectivity of the catalysts were still low. Acetic acid, esters, ethers and higher alcohols were also observed in the product mixture and the reactions required prohibitively high operating pressure, usually 3000-10000 psi of synthesis gas, rendering the process commercially unattractive.[5]

1.2.2 Mechanisms of Co-catalyzed MRC

Scheme 1.2. Proposed mechanism for non-promoted Co-catalyzed MRC

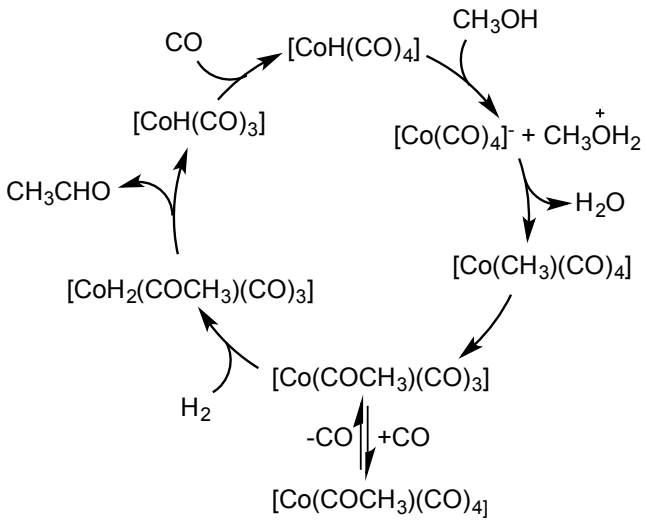

The generally accepted mechanism of the non-promoted Co-catalyzed MRC is based on a [$CoH(CO)_4$] active species (Scheme 1.2). The acidic hydride complex protonates MeOH followed by nucleophilic attack on the methyl group in an S_N2 fashion to form [$Co(CH_3)(CO)_4$]. Migratory insertion of CO into the Co-methyl bond, followed by coordination of another CO generates an off-cycle Co-acetyl complex, [$Co(COCH_3)(CO)_4$]. Dissociation of a CO ligand from the Co-acetyl complex allows oxidative addition of H_2 to form the dihydrido Co-acetyl complex, [$CoH_2(COCH_3)(CO)_3$], which undergoes reductive

elimination of acetaldehyde to regenerate $[CoH(CO)_4]$.[14]

Scheme 1.3. Proposed mechanism of iodine-promoted Co-catalyzed MRC.

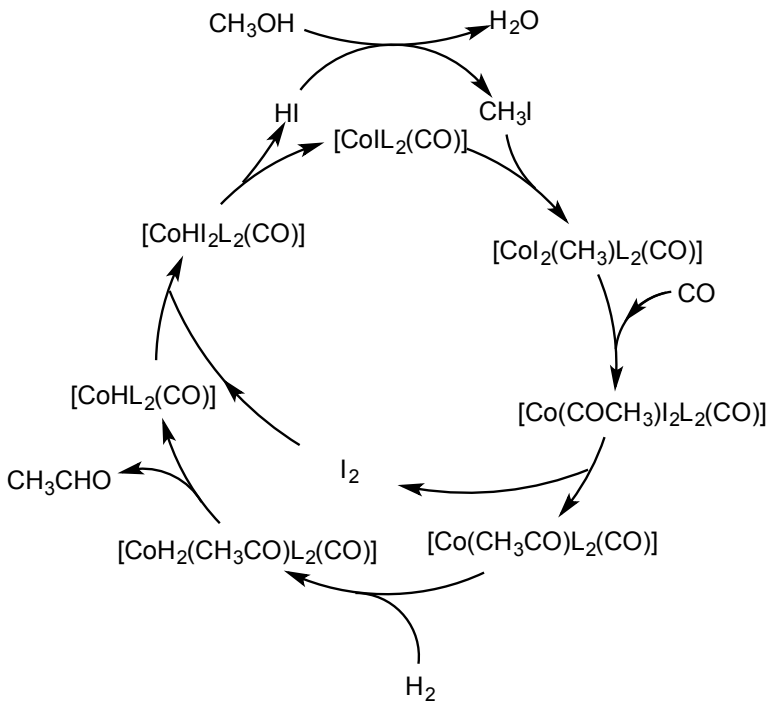

The mechanism for the iodine-promoted cobalt-catalyzed MRC, proposed by Roper and Loevenich, is shown in Scheme 1.3. The main difference between this mechanism and the non-promoted mechanism is that CH_3I, which is generated from methanol and the added iodine, undergoes oxidative addition to the Co active species, $[CoIL_2(CO)]$. In this proposal, reductive elimination of I_2 occurs prior to H_2 oxidative addition in order to free up a coordination site and reduce Co center to Co^I. The I_2 is reincorporated into the complex via oxidative addition to the Co-hydrido species after the product forming step.[5]

1.3 Rh-catalyzed methanol reductive carbonylation

Rhodium complexes are excellent catalysts for synthesis gas related reactions, including methanol carbonylation and olefin hydroformylation. In rhodium-catalyzed hydroformylation, two prominent steps are (1) insertion of CO into a Rh-alkyl bond to form a Rh-acyl complex and (2) reaction of the acyl complex with H_2 leads to aldehyde product (Scheme 1.4). These two steps are essential to aldehyde formation in MRC, making Rh-based catalyst very promising.

Scheme 1.4. Simplified catalytic cycles of Rh-catalyzed methanol carbonylation (left) and olefin hydroformylation (right) showing elementary steps related to MRC.

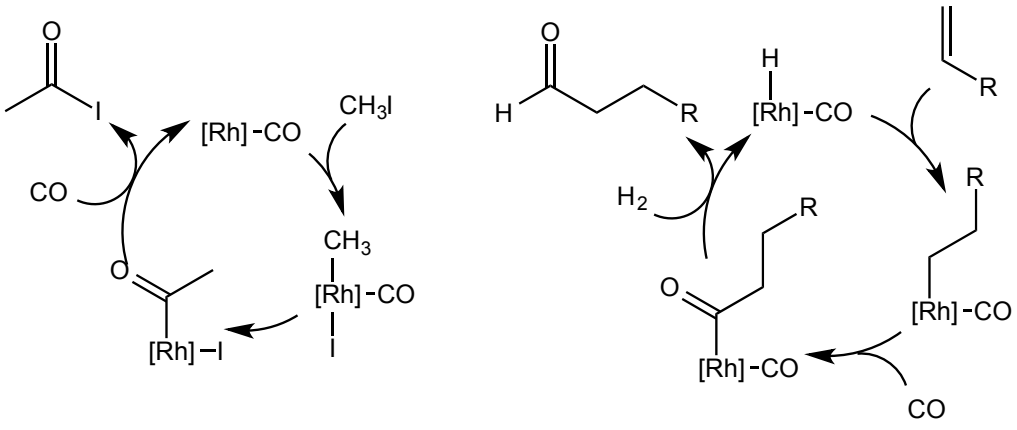

Because the Rh-based catalysts are very selective for carbonylation to form acetic acid, the initial work by Dumas et al. used an extremely high H_2: CO ratio of 40:1 to shift the selectivity toward ethanol with total pressure not much lower than those in the Co-catalyzed system.[24] In 1989, Wegman and Moloy reported a modified system using Rh(diphosphine)/Ru catalyst system with a CH_3I promoter.[25] Similar to the Co bimetallic s ystems, the role of Ru is to catalyzes the hydrogenation of acetaldehyde to ethanol whereas the Rh catalyst is responsible for converting methanol to acetaldehyde. With the best

performing ligand, 1,3-bis(diphenylphosphino)propane (dppp), greater than 80% selectivity for the reductive carbonylation products (ethanol and acetaldehyde) was observed using 1000 psi 2:1 H_2/CO at 140 °C in 4 h, conditions milder than typical Co-catalyzed reactions.

1.3.1 Mechanism of Rh-catalyzed MRC

Mechanistic studies by Wegman and Moloy led to the proposed catalytic cycle shown in Scheme 1.5. This cycle is similar to the Monsanto acetic acid process where CH_3I undergoes oxidative addition to unsaturated Rh-I complex **1-I**[*], yielding iodo Rh-methyl complex **2-Me.** Migratory insertion of CO into the Rh-CH_3 bond yields diiodo Rh-acetyl complex **3-Ac**. This Rh-acetyl complex, believed to be the key intermediate at the rate- and selectivity-determining step, branches to either a) CO coordination and reductive elimination of CH_3COI which eventually becomes the acetic acid side product or b) hydrogenolysis by H_2 to form acetaldehyde and $[\{RhHI_2(dppp)\}_2]$ dimer , followed by HI elimination and CO coordination to regenerate the catalytic species.

[*] The naming scheme **A-X-B$_L$** is used throughout this thesis, where **A** denotes isotope labeling (**D** = ^{2}H, **^{13}C** = carbon-13, absence = natural isotope) on methyl group of Rh-methyl or Rh-acetyl complexes, **X** is the unique number given to each type of complex, **L** denotes diphosphine ligand (**OEt** = 1,3-bis(di-2-ethoxyphenylphosphino)propane (dpppOEt), absence = dppp), and **B** denotes specific ligand variation of the complex. For example, **D-2-Ac$_{OEt}$** is $[RhI_2(COCD_3)(CO)(dpppOEt)]$.

Scheme 1.5. Proposed mechanism of Rh-catalyzed MRC.

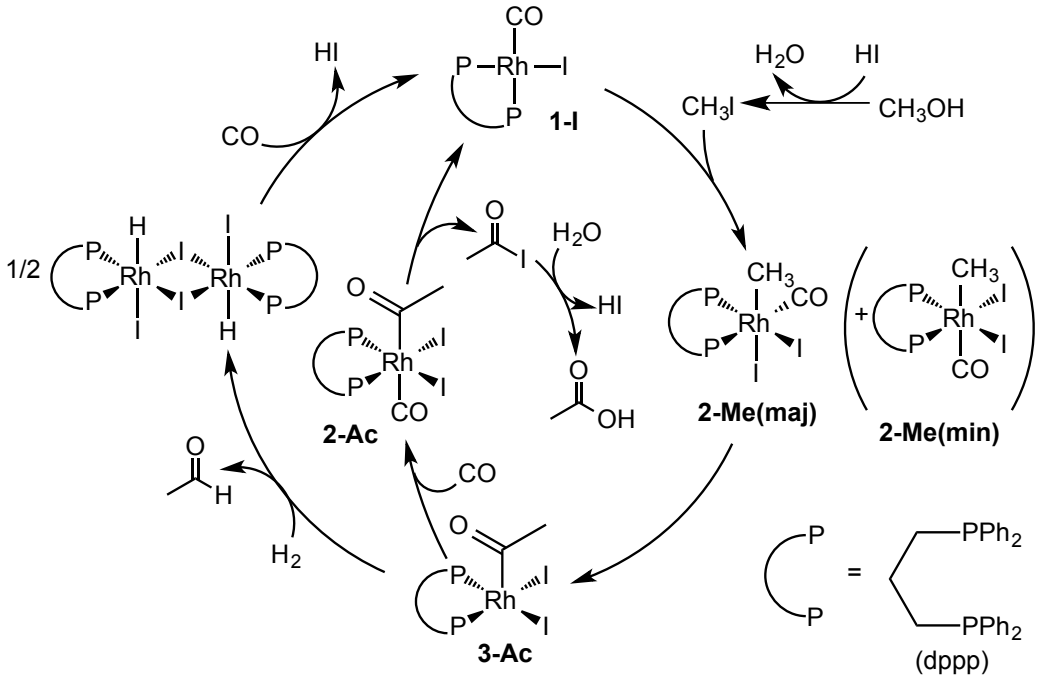

1.4 Our research questions

Rh catalysis is promising in terms of practicality for industry due to gentler reaction conditions used. However, the activity and selectivity of these catalysts still needs improvement. Achieving a fundamental knowledge of the mechanism is essential to the development of better catalysts. Although the proposed catalytic cycle by Wegman and Moloy (Scheme 1.5) forms a good basis for the possible mechanism, parts of the proposal are not clearly understood, especially the hydrogenolysis of **3-Ac**. Unlike a Rh^{I} complex, oxidative addition of H_2 to a Rh^{III} center seems unlikely. Hydrogenolysis may proceed by sigma bond metathesis of dihydrogen coordinated a $[RhI_2(COCH_3)(H_2)(dppp)]$ complex, but computational studies indicate that the energy barrier is so high that the selectivity would favor acetic acid formation. Rate studies by Wegman and Moloy showed zero order kinetics on the concentration of CH_3I and first order dependence on the concentration of **3-Ac** but the

dependencies of the reaction rate on H_2 and CO were not determined. This is unfortunate because these rate dependencies would clarify the mechanism at the branching point between acetate and acetaldehyde formation. In the recent studies by our collaborators at Dow Chemical, dppp-derivatives were found to be significantly more active and selective than dppp. Reaction product analysis of one of the ligands revealed inhibition of acetaldehyde production by increased pressure of CO. In addition, their studies demonstrated inhibition by iodide ions. These inhibitive effects are not explained by the mechanism of Wegman and Moloy.[26,27]

Scheme 1.6. Mechanistic assumptions based on kinetic measurements by Wegman and Moloy‡

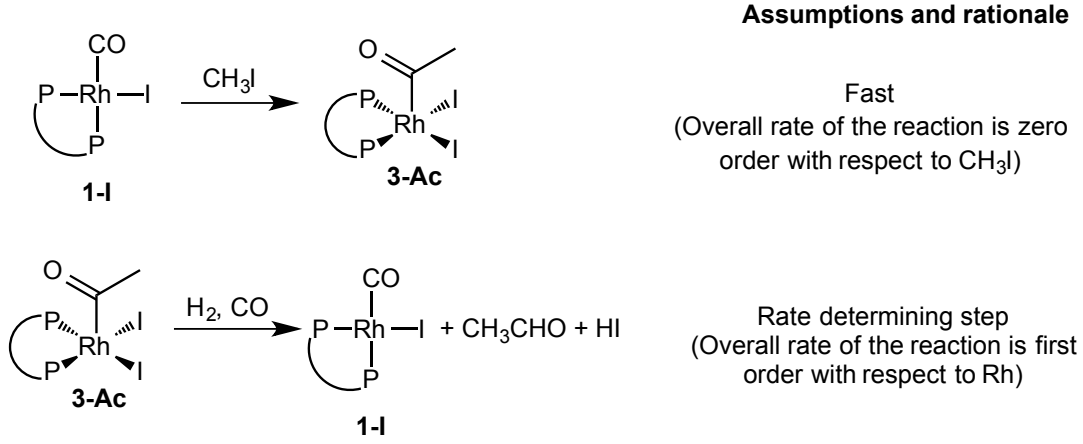

In this research project, we aim to uncover the elementary steps of the catalytic cycle, the reaction conditions affecting the performance of the catalyst, and the origin of the catalytic differences between different phosphine ligands. Our approach is to intercept and/or synthesize catalytic species, study their reactivity, and investigate their reaction kinetics investigation using the power of NMR spectroscopy.

‡ The rate dependencies with respect to H_2 and CO were not determined.

1.5 References

(1) Rostrup-Nielsen, J. R. *Science* **2005**, *308*, 1421–1422.

(2) Spath, P.; Dayton, D. Preliminary Screening — Technical and Economic Assessment of Synthesis Gas to Fuels and Chemicals with Emphasis on the Potential for Biomass-Derived Syngas; NREL/TP-510-34929: Golden, CO 2003.

(3) Ahmed, A.; White, A. M.; Hu, P.; Lewis, R. S.; Huhnke, R. L. Ethanol from Syngas — Microbial Conversion, 2008. SunGrant BioWeb. http://bioweb.sungrant.org/Technical/Biofuels/Technologies/Biofuels+from+Syngas/Ethanol+from+Syngas/Default.htm (accessed Aug 6, 2014)

(4) Subramani, V.; Gangwal, S. *Energy Fuels* **2008**, 814–839.

(5) Röper, M.; Loevenich, H. In *Catalysis in C1 Chemistry*; Keim, W., Ed.; Catalysis by Metal Complexes: Volume 4; Springer Netherlands: Dordrecht, Holland, 1983; pp. 105–134.

(6) Braca, G.; Raspolli Galletti, A. M.; Sbrana, G. In *Oxygenates by Homologation or CO Hydrogenation with Metal Complexes*; Braca, G., Ed.; Catalysis by Metal Complexes: Volume 16; Springer Netherlands: Dordrecht, Holland, 1993; pp. 89–190.

(7) Wender, I.; Friedel, R. A.; Orchin, M. *Science* **1951**, *113*, 206–207.

(8) Deluzarche, A.; Jenner, G.; Kiennemann, A.; Samra, F. A. *Erdöl und Kohle, Erdgas, Petrochemie* **1979**, *32*, 436–438.

(9) Bartish, C. Synthesis of Ethanol by Homologation of Methanol. U.S. Patent 4,171,461, Oct 16, 1979.

(10) Walker, W. E. Process for the Selective Homologation of Methanol to Ethanol. U.S. Patent 4,277,634, Jul 7, 1981.

(11) Fakley, M. E.; Head, R. A. *Appl. Catal.* **1983**, *5*, 3–18.

(12) Lin, J.-J.; Knifton, J. F. Synthesis of Ethanol by Homologation of Methanol. U.S. Patent 4,374,285, Feb 15, 1983.

(13) Ziesecke, K. H. *Brennstoff-Chemie* **1952**, *33*, 385–397.

(14) Wender, I. *Catal. Rev.* **1976**, *14*, 97–129.

(15) Sheldon, R. A. In *Chemicals from Synthesis Gas - Catalytic Reactions of CO and H2*; Catalysis by Metal Complexes; Springer Netherlands: Dordrecht, Holland, 1983; pp. 149–153.

(16) Berty, J.; Marko, L.; Kallo, D. *Chem. Tech.–Leipzig* **1956**, *8*, 260–266.

(17) Bozik, J.; Kobylinski, T.; Pretzer, W. R. Ethanol from Methanol. U.S. Patent 4,239,924, Dec 16, 1980.

(18) Pretzer, W. R.; Kobylinski, T. P. *Ann. N. Y. Acad. Sci.* **1980**, *333*, 58–66.

(19) Mizoroki, T.; Nakayama, M. *Bull. Chem. Soc. Jpn.* **1964**, *37*, 236–241.

(20) Loevenich, H. Dissertation, Rheinisch-Westfalisch Technische Hochschule Aachen, 1982.

(21) Sugi, Y.; Bando, K.; Takami, Y. *Chem. Lett.* **1981**, 63–64.

(22) Pretzer, W. R.; Kobylinski, T. P.; Bozik, J. E. Selective Formation of Ethanol from Methanol, Hydrogen and Carbon Monoxide. U.S. Patent 4,133,966, Jan 9, 1979.

(23) Gerald, D. *J. Mol. Catal.* **1981**, *13*, 237–247.

(24) Dumas, H.; Levisalles, J.; Rudler, H. *J. Organomet. Chem.* **1979**, *177*, 239–244.

(25) Moloy, K. G.; Wegman, R. W. *Organometallics* **1989**, *8*, 2883–2892.

(26) Margl, P.; Klamo, S. B.; Patyk, R. A. Personal Communication.

(27) Clark, T. P.; Spinney, H.; Macdonald, J.; Cummins, C.; Klosin, J.; Briggs, J. Ligands

for Rhodium Catalyzed Reductive Carbonylation of Alcohols. PCT Int. Appl. WO 2013/096631 A1, Jun 27, 2013.

Chapter 2

Exploration of a Hydride Mechanism for Catalytic Methanol Reductive Carbonylation by Synthesis and Characterization of Rh(diphosphine) Complexes

2.1 Introduction

In this chapter, we explore an alternative mechanism, shown in Scheme 2.1, for the rhodium-catalyzed reductive carbonylation of methanol. Several parts of the mechanism show similarities to the mechanism originally proposed by Wegman and Moloy (Scheme 1.5). For example, the left pathway, which shows the activation of methyl iodide with [RhI(CO)(dppp)] (**1-I**), ultimately generating the byproduct acetic acid, is preserved due to the reported results that the isolated diiodo Rh-acetyl diiodide **3-Ac** can be employed as a catalyst. The new mechanistic hypothesis shows a different route to formation of acetaldehyde, where the only common intermediate between the acetaldehyde cycle and the acetic acid cycle is the monocarbonyl Rh-iodo complex **1-I**. Rather than reacting with methyl iodide, complex **1-I** instead undergoes hydrogenolysis to generate HI and the Rh-hydrido complex [RhH(CO)(dppp)] (**1-H**). In this mechanism, the observed inhibition of acetaldehyde formation by HI/I^- is attributed to elimination of HI in the hydrogenolysis step; an increase in HI/I^- in the solution disfavor hydrogenolys of 1-I to **1-H** plus HI less favorable in accordance with LeChatelier's principle. The hydride intermediate **1-H** can react with CO to form the off-cycle dicarbonyl Rh-hydrido species [$RhH(CO)_2$(dppp)] (**4-H**) as is commonly described in hydroformylation mechanisms. Shifting the equilibrium from **1-H** to the CO-saturated **4-H** would effectively inhibit oxidative addition of CH_3I to the complex, which is the necessary methyl iodide activation step. We note that **1-H** is a critical, highly reactive intermediate in rhodium-catalyzed hydroformylation reactions. Complex **1-H**, a Rh^I species, then undergoes oxidative addition with methyl iodide to form [$RhHI(CH_3)$(CO)(dppp)] (**5-Me**). Subsequent migratory insertion of CO into the Rh-Me bond and coordination of another CO yields the Rh-acetyl complex

[RhHI($COCH_3$)(CO)(dppp)] (**5-Ac**); reductive elimination of acetaldehyde regenerates the catalytic complex **1-I**. We note that the alternate mechanism requires that **1-I** be converted into the hydride **1-H**, thus entering into the acetaldehyde production cycle. Previously, it was found that the diiodo Rh-acetyl complex [$RhI_2(COCH_3)$(dppp)] (**3-Ac**) was the only Rh complex recovered from the catalysis. The abundance of **3-Ac** at the end of the reaction suggests that it is the primary thermodynamic sink; the question is whether it lies within the main cycle for producing acetaldehyde.

Scheme 2.1. Proposed hydride mechanism.

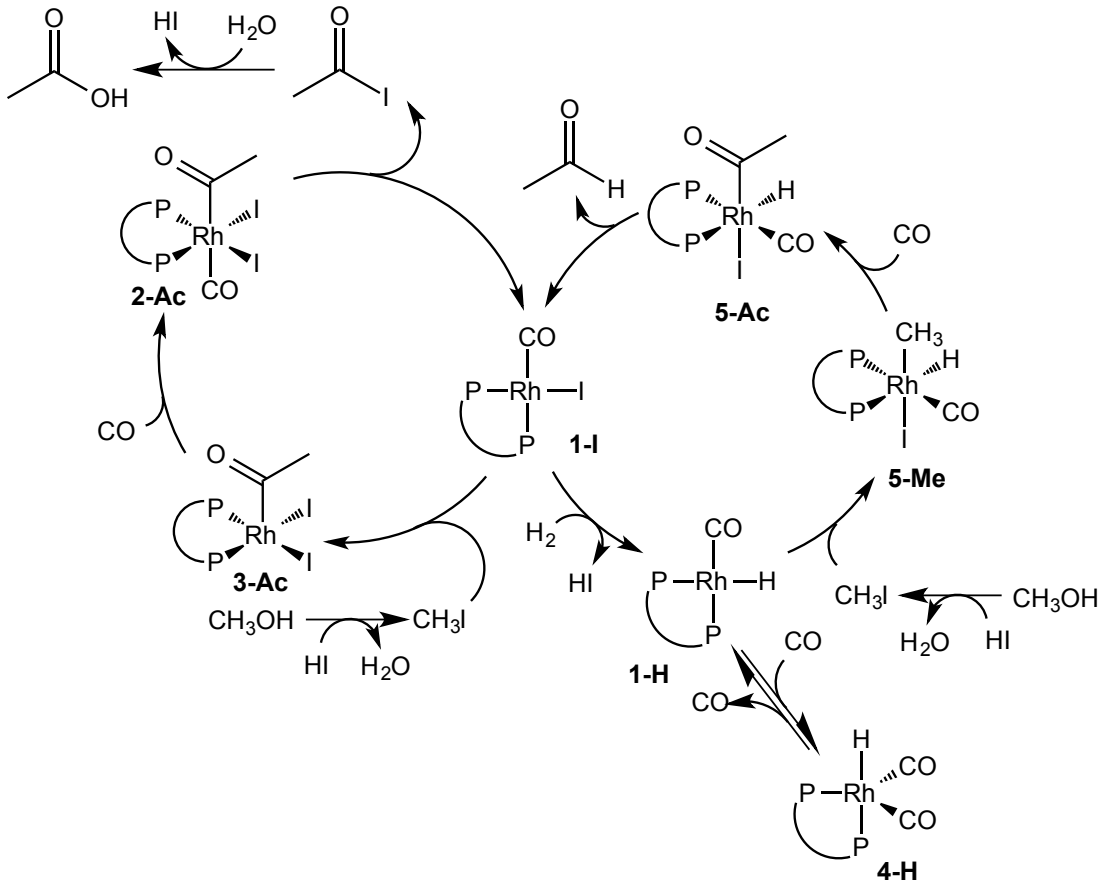

In this chapter we explore the viability of the alternative mechanism (Scheme 2.1) by empirical methods—using independent synthesis of related intermediates and monitoring their transformations by NMR spectroscopy.

2.2 Synthesis and Reactivity of Rh-H complex 4-H

*2.2.1 Synthesis and characterization of **4-H***

The dicarbonyl Rh-hydrido complex **4-H** was synthesized by addition of $KHBEt_3$ to the cationic Rh precursor $[Rh(CO)_2(dppp)]BF_4$ (**[1-CO]BF$_4$**) in CH_2Cl_2 at -78 °C under an atmospheric pressure of synthesis gas. The fluxionality of the trigonal bipyramidal complex observed by variable temperature NMR (VTNMR) experiment shows coalescence of ^{31}P signals from two very broad signals around δ 17 and 7 ppm at -80 °C to a broad doublet at δ 12.4 ppm at -50 °C (see Figure 2.1). The hydride signal in the ^1H NMR spectrum changes over the same range of temperature, from a doublet of doublets to a triplet of doublets with a corresponding change of the coupling constant $^2J_{H\text{-}P}$ from 110 Hz (hydride to *trans*-phosphorus) to 55 Hz (average of two phosphorus atoms); we note that the coupling of the hydride with the *cis* phosphorus at -80 °C is too small to be observable. The coalescence indicates slow exchange within the NMR time frame at -80 ºC and the two phosphorus atoms are distinguishable. There is a broad signal between two doublets of the hydride signal at the low temperature indicating incomplete freezing of the fluxional process.[1]

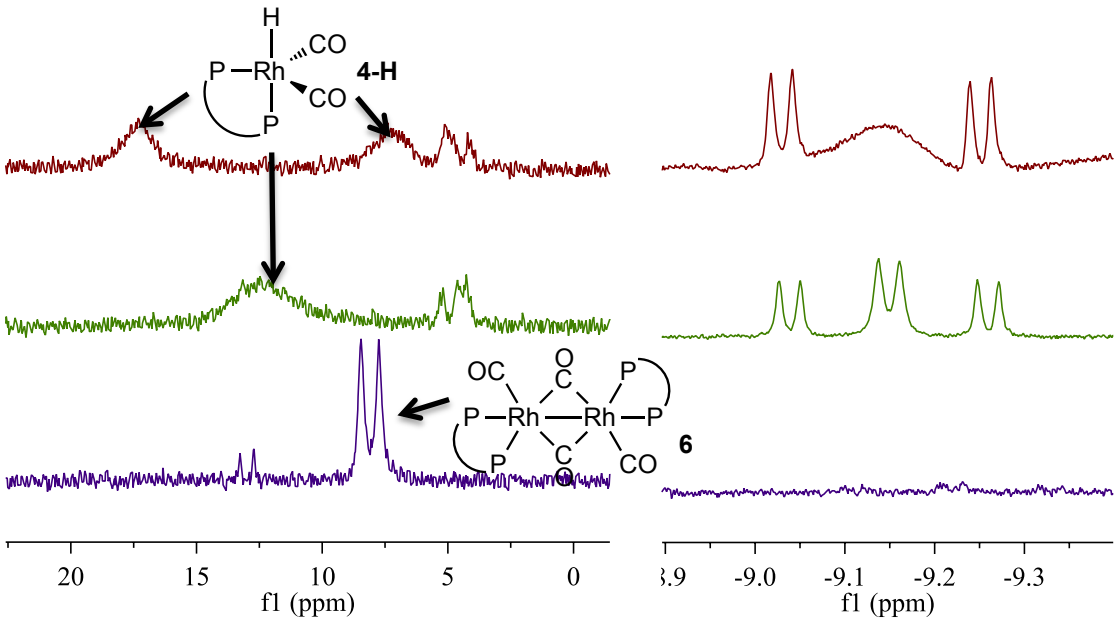

Figure 2.1. $^{31}P\{^{1}H\}$ NMR spectra (left) and hydride region in ^{1}H NMR spectra (right) of **1-H** at (a) -80 °C, (b) -50 °C, and (c) 24 °C (mostly converted to **6**) in CD_2Cl_2 under an atmospheric pressure of syngas.

The chemical shift and coupling constant $^{2}J_{H\text{-}P}$ of **4-H** have been reported previously only at low temperature (-5 to -30 °C). In this case, the complex was produced either by substitution of the PPh_3 ligand in $[RhH(CO)(PPh_3)_3]$ with dppp under an atmosphere of CO or by hydrogenolysis of [Rh(acac)(dppp)]under 300 psi of synthesis gas in a high pressure NMR apparatus.[2,3] We found that the complex has been observed only under those conditions because this type of complex is in equilibrium with a dinuclear complex $[\{Rh(CO)_2(dppp)\}_2]$ (**6**) through loss of H_2 as shown in Scheme 2.2.[4,5] It is also known that the equilibrium particularly favors the dimer with dppp type ligands at lower H_2 pressures. Castellanos-Páez *et al.* reported that under 75 psi of H_2 the Rh-hydrido complex with BDPP [(2S,4S)-bis(diphenylphosphine)pentane] ligand is present predominantly as the dimer.[1,6] Our reaction monitoring by VTNMR demonstrates that the conversion starts above -30 °C under atmospheric pressure of synthesis gas, and no hydrido complex was observed at room

temperature. For characterization purpose, we synthesized the dinuclear complex **6** by bubbling $RhH(dppp)_2$ complex with CO at room temperature in accordance with a previously reported method. The same dimer signal of AA′A″A‴XX′ type was observed in the final product as a doublet with slight difference in $^{1}J_{P\text{-}Rh}$ from the reported value. The only intermediate appears in NMR spectra is RhH(CO)(dppp)(dppp*) (where dppp* is dppp coordinating in monodentate fashion with the one phosphorus end dangling) suggesting rapid dimerization once the second CO has completely replaced dppp* ligand.[7,8]

Scheme 2.2. Dimerization of **4-H** and proposed pathway through **1-H**.

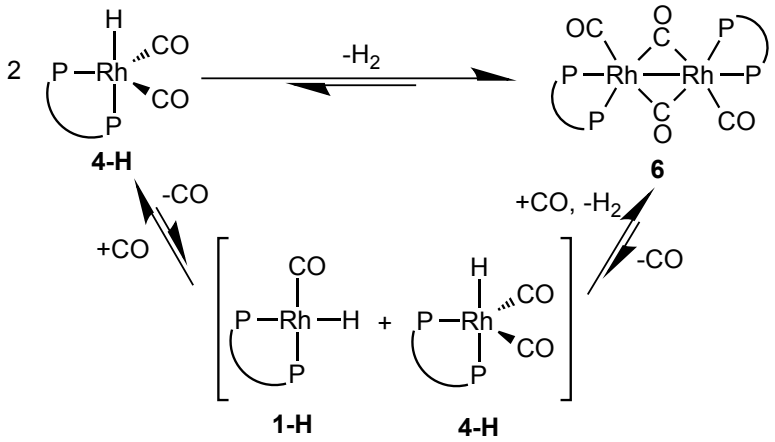

*2.2.2 Reactivity of the hydrido dicarbonyl complex **4-H** with CH_3I*

In order for the hydride mechanism to operate, the Rh-hydrido complex (**1-H** or **4-H**) must react with CH_3I to generate acetaldehyde. Excess CH_3I was added to hydrido dicarbonyl **4-H** at -30 °C under a synthesis gas atmosphere. Warming the sample up to room temperature generates acetaldehyde, acetone, methane, while only diiodo Rh-acetyl complex **3-Ac** was observed when the reaction completed. The complex **3-Ac** was proposed by Wegman and Moloy to be the key intermediate at the selectivity-determining step. However, we observe that the formation of the desired product, acetaldehyde, starts prior to formation of **3-Ac**, and this complex does not react further with synthesis gas. This result raises the

possibility that **3-Ac** is not required for acetaldehyde formation as originally proposed. In contrast, the result agrees with an alternate hypothesis in which acetaldehyde is generated from the reaction of the Rh-hydrido complex with CH_3I.

Scheme 2.3. The reaction of hydrido dicarbonyl **4-H** with CH_3I

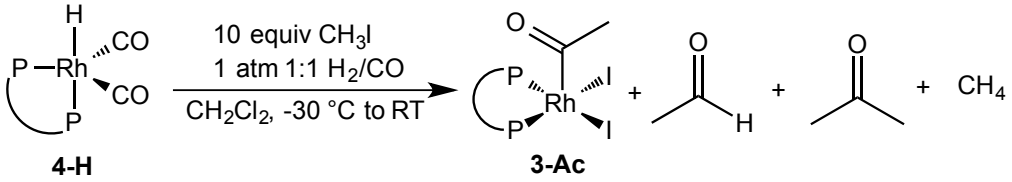

4-H **3-Ac**

2.3 Attempted Syntheses of Hydrido Monocarbonyl 1-H and Diiodo Methyl 5-Me

*2.3.1 Attempted synthesis of **1-H***

Further investigation was carried out by interception of the proposed intermediates in the hydride mechanism shown in Scheme 2.1. Attempts were made to synthesize the monocarbonyl complex **1-H** by sparging a solution of the dicarbonyl complex **4-H** with N_2 at -78 °C (see Scheme 2.4). However, there was no sign of formation of **1-H**. Instead, **4-H** slowly decomposes to the dimer **6**. Addition of the CO scavenger, $(CH_3)_3NO$ at -78 °C to **4-H** or bubbling a solution the hydrido dicarbonyl **4-H** with H_2 under high pressure of H_2 do not produce the desired complex. The dimer **6** is produced along with other unidentified non-hydride species. Because **4-H** is an $18e^-$ complex, we propose that dimerization is initiated by dissociation of CO from at least one rhodium complex. Once CO has dissociated, the reductive coupling with the other rhodium species occurs fast. That we cannot observe **1-H** directly is not unexpected since only very few examples of the four-coordinate complex $[RhH(CO)(PR_3)_2]$ have been isolated or characterized before, mostly with bulky monophosphine ligands in a *trans* configuration, indicating their highly unstable nature.[9,10]

Scheme 2.4. The attempted synthesis of hydrido monocarbonyl **1-H**

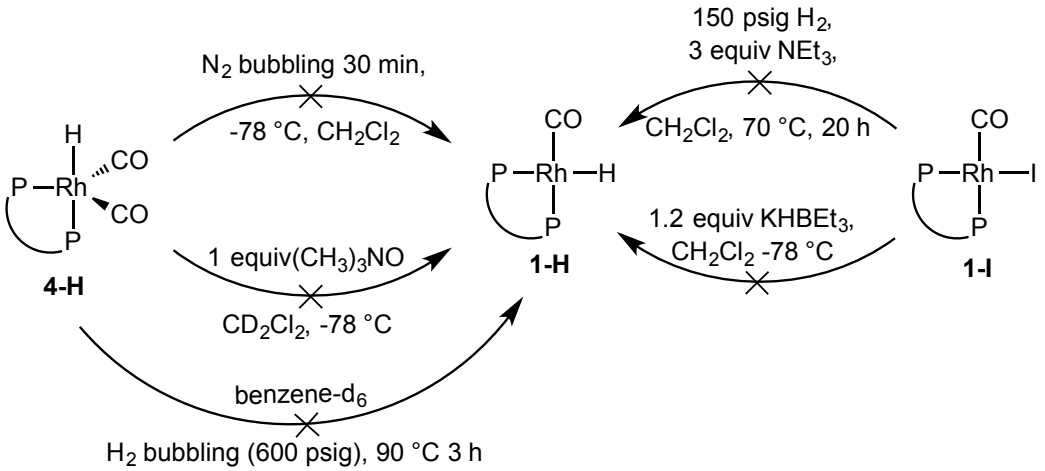

Attempts were also made to synthesize **1-H** via reaction of iodo monocarbonyl **1-I** with either the hydride donor reagent, $KHBEt_3$, at -78 °C, or 150 psig of H_2 at 70 °C in the presence of base. Unfortunately, the attempts to produce **1-H** via these methods were not successful. No hydride signal was observed in ^1H NMR spectrum under either set of conditions. The major product appeared as a new doublet at δ 19.3 ppm (d, $^1J_{P\text{-}Rh}$ = 181 Hz) that persists through warming to room temperature in ^{31}P NMR spectrum. We hypothesize that the four-coordinate monocarbonyl hydride **1-H**, formed in the absence of extra CO, dimerizes in a manner similar to **4-H** as shown in Scheme 2.2 resulting a dinuclear complex [{Rh(CO)(dppp)}$_2$] without terminal CO ligand. However, this product has not been characterized further.

*2.3.2 Attempted synthesis of hydrido methyl iodo monocarbonyl **5-Me***

In the reaction of hydrido dicarbonyl **4-H** and CH_3I some acetaldehyde was formed, We hypothesize that CH_3I reacted with the small amount of **1-H** present in equilibrium with **4-H.** Similarly, the dimerization of [RhH(CO)$_2$(dppp)] **4-H** is proposed to occur via dissociation of CO to form the monocarbonyl **1-H** (Scheme 2.2). Therefore, attempts were

made to react **4-H** with a large excess of CH_3I, which, if **1-H** were generated, would react to form **5-Me**. Such reaction would have been a strong evidence for the oxidative addition of CH_3I in the hydride mechanism. Unfortunately, the desired complex **5-Me** was not observed. The products were characterized by NMR spectroscopy as **6**, the diiodo Rh-methyl complex *cis*-$[RhI_2(CH_3)(CO)(dppp)]$ (**2-Me**), the dicarbonyl Rh-acetyl complex $[Rh(COCH_3)(CO)_2(dppp)]$ (**4-Ac**), and **3-Ac** (Scheme 2.5, see later section for independent syntheses and characterizations of these complexes).

Scheme 2.5. Attempted syntheses of $[RhHI(CH_3)(CO)(dppp)]$, **5-Me**.

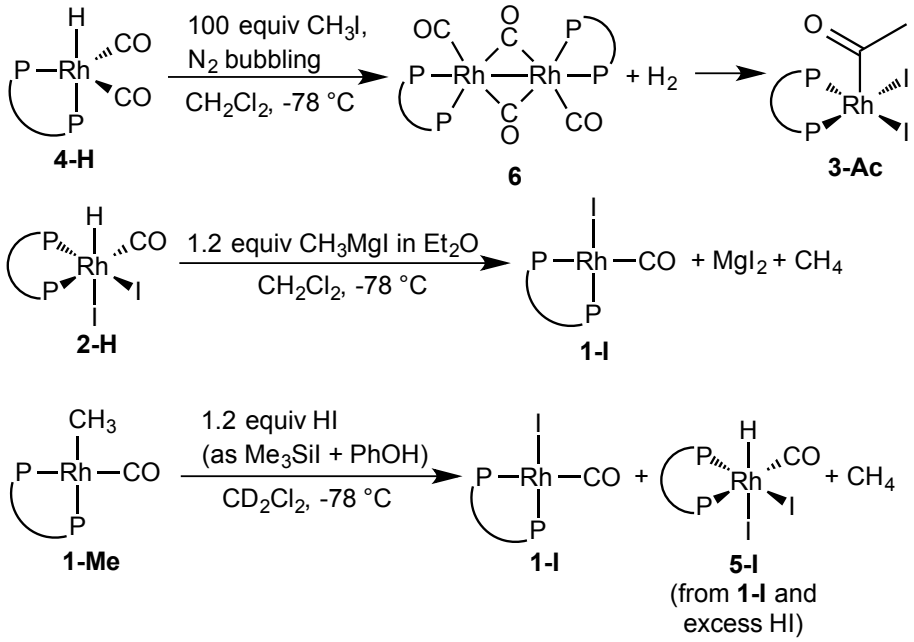

An alternative synthesis strategy toward **5-Me** was proposed as a reaction of HI with Rh-methyl complex, **1-Me** or **4-Me**. Reaction of **4-Me** with HI, generated *in situ* by mixing $(CH_3)_3SiI$ with PhOH, at -80 °C immediately produces dicarbonyl Rh-iodo complex **4-I** which reacts further with another equivalent of HI to produce diiodo Rh-hydrido complex **2-H**. There is no acetaldehyde or Rh-acetyl signal observed in ^1H NMR spectrum. One can

envisage that **4-Me** is a saturated complex, so it requires liberation of one CO before oxidative addition of HI can occur. The reaction is therefore possibly outcompeted by protonation of Rh-CH_3 by strong acid HI and generating **4-I** and CH_4.

To circumvent the aforementioned problem, we attempted to facilitate the oxidative addition of HI by using non-saturated monocarbonyl Rh-methyl complex **1-Me** to bypass the CO liberation step. In spite of possessing an open coordination site, addition of HI to the complex does not produce the hydrido methyl iodo monocarbonyl **5-Me**. Instead the products resulting from protonolysis of the methyl group, **1-I** and **4-I**, were observed again. An alternative explanation is that **5-Me** formed but immediately decomposed because of its reactive nature. In this case, the fact that we did not observe acetaldehyde implies that reductive elimination of CH_4 from **5-Me** is favored over CO migratory insertion to form Rh-acetyl **5-Ac**, which is inconsistent with the hydride mechanism. This preferential elimination of alkane was believed to be the case for $RhHCl(R)(CO)(PPh_3)_2$, a proposed intermediate in Rh-catalyzed aldehyde decarbonylation.[11,12] That we have not observed **5-Me** or acetaldehyde therefore does not clarify if the hydride mechanism is operational.

Table 2.1. NMR spectroscopy data for complexes characterized in this work[a]

Complex	Ligand	T (°C)	$^{31}P\{^{1}H\}$, δ (J, Hz)	Selected $^{13}C\{^{1}H\}$, δ (J, Hz)	Selected ^{1}H NMR, δ (J, Hz)
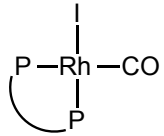 **1-I**	dppp	24	2.5 (dd, $J_{P\text{-}Rh,\ P\text{-}P}$ = 114, 55), 21.1 (dd, $J_{P\text{-}Rh,\ P\text{-}P}$ = 156, 55)	-	-
	dpppOEt	24	6.2 (dd, $^{1}J_{P\text{-}Rh}$ = 117, $^{2}J_{P\text{-}P}$ = 53), 21.7 (dd, $^{1}J_{P\text{-}Rh}$ = 162, $^{2}J_{P\text{-}P}$ = 53).		
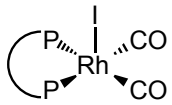 **4-I**	dppp	24	2.4 (d, $J_{P\text{-}Rh}$ = 106)	-	
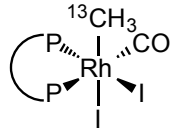 **^{13}C-2-Me(maj)**	dppp	-10	-13.3 (ddd, $^{1}J_{P\text{-}Rh}$ = 97, $^{2}J_{P\text{-}P}$ = 43, $^{3}J_{P\text{-}C}$ = 4), 10.2 (dd, (dd, $^{1}J_{P\text{-}Rh}$ = 112, $^{2}J_{P\text{-}P}$ = 43)	6.6 (ddd, $^{1}J_{C\text{-}Rh}$ = 18, $^{2}J_{C\text{-}P}$ = 4, 2)	1.45 (dtd, $^{1}J_{H\text{-}C}$ = 140, $J_{H\text{-}P,\ H\text{-}Rh}$ = 4, 2[b]; Rh-$^{13}C\mathit{H_3}$)
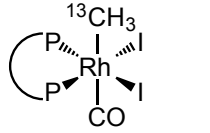 **^{13}C-2-Me(min)**	dppp	-10	17.0 (dd, $^{1}J_{P\text{-}Rh}$ = 120, 5)	6.5[c]	1.1 (dm, $^{1}J_{H\text{-}C}$ = 139[c]; Rh-$^{13}C\mathit{H_3}$)
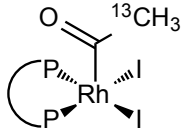 **^{13}C-3-Ac**	dppp	24	18.2 (d, $^{1}J_{P\text{-}Rh}$ = 132)	45.7 (s, Rh-CO^{13}CH$_3$)	3.01 (d, $^{1}J_{H\text{-}C}$ = 134, Rh-CO$^{13}C\mathit{H_3}$)

Complex	Ligand	T (°C)	$^{31}P\{^{1}H\}$, δ (J, Hz)	Selected $^{13}C\{^{1}H\}$, δ (J, Hz)	Selected ^{1}H NMR, δ (J, Hz)
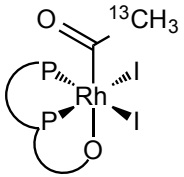 **^{13}C-3-Ac$_{OEt}$**	dpppOEt	-30	15.79 (dd, $^{1}J_{P\text{-}Rh}$ = 143, $^{2}J_{P\text{-}P}$ = 22) 26.48 (dd, $^{1}J_{P\text{-}Rh}$ = 133, $^{2}J_{P\text{-}P}$ = 21)	50.5 (s, Rh-CO^{13}CH$_3$)	3.45 (d, $^{1}J_{H\text{-}C}$ = 134, Rh-CO$^{13}C\mathit{H_3}$)
		24	16.9 (br s)	49.5 (s, Rh-CO^{13}CH$_3$)	3.42 (d, $^{1}J_{H\text{-}C}$ = 140, Rh-CO^{13}CH$_3$)
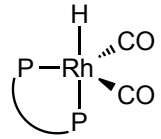 **4-H**	dppp	-80	17 (br s) and 7 (br s)	-	-9.14 (dd, $^{2}J_{H\text{-}Ptrans}$ = 110, $^{1}J_{H\text{-}Rh}$ = 12)
		-50	12.4 (d, $^{1}J_{P\text{-}Rh}$ = 112)[d]	-	-9.15 (td, $^{2}J_{H\text{-}P}$ = 55, $^{1}J_{H\text{-}Rh}$ = 12)
	dpppOEt	-80	-8.1 - (-3.3) (br m), 6.7 - 16.6 (br m)		-9.99 (br s), -8.91 (br s)
		24	10.8 (d, $^{1}J_{P\text{-}Rh}$ = 111)		-9.66 (td, $^{2}J_{H\text{-}P}$ = 55, $^{1}J_{H\text{-}Rh}$ = 12)
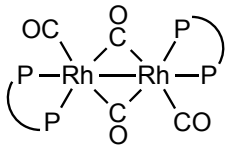 **6**	dppp	-80	3.3 (br d, $^{1}J_{P\text{-}Rh} \approx 190$), 14.6 (br s)	-	-
		24	8.1 (d, $^{1}J_{P\text{-}Rh}$ = 146)	-	-
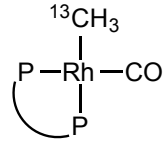 **^{13}C-1-Me$_{(OEt)}$**	dppp	-80	10.7 (ddd, $^{1}J_{P\text{-}Rh}$ = 104, $^{2}J_{P\text{-}C}$ = 56, $^{2}J_{P\text{-}P}$ = 48), 18.1 (ddd, $^{1}J_{P\text{-}Rh}$ = 131, $^{2}J_{P\text{-}P}$ = 48, $^{2}J_{P\text{-}C}$, = 10)	-5.7 (ddd, $^{2}J_{C\text{-}Ptrans}$ = 56, $^{1}J_{C\text{-}Rh}$ = 19, $^{2}J_{C\text{-}Pcis}$ = 10; Rh-^{13}CH$_3$)	-0.31 (dddd, $^{1}J_{H\text{-}C}$ = 124, $^{3}J_{H\text{-}Ptrans}$ = 8, $^{2}J_{H\text{-}Rh}$ = 5, $^{3}J_{H\text{-}Pcis}$ = 2; Rh-$^{13}C\mathit{H_3}$)[c]
	dpppOEt	-30	10.5 (m) 19.9 (ddd, $^{1}J_{P\text{-}Rh}$ = 134, $^{2}J_{P\text{-}P}$ = 47, $^{3}J_{P\text{-}C}$ = 10)	-6.1 (ddd, $^{2}J_{C\text{-}Ptrans}$ = 58, $^{1}J_{C\text{-}Rh}$ = 20, $^{2}J_{C\text{-}Pcis}$ = 10; Rh-^{13}CH$_3$)	-0.50 (br dt, $^{1}J_{H\text{-}C}$ = 126, $^{3}J_{H\text{-}Ptrans}$, $^{2}J_{H\text{-}Rh}$ = 7; Rh-$^{13}C\mathit{H_3}$)

Complex	Ligand	T (°C)	$^{31}P\{^{1}H\}$, δ (J, Hz)	Selected $^{13}C\{^{1}H\}$, δ (J, Hz)	Selected ^{1}H NMR, δ (J, Hz)
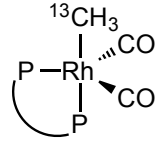 **^{13}C-4-Me$_{(OEt)}$**	dppp	-80	9.2 (dd, $^{1}J_{P\text{-}Rh}$ = 126, $^{2}J_{P\text{-}P}$ = 47) 17.8 (ddd, $^{1}J_{P\text{-}Rh}$ = 84, $^{2}J_{P\text{-}C}$ = 54, $^{2}J_{P\text{-}P}$ = 47)	-18.5 (ddd, $^{2}J_{C\text{-}Ptrans}$ = 54, $^{1}J_{C\text{-}Rh}$ = 15, $^{2}J_{C\text{-}Pcis}$ = 5)	-0.14 ppm (dddd, $^{1}J_{H\text{-}C}$ = 134, $^{3}J_{H\text{-}Ptrans}$ = 10, $^{2}J_{H\text{-}Rh}$ = 5, $^{3}J_{H\text{-}Pcis}$ = 1)
	dpppOEt	-80	12.7 (m, $^{1}J_{P\text{-}Rh}$ = 87, $^{2}J_{P\text{-}C}$ = 57, $^{2}J_{P\text{-}P}$ = 45) 19.8 (ddd, $^{1}J_{P\text{-}Rh}$ = 121, $^{2}J_{P\text{-}P}$ = 45)	-17.7 (br dd, $^{2}J_{C\text{-}Ptrans}$ = 57, $^{1}J_{C\text{-}Rh}$ = 11)	-0.53 (br d, $^{1}J_{H\text{-}C}$ = 133)
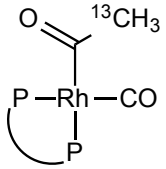 **^{13}C-1-Ac**	dppp	-30	1.0 (dd, $^{1}J_{P\text{-}Rh}$ = 159, $^{2}J_{P\text{-}P}$ = 56) 8.9 (ddd, $^{1}J_{P\text{-}Rh}$ = 83, $^{2}J_{P\text{-}P}$ = 56, $^{3}J_{P\text{-}C}$ = 21)	50.1 (ddd, $^{3}J_{C\text{-}Ptrans}$ = 21, $^{2}J_{C\text{-}Rh}$ = 11, $^{3}J_{C\text{-}Pcis}$ = 7)	2.10 (d, $J_{H\text{-}C}$ = 125, Rh-CO^{13}CH_3)
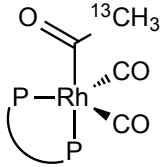 **^{13}C-4-Ac$_{(OEt)}$**	dppp	-30	1.5 (dd, $^{1}J_{P\text{-}Rh}$ = 136, $^{2}J_{P\text{-}P}$ = 53) 9.0 (ddd, $^{1}J_{P\text{-}Rh}$ = 65, $^{2}J_{P\text{-}P}$ = 53, $^{3}J_{PC}$ = 28)	52.9 (dt, $^{3}J_{C\text{-}Ptrans}$ = 28, $^{3}J_{C\text{-}Pcis}$ = 4, $^{2}J_{C\text{-}Rh}$ = 4)	2.04 (d, $^{1}J_{H\text{-}C}$ = 127, Rh-CO^{13}CH_3)
	dpppOEt	-80	2.9 (br s) 12.2 (dd, $^{1}J_{P\text{-}Rh}$ = 130, $^{2}J_{P\text{-}P}$ = 52)	51.1 (br d, $^{3}J_{C\text{-}Ptrans}$ = 28)	
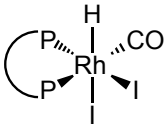 **2-H**	dppp	24	-1.2 (dd, $^{1}J_{P\text{-}Rh}$ = 95, $^{2}J_{P\text{-}P}$ = 43) 18.1 (dd, $^{1}J_{P\text{-}Rh}$ = 109.8, $^{2}J_{P\text{-}P}$ = 43)	-	-10.5 (t, J = 13[b])

[a] All the complexes are in solution of CD_2Cl_2 or CH_2Cl_2 unless noted otherwise.

[b] Coupling constants cannot be assigned specifically.

[c] From correlation experiments, multiplicity and coupling constants are not measureable.

[d] Coupling constant is measured from residual peak at room temperature

2.4 Synthesis, Characterization, and Reactivity of RhI(CO)(dppp) 1-I and $Rh(I)(CO)_2$(dppp) 4-I

*2.4.1 Synthesis and characterization of iodo carbonyls **1-I** and **4-I***

The complex **1-I** itself is also one of the important intermediates in both the hydride mechanism and the mechanism proposed by Wegman and Moloy. In their studies, Wegman and Moloy reported **1-I** as a complex with uncertain nuclearity, $[RhI(CO)(dppp)]_n$. Only elemental analysis data was available at that time due to its insolubility in most solvents.[13] The NMR spectroscopy data of the complex was published recently by Panthi et al.[14], no other data was reported therein. Hence, whether the complex is polymeric or not still has not been revealed. We were able to prepare **1-I** cleanly according to the published method with slight modification by salt metathesis from $[\{RhCl(CO)_2\}_2]$ and dppp with NaI in THF. Interestingly, we have not had problems dissolving the complex in CH_2Cl_2 or THF. We were also able to obtain crystallographic data revealing the monomeric square-planar structure of the complex.

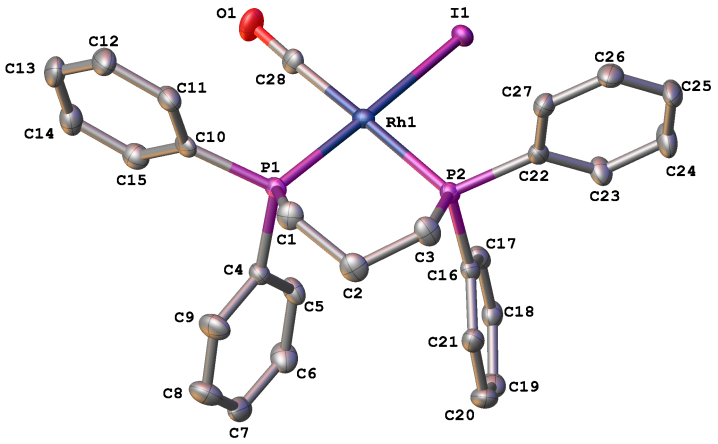

Figure 2.2. Crystallographic structure of **1-I**. Only one conformer of the co-crystallized complex is shown. All atoms are shown as 50% thermal probability ellipsoids. All H atoms are omitted for clarity.

The complex can be prepared from mixing the cationic rhodium precursor **[1-CO]BF_4** with NBu_4I followed by bubbling with N_2 to remove the extra CO ligand. From this synthesis route, it is questionable whether the iodide ion coordinates to $[Rh(dppp)(CO)_2]^+$ to form the five-coordinate complex **4-I** before CO is removed or CO needs to be removed before iodide coordinates. To answer this question is more complicated than what we expected because there is only very subtle change in ^{31}P NMR spectrum after the iodide ions have been added to **[1-CO]BF_4** , a decrease of $^1J_{P\text{-}Rh}$ about 6 Hz, while the chemical shift appears unchanged. The product after addition of iodide ions remains unchanged over a wide range of temperatures as judged by VTNMR experiments. This result indicates that the five-coordinate complex, if it forms, is not likely to be a trigonal bipyramidal complex, because such a complex is expected to undergo rapid Berry pseudo-rotation. Although a d^9 Rh^I species in a square-based pyramidal geometry is not common, we cannot rule out this possibility. The nature of the coordination geometry was unclear until the crystal structure of it was obtained, revealing this unexpected square pyramidal geometry of **4-I**.

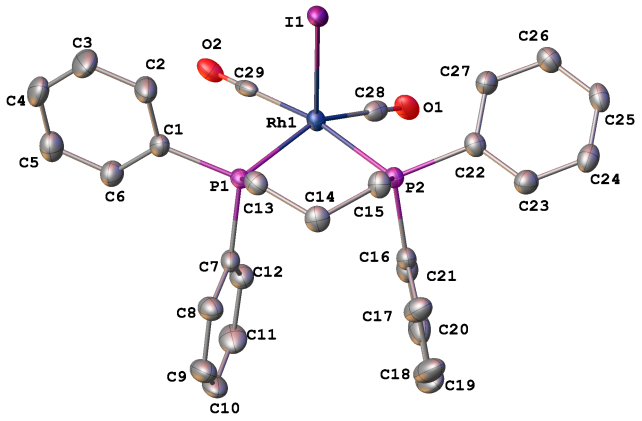

Figure 2.3. Crystallographic structure of **4-I**. All atoms are drawn as 50% thermal probability ellipsoids. All H atoms are omitted and disordered parts are omitted for clarity.

*2.4.2 Oxidative addition of CH_3I to iodo monocarbonyl **1-I** and characterization of diiodo methyl **2-Me***

When CH_3I was added to hydrido dicarbonyl **4-H** in CH_2Cl_2, the acyl diiodo complex **3-Ac** was observed as the primary rhodium-containing product. The only route known to produce this complex is the oxidative addition of CH_3I to the iodo monocarbonyl **1-I**. as proposed in the mechanism by Wegman and Moloy. In the original paper, this oxidative addition reaction was studied only for the Rh-dppe analogue of the dppp complex **1-I** (dppe = 1,2-bis(diphenylphosphino)ethane) because of the solubility issue mentioned above. For characterization purpose, we conducted this experiment at 0 °C where the reaction occurs slow enough to monitor. During the reaction, two isomeric diiodo carbonyl Rh-methyl intermediates, **2-Me(maj)** and **2-Me(min)**, were observed in accordance with the reported reaction of methyl iodide with the Rh-dppe complex. As described below, these complexes were assigned to have the structures shown here.

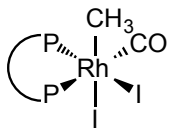

2-Me(maj)

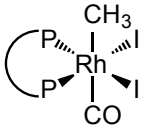

2-Me(min)

The major diiodo carbonyl methyl isomer, **2-Me(maj)**, appears as two doublets of doublets at δ -13.3 ppm and 10.2 ppm in the ^{31}P NMR spectrum indicating non-equivalent phosphorus atoms. A ^{31}P-^{1}H HSQC experiment shows crosspeaks between the ^{31}P NMR signals and a proton resonance at 1.45 ppm in the ^{1}H NMR spectrum. Correlation between the same proton resonance and a ^{13}C signal at 6.6 ppm in the ^{13}C NMR spectrum confirms that the resonances belong to a Rh-methyl complex. The small $^{2}J_{P\text{-}C}$ is consistent with the methyl group being *cis* to both phosporus atoms. The minor diiodo methyl isomer, **2-Me(min)**, was characterized by similar measurements. Only one doublet was observed in the ^{31}P NMR spectrum at 17.0 ppm, suggesting that the two phosporus atoms are equivalent indicating an octahedral coordination geometry with the phosphorus atoms and carbonyls in the same plane and a *trans* arrangement of the methyl and iodo groups. Although only **2-Me(maj)** has the *cis* arrangement of the methyl group and CO necessary for migratory insertion of CO to form **3-Ac**, neither isomer of **2-Me** was observed at the end of the reaction. This observation requires that formation of **2-Me(min)** is reversible or that there is a mechanism for isomerization of **2-Me(min)** to **2-Me(maj).** The final product **3-Ac** is a thermodynamic sink. The kinetic studies according to this model are described in detail in section 3.4 of chapter 3 (see Scheme 3.2).

2.5 Synthesis and Characterization of Rh-methyl and Rh-acetyl complexes 1-Me, 4-Me, 1-Ac, and 4-Ac

Although the syntheses of key intermediates in the proposed mechanism were not

successful, it is worth reviewing the characterization of **1-Me** and **4-Me** precursor complexes and their CO insertion products, Rh-acetyl complexes **1-Ac** and **4-Ac** (Scheme 2.6). The rhodium complexes of this type are involved in many proposed catalytic mechanisms, including hydroformylation and alkylation, but the number of complexes directly observed and characterized is surprisingly small. To date, the reported four-coordinate complexes with the formula [Rh(R)(CO)P_2] mostly have two monophosphine ligands coordinated in a *trans* configuration like the reported four-coordinate Rh-hydrido complexes.[15–18] Only two exceptions are known—from the work of Urtel *et al*. where [Rh(neopentyl)(CO)(dtbpm)] (dtbpm = bis(di-*tert*-butylphosphino)methane) was observed in the reaction of [Rh(neopentyl)(dtbpm)] with CO; and the work of Nelsen and Landis where [Rh(1-phenylethyl)(CO)(BDP)] (BDP = bis(diazaphospholane)) was observed by monitoring reaction of [RhH$(CO)_2$(BDP)] with styrene at low temperature.[19,20]. The latter report also contains the only published observation of a [Rh(R)$(CO)_2$(P^P)] complex. The complex [Rh(acyl)$(CO)_2P_2$] is similarly rare.[15,20–23] To the best of our knowledge, the four-coordinate [Rh(acyl)(CO)P_2] has not been reported before.

Scheme 2.6. Synthesis routes for mono- and dicarbonyl Rh-methyl and Rh-acetyl complexes.

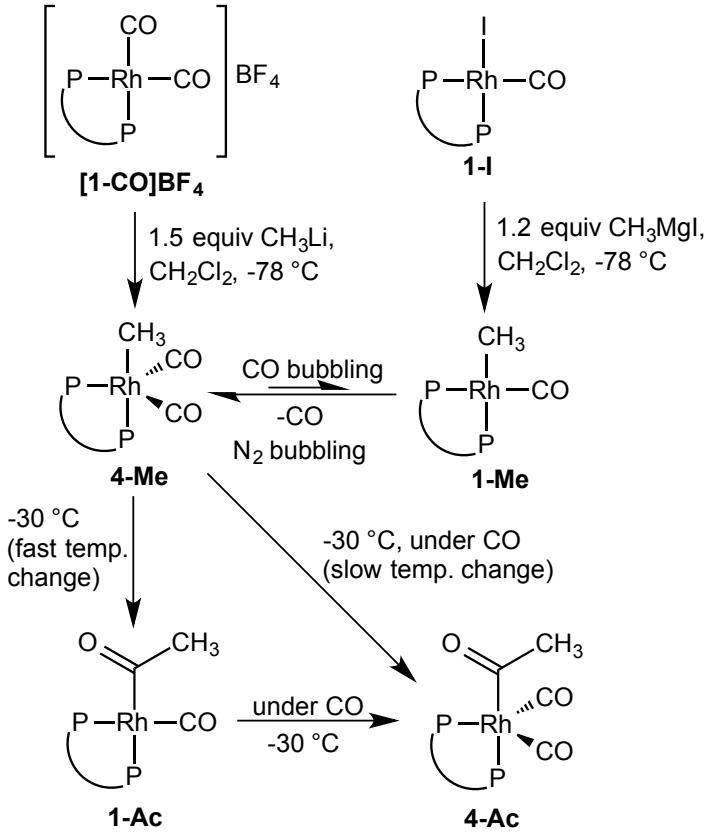

*2.5.1 Synthesis and characterization of methyl dicarbonyl **4-Me***

The five-coordinate Rh-methyl complex **4-Me** was prepared via alkylation of the cationic complex **[1-CO]BF$_4$** with CH_3Li under a CO atmosphere at -78 °C. ^{13}C-enriched $^{13}CH_3Li$ was used, in conjunction with a three-channel NMR instrument, to characterize the complex by selective ^{31}P-decoupling in the $^{13}C\{^{31}P\}$ spectrum and ^{13}C-^{31}P correlation experiments. As a result, we found that one of the ^{31}P signal possesses ABMX pattern with a large coupling constant to ^{13}C ($^2J_{P\text{-}C}$ = 54 Hz) and relatively small coupling constant to Rh ($^1J_{P\text{-}Rh}$ = 84 Hz), agreeing with coupling between the *trans* phosphorus atom and the methyl group, which is a strong sigma donor ligand. The phosphorus *cis* to the methyl group shows no apparent coupling to carbon. The chemical shifts of the methyl group in both ^{13}C and ^{1}H

NMR spectra are in upfield regions (at -18.5 and -0.14 ppm, respectively, for the dppp complex). These chemical shifts are consistent with reported values for $Rh(CH_3)(CO)P_2$ complexes (which range from δ (-5) – (-3) ppm and δ (-0.7) – (-0.3) ppm by ^{13}C and ^{1}H NMR spectroscopy, respectively), with slightly more upfield on ^{13}C.[15,16] It is important to note that we compare our signals with four-coordinate complexes, for which the reference data are available, and the NMR data did not provide enough data to determine coordination number. The complex is prone to CO insertion at higher temperature, precluding us from doing variable temperature experiments. Although the precursor and synthesis conditions suggested likely formation of a five-coordinate complex, the coordination number could not be conclusively determined until the four-coordinate methyl monocarbonyl complex **1-Me** was characterized.

*2.5.2 Synthesis and characterization of **1-Me***

Upon access to the monocarbonyl Rh-iodo complex **1-I**, synthesis of the four-coordinate complex **1-Me** was relatively simple. The complex **1-Me** was generated cleanly by alkylation of **1-I** with CH_3MgI at -78 °C. Characterization of the complex **^{13}C-1-Me** by ^{1}H, ^{13}C, and ^{31}P NMR spectroscopy gave results similar to **^{13}C-4-Me**, consistent with the product containing a Rh-methyl group. When the solution of methyl monocarbonyl **1-Me** was bubbled with CO, we observed the signals of methyl dicarbonyl **4-Me,** which can be reverted to the original complex by bubbling with N_2, giving strong evidence on the coordination number of each complex (see Scheme 2.6). Addition of one CO to the coordination sphere (as with **4-Me**) results in about 20 Hz decrease in $^{1}J_{P\text{-}Rh}$ of the ^{31}P NMR signal for the phosphine *trans* to the methyl group, consistent with bonding changes expected on expansion of the coordination sphere. It is interesting that although the chemical shift of

both ^{31}P signals look similar in four- and five-coordinate complexes, the shifts associated with *cis* and *trans* arrangements of phosphorus atoms with respect to the methyl switch positions. With assignments based on the values of $^{2}J_{P\text{-}C}$ of the phosphorus signals, the phosphorus atom *trans* to the methyl group shifts downfield by 7.1 ppm from **^{13}C-1-Me** to **^{13}C-4-Me** while the *cis* phosphine shifts upfield by 8.9 ppm. The former occurs due to the deshielding effect from the presence *trans* CO in the coordination sphere, while in the latter, CO ligands are not directly *trans* to phosphorus.

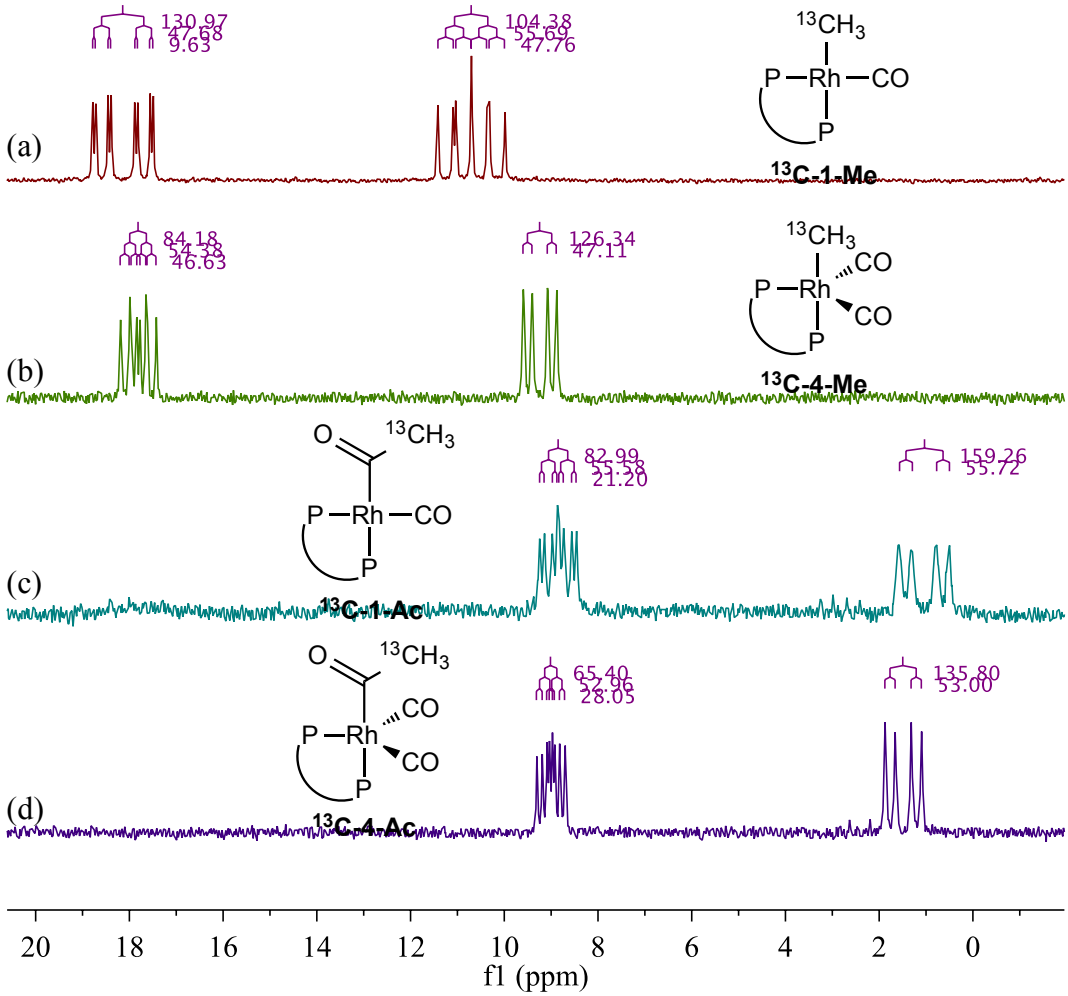

Figure 2.4. $^{31}P\{^{1}H\}$ NMR spectra of (a) **^{13}C-1-Me** (145.8 MHz, -80 °C, CH_2Cl_2), (b) **^{13}C-4-Me** (242.8 MHz, -75 °C, CD_2Cl_2), (c) **^{13}C-1-Ac** (202.5 MHz, -30 °C, CD_2Cl_2), and (d) **^{13}C-4-Ac** (242.8 MHz, -30 °C, CD_2Cl_2) all showing ^{13}C-^{31}P coupling.

*2.5.3 Observation and characterization of acyl monocarbonyl **1-Ac** and acyl dicarbonyl **4-Ac***

Upon warming methyl dicarbonyl **4-Me**, the Rh-acetyl complexes **1-Ac** and **4-Ac** were observed. The four-coordinate, monocarbonyl **1-Ac** was observed only when the sample solution was not fully saturated with CO and the temperature was increased rapidly from -80 °C to -30 °C. When the sample of monocarbonyl **4-Me** was saturated with an

atmospheric pressure of CO at -80 ºC, and then warmed up slowly, complete conversion to **4-Ac** was observed at temperatures as low as -60 °C (see Scheme 2.6). This indicates rapid coordination of CO to the four-coordinate complex and thermodynamic preference for a five coordinate complex under these conditions.

The downfield ^{31}P signals in ^{13}C-enriched acyl **^{13}C-1-Ac** and **^{13}C-4-Ac** complexes show ABMX patterns similar to those observed for the Rh-methyl complexes **1-Me** and **4-Me**. All ^{13}C-X coupling constants for **1-Ac** and **4-Ac** were lower than those observed in the corresponding Rh-methyl complexes, consistent with weaker coupling to the more remote methyl group of the acetyl ligand. A similar degree of reduction in $^{1}J_{\text{P-Rh}}$ of the ^{31}P signal for the phosphine *trans* to the acetyl group was observed upon CO coordination, similar to the Rh-methyl complexes. Both ^{13}C and ^{1}H signals of the methyl group shift downfield to the acetyl region, providing strong evidence for acetyl group formation.

2.6 Characterization and Reactivity of Rh-dpppOEt Analogues

Recently, our collaborators from Dow Chemical performed ligand screening to optimize catalysis of the MRC reaction. Many dppp derivatives were found to out-perform dppp, with improved selectivity and activity. To help gain an understanding of the mechanism and reveal the origin of this superiority, we chose to study the best performing ligand from the screening, 1,3-bis(di-2-ethoxyphenylphosphino)propane (dpppOEt) for comparison.

Rh-dpppOEt analogues of many of the Rh-dppp complexes described above were synthesized by similar methods. We can confirm, with the aid of heteronuclear NMR spectroscopy and correlation experiments, that the Rh-dpppOEt analouges have formed successfully with spectroscopic data shown in Table 2.1. However, most of the samples

contained multiple signals with poorly defined features, making it difficult to clarify the exact composition of each reaction mixture, whether they contained multiple conformers, isomers or totally different compounds.

2.6.1 Reactivity of Rh-hydrido dpppOEt complex ***4-H$_{OEt}$***

In spite of the characterization difficulties in the other complexes, we managed to carry out basic experiments on the dicarbonyl Rh-hydrido complex analogue of dppp, **4-H$_{OEt}$** which was produced cleanly according to ^{31}P NMR spectroscopy. Unlike the hydrido complex of dppp, this complex is very stable. Even after it was subjected to heat at 50 °C or to reduced pressure at room temperature, there was little conversion to unidentified species. The stability of **4-H$_{OEt}$** results in no immediate reactivity with CH_3I unless the sample is bubbled with N_2, producing acetaldehyde and methane along with multiple signals in the ^{31}P NMR spectrum. This stability likely is impacted by both electronic and steric effects of the aryl ethers. The electron donating ethoxy groups promote stronger back-bonding from Rh to CO, making CO dissociation from the saturated complex more difficult, while its increased steric bulk, in comparison to dppp, hinders oxidative addition of CH_3I or the dimerization with other Rh center. These results do not clarify whether the hydride mechanism is operating, although they do suggest that the dpppOEt ligated complexes should be less reactive if the hydride mechanism were operative.

2.6.2 NMR Characterization of [RhI$_2$(COCH$_3$)(dpppOEt)], ***3-Ac$_{OEt}$***

It is worthwhile to mention the diiodo Rh-acetyl complex **3-Ac$_{OEt}$**, in particular, because its characterization data is substantially different from that of the dppp analogue. The acyl diiodo complex **3-Ac** is the center of attention in the mechanism proposed by Wegman and Moloy and its structure is undoubtedly characterized by crystallography as a five-

coordinate square-based pyramidal complex with the acyl group at the apex. The geometry is common for five-coordinate d^6 Rh^{III} complexes, and the ^{31}P NMR spectrum shows a doublet in accordance with the equivalent phosphorus atoms.

On the other hand, we have found that the complex **3-Ac$_{OEt}$** has a broad singlet signal at 17.0 ppm in ^{31}P NMR spectrum at room temperature. Upon cooling it down to -30 °C, the signal decoalesces to two doublets of doublets with a AMX pattern, common for Rh(diphosphine) complexes with non-equivalent phosphorus atoms (see characterization data in Table 2.1). Although possible, it is unlikely for a Rh^{III} complex to possess trigonal bipyramidal geometry. The only difference between dppp and dpppOEt is the ortho-ethoxy group on the phenyl ring, so we suggest that the complex has one ethoxy group coordinated to the Rh center, differentiating two phosphorus atoms. The coordination of the ethoxy groups exchanges between two ends of the ligand faster than NMR time frame at room temperature and causes coalescence of the ^{31}P NMR signals. This coordination is also proposed to be immensely important, as it is believed to promote ionization of the complex in methanol and facilitate the hydrogenolysis according to the alternative ionization mechanism (see section 3.6 and 3.7 in chapter 3)

2.7 The Dimer Mechanism and Disproval of the Hydride Mechanism

With characterization data for many of the proposed intermediates, we were able to analyze Rh-complex speciation observed in the reaction of the hydride dicarbonyl **4-H** with CH_3I by NMR spectroscopy. The reaction mixture starts with **4-H** in excess CH_3I at -30 °C under synthesis gas where the complex is stable. Slowly warming up the sample converts the complex to the dimer **6** followed by the formation of the iodo monocarbonyl **1-I**, the iodo dicarbonyl **4-I** and the acetyl dicarbonyl **4-Ac**. The presence of complex **4-Ac** without iodide

coordination is not expected according to the hydride mechanism. This suggests either that the oxidative addition to **1-H** does not occur or that the oxidative addition product **5-Me** favors reductive elimination of CH_4 and HI rather than acetaldehyde. These outcomes are not consistent with the observed data and **1-H** is eliminated as a likely intermediate in MRC. The species observed later in the reaction is the methyl diiodo carbonyl**2-Me,** which subsequently underwent CO insertion to give the acetyl diidodo **3-Ac**. We propose a non-catalytic pathway, shown in Scheme 2.7, for this reaction. The pathway starts with reductive coupling of two hydrido dicarbonyls (**4-H),** that is followed by release of H_2, and the dinuclear complex **6**, consistent with experimental observation. Instead of reacting with **1-H**, CH_3I oxidatively cleaves the dimer **6** to yield iodo dicarbonyl **4-I** and methyl dicarbonyl **4-Me**. The latter complex is converted to the acetyl dicarbonyl **4-Ac** in the presence of CO followed by reaction with H_2 to eliminate acetaldehyde and regenerate the hydride **4-H**. Eventually, all the complexes converge to iodo dicarbonyl **4-I**, which is in equilibrium with the iodo monocarbonyl **1-I**. The oxidative addition of CH_3I with **1-I** forms acetyl diiodo **3-Ac**, the thermodynamic sink at room temperature or below and under an atmospheric pressure of synthesis gas. To support the hypothesis, we intentionally allowed **4-H** to completely dimerize to **6** (but without removing H_2 from solution) before addition of CH_3I, and the same distribution of Rh complexes was observed. Interestingly, when the reaction started from **6** in the absence of H_2, the complex reacts with another equivalent of CH_3I and acetone was found as the major organic product.

Scheme 2.7. Proposed dimer mechanism[†].

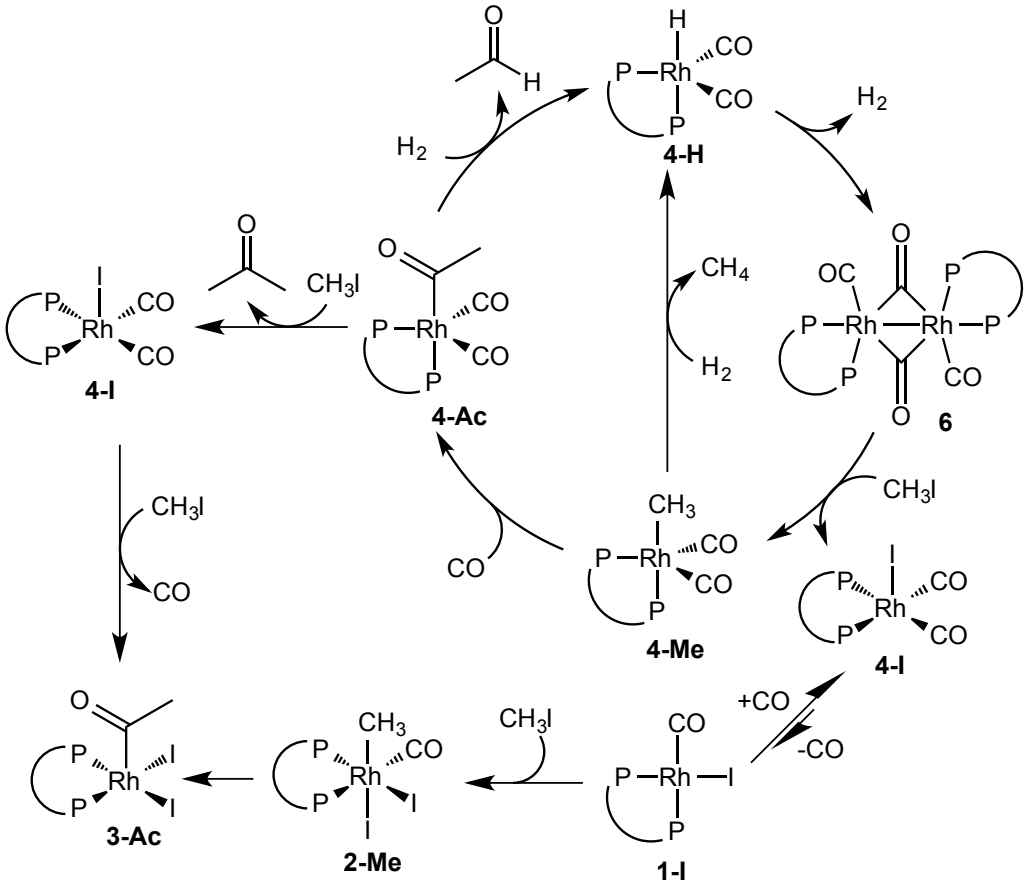

The proposed pathway through dimer formation explains the results from the reaction of hydrido carbonyl **4-H** with CH_3I at low temperature and pressure, but it is not necessary true that the reaction according to the hydride mechanism does not occur under the catalytic conditions. Other experiments were performed to confirm that the mechanism via Rh-hydrido complex is not operating. Apart from formation of different intermediate species, the other key differences between the hydride mechanism and the Wegman-Moloy mechanism are a)

[†] Although the mechanism is drawn in cycle, there is Rh complex lost from the cycle, and therefore it is a stoichiometric, not catalytic, reaction converging to $RhI_2(COCH_3)(dppp)$ in the pathway at the bottom.

that a Rh-hydrido complex needs to form from **1-I** under catalytic conditions and b) that acetaldehyde does not form from the complex **3-Ac**. We used a high pressure NMR equipment, namely Wisconsin High Pressure NMR Reactor – WiHP-NMRR (more details on the instrument in chapter 3) to monitor the reaction of **1-I** under 900 psig of 2:1 H_2/CO at 120 °C for 4 h. No formation of **1-H** or **4-H** or even its dimer **6** was observed; only traces of acetaldehyde were observed. These results indicate that catalytic MRC did not occur under these conditions and that hydrido dicarbonyl **1-H** was not regenerated at the conclusion of reaction. These observations argue against any catalytic cycle with **1-H** as an on-cycle intermediate.

To reveal the origin of the acetaldehyde, specifically, whether it comes from the acetyl group of the acetyl diiodo complex **3-Ac** or not, ^{13}C-labeled **^{13}C-3-Ac** was treated with 2:1 synthesis gas at 120 °C in MeOH. The reaction produced dimethyl acetal acetaldehyde, $^{13}CH_3CH(OCH_3)_2$, as a major product, suggesting that acetaldehyde formation shares the a common intermediate along the pathway to formation of both acetic acid and acetaldehyde in accordance with the mechanism proposed by Wegman and Moloy. Interestingly, the experiments with ^{13}C-enriched complex demonstrated that the catalysis requires MeOH as a solvent. The reaction loses selectivity (from 87% to 5% selectivity) when done in THF or CH_2Cl_2. These results, together with the inhibitive effect of iodide ions on catalysis, may indicate that the operating mechanism involves dissociation of iodide ion. The results of experiments with ^{13}C-labeled **^{13}C-3-Ac** indicate that the hydride mechanism is not operating.

2.8 Conclusions

We have reinvestigated a potential mechanism for MRC that features a critical role for hydrido monocarbonyl as an on-cycle intermediate. In the process of these investigations

a large number of related rhodium complexes were synthesized and characterized. Studies of the reactivity and speciation of these complexes lead us to propose a stoichiometric tranformation of hydrido dicarbonyl **4-H** and CH_3I through dinuclear complex **6** at lower temperature and low synthesis gas pressure. Experiments at higher pressure and temperature are not consistent with the hydride mechanism but support the original Wegman-Moloy mechanism. However, new observations are suggestive of possible ionic intermediates generated by the dissociation of I from diiodo rhodium complexes. As a result we suggest the further exploration of a reaction mechanism involving ionization of the catalytic species to uncover the missing details of the catalysis. Such studies require observation of reaction at high pressure and temperature where the catalysis occurs. Such studies are facilitated by the new instrument, WiHP-NMRR, as described in the next chapter.

2.9 Experimental

General Considerations

All manipulations were carried out under N_2 using standard Schlenk, high vacuum, and glovebox techniques. Dichloromethane, diethyl ether, $^{13}CH_3I$, dppp were obtained from Sigma-Aldrich. CD_2Cl_2 was obtained from Cambridge Isotope Laboratories. All solvents and liquid reagents were degassed by at least three freeze-pump-thaw cycles or sparging with N_2 and dried by passing through activated alumna unless otherwise noted. $^{13}CH_3I$ was used as received. $RhCl_3 \cdot xH_2O$ from Alfa Aesar and $Rh(acac)(CO)_2$ from Dow were used as received. Most of the Rh complexes were synthesized *in situ* in an NMR tube for characterization purposes and were not isolated. The isotopically unlabeled complexes were prepared similarly to the corresponding labeled complexes and the complexes of dpppOEt ligand were prepared in a manner similar to the analogous complexes of dppp ligand. The complex $[RhCl(CO)_2]_2$ was prepared according to the reported procedure.[24,25]

Routine NMR experiments were performed on Bruker AC+ 300a and Avance-400 spectrometers. All reaction monitoring, variable temperature, and two-dimensional correlation experiments were performed on Varian Unity 500 and Inova 600, and Bruker Avance-360 and Avance-500 spectrometers. ^1H NMR spectra were referenced with a solvent peak. ^{31}P and ^{13}C NMR spectra were referenced with ^1H NMR spectrum by absolute referencing. All the coupling constants are reported in hertz (Hz). NMR yield was calculated from integration of signals of interest divided by total integration of a ^{31}P NMR spectrum.

RhI(CO)(dppp) (1): The synthesis was modified from reported method.[13] $[RhCl(CO)_2]_2$ (0.140 g, 0.360 mmol), dppp (0.296 g, 0.718 mmol, 1.99 equiv), and NaI (1.08 g, 7.21 mmol, 20.0 equiv,) were stirred together in 7 mL THF at room temperature for 18 h. The solvent was then removed under vacuum resulting pale yellow solid. Dichloromethane

10 mL was added and the yellow solution was filtered from the solid three times to remove the product from NaCl and excess NaI. The filtrate was combined and dried under vacuum. Yield 93.7%. ^{1}H NMR (500.2 MHz, CH_2Cl_2, 24 °C): δ 1.98 (2H, br m, PCH_2CH_2), 2.33 (2H, br m, PCH_2), 2.55 (2H, br m, PCH_2), 7.3-7.6 (20H, m, aromatic dppp). ^{31}P{^{1}H} NMR (202.4 MHz, CH_2Cl_2, 24 °C): δ 3.4 (dd, $^{1}J_{P\text{-}Rh}$ = 114, $^{2}J_{P\text{-}P}$ = 55), 22.0 (dd, $^{1}J_{P\text{-}Rh}$ = 156, $^{2}J_{P\text{-}P}$ = 55).

RhI(CO)(dpppOEt) ($\mathbf{1_{OEt}}$): Yield 97.1%. ^{1}H NMR (500.2 MHz, THF, 24 °C): δ 0.87 (6H, t, *J* = 7, OCH_2CH_3), 1.19 (6H, br s , OCH_2CH_3), 1.95 (2H, br m, PCH_2CH_2), 2.59 (2H, br m, PCH_2), 2.66 (2H, br m, PCH_2), 3.77 (m, OCH_2CH_3), 3.89 (m, OCH_2CH_3) 4.02 (m, OCH_2CH_3) 4.09 (m, OCH_2CH_3), 6.82 (2H, m, aromatic dpppOEt), 6.91 (6H, m, aromatic dpppOEt), 7.37 (4H, m, aromatic dpppOEt), 7.92 (4H, br s, aromatic dpppOEt). ^{31}P{^{1}H} NMR (202.4 MHz, THF, 24 °C): δ 6.3 (dd, $^{1}J_{P\text{-}Rh}$ = 117, $^{2}J_{P\text{-}P}$ = 53), 22.0 (dd, $^{1}J_{P\text{-}Rh}$ = 161, $^{2}J_{P\text{-}P}$ = 53).

[Rh(CO)$_2$(dppp)]BF$_4$ (12BF$_4$): Solution of dppp (0.0148 g, 0.0360 mmol) was added to a mixture of $[RhCl(CO)_2]_2$ (0.0070 g, 0.0180 mmol) and $AgBF_4$ (0.0084 g, 0.0433 mmol) in CD_2Cl_2. The mixture was agitated by suction and release with Pasteur pipette multiple times until no more white solid formed. The solution was filtered by syringe filter to remove the solid into an NMR tube. The solution in the NMR tube with septum cap was bubbled with CO through long fine needle until the solution turned from brownish red to bright yellow, usually within a few minutes.

[Rh(CO)$_2$(dpppOEt)]BF$_4$ ($\mathbf{12_{OEt}BF_4}$): Yield: 100 % (NMR). ^{1}H NMR (500.2 MHz, CD_2Cl_2, 24 °C): δ 1.32 (12H, t, *J* = 7, OCH2CH_3), 2.24 (2H, br m, PCH_2CH_2), 2.74 (4H, dt, *J* = 11, 6; PCH_2), 4.12 (8H, q, *J* = 7, OCH_2CH_3), 6.78 (4H, m, aromatic dpppOEt) 6.98 (8H, m, aromatic dpppOEt), 7.45 (4H, m, aromatic dpppOEt). ^{31}P{^{1}H} NMR (202.4 MHz, CD_2Cl_2,

24 °C): δ -8.3 (d, $^{1}J_{P\text{-}Rh}$ = 114). $^{31}P\{^{1}H\}$ NMR (202.4 MHz, CD_2Cl_2, - 80 °C): δ -26.2 (br), -23.9 (br), -18.8 (d, $^{1}J_{P\text{-}Rh}$ = 117), -2.2 (br),10.0 (br).

$RhH(CO)_2(dppp)$ (5CO): Solution of $[Rh(CO)_2(dppp)]BF_4$ under atmospheric pressure of synthesis gas in NMR tube in dry ice/isopropanol bath was injected with solution of $KHBEt_3$ (1.00 M in THF, 0.043 mL, 0.043 mmol). Carefully not to let the solution warm up, the NMR tube was inverted a few times, to facilitate mixing, resulting dark green solution. Yield: 100 % (NMR). ^{1}H NMR (500.2 MHz, CD_2Cl_2, -80 °C): δ -9.14 (1H, dd with broad s in the middle, $^{2}J_{H\text{-}Ptrans}$ = 110 Hz, $^{1}J_{H\text{-}Rh}$ = 12 Hz, Rh-*H*), 2.33 (4H, br s, PCH_2), 6.7-7.5 (20H, m, aromatic dppp). ^{1}H NMR (500.2 MHz, CD_2Cl_2, -50 °C): δ -9.14 (1H, dd with broad s in the middle, $^{2}J_{H\text{-}Ptrans}$ = 110 Hz, $^{1}J_{H\text{-}Rh}$ = 12 Hz, Rh-*H*), 2.33 (4H, br s, PCH_2), 6.7-7.5 (20H, m, aromatic dppp). $^{31}P\{^{1}H\}$ NMR (202.4 MHz, CD_2Cl_2, -80 °C): δ 7.4 (br s), 17.3 (br s). ^{1}H NMR (500.2 MHz, CD_2Cl_2, -50 °C): δ -9.15 (td, $^{2}J_{H\text{-}P}$ = 55, $^{1}J_{H\text{-}Rh}$ = 12).

$RhH(CO)_2(dpppOEt)$ (5_{OEt}CO): Yield: 100 % (NMR). ^{1}H NMR (500.2 MHz, CD_2Cl_2, 24 °C): δ -9.66 (1H, td, $^{2}J_{H\text{-}Ptrans}$ = 55, $^{1}J_{H\text{-}Rh}$ = 11, Rh-*H*), 0.94 (12H, t, OCH2CH_3), 1.9 (2H, br m, PCH_2CH_2), 2.66 (4H, br m, PCH_2), 3.6-3.8 (8H, m, OC*H2*CH_3), 6.74 (4H, d, *J* = 8, aromatic dpppOEt) 6.86 (4H, t, *J* = 8, aromatic dpppOEt), 7.27 (4H, t, *J* = 8, aromatic dpppOEt) 7.64 (4H, q, *J* = 7, aromatic dpppOEt). $^{31}P\{^{1}H\}$ NMR (202.4 MHz, CD_2Cl_2, -80 °C): δ -9.9 (br, Rh-H), -8.9 (br). $^{31}P\{^{1}H\}$ NMR (202.4 MHz, CD_2Cl_2, 24 °C): δ 10.8 (d, $^{1}J_{P\text{-}Rh}$).

$[Rh(CO)_2(dppp)]_2$ (8): The sample was prepared similar to aforementioned $RhH(CO)_2(dppp)$, but the addition of $KHBEt_3$ solution was done at room temperature. Warming the solution of $RhH(CO)_2(dppp)$ to room temperature also produced this dimer. An alternative method followed reported synthesis in order to confirm the identity of the

complex.[7] Yield: 100 % (NMR). ^{1}H NMR (500.2 MHz, CD_2Cl_2, 24 °C): δ 2.44 (4H, br s, PC*H*$_2$), 7.14 - 7.57 (20H, m, aromatic dppp). ^{31}P{^{1}H} NMR (202.4 MHz, CD_2Cl_2, 24 °C): δ 8.1 (d, $^{1}J_{P\text{-}Rh}$ = 146 Hz).

Attempted synthesis of RhH(CO)(dppp) (5): *Method A*. Solution of $RhH(CO)_2$(dppp) in CH_2Cl_2 was bubbled with N_2 at -78 °C for 30 min, then at -50 °C for 10 min. *Method B*. Solution of RhI(CO)(dppp) (0.0180 mmol) prepared from bubbling [$Rh(CO)_2$(dppp)]BF_4 in the presence of NBu_4I was added with $KHBEt_3$ solution (1.00 M in THF, 0.043 mL, 0.043 mmol) at -78 °C. *Method C*. Solution of RhI(CO)(dppp) (0.0241 g, 0.0360 mmol) in CH_2Cl_2 with Et_3N (0.010 mL, 0.072 mmol) was stirred under 150 psig of H_2 at 70 °C for 20 h. *Method D*. Solution of $RhH(CO)_2$(dppp) (0.0360 mmol) in CD_2Cl_2 was added with solution of $(CH_3)_3NO$ (0.125 mL of 288 mM $(CH_3)_3NO$ in CD_2Cl_2, 0.0360 mmol, 1.00 equiv) at -78 °C. *Method E*. Solution of Rh(acac)(dppp) (0.0114 g, 0.0185 mmol) in benzene-d_6 was pressurized to 400 psig 1:1 H_2/CO and heated to 60 °C for 10 min in WiHP-NMRR (see the reaction setup in chapter 3). Then the reactor was cooldowned to room temperature, vented, re-pressurized to 600 psig H_2 and heated to 90 °C. The reaction was followed by NMR spectroscopy for 3 h.

Rh(^{13}CH$_3$)(CO)(dppp) (^{13}C-9): A solution of RhI(CO)(dppp) (0.0150 g, 0.0224 mmol) in dichloromethane at -78 °C in dry ice/isopropanol bath was prepared in an NMR tube with septum cap. The sample was added with $^{13}CH_3MgI$ solution (1.0 M in Et_2O, 0.027 mL, 0.027 mmol) by syringe. The NMR tube was inverted quickly a few times for mixing. Yield: 96.7 % (NMR). ^{1}H NMR (360.1 MHz, CH_2Cl_2, -80 °C): δ -0.31 (3H, dddd, $^{1}J_{H\text{-}C}$ = 124, $^{3}J_{H\text{-}Ptrans,}$ = 8, $^{2}J_{H\text{-}Rh}$ = 5, $^{3}J_{H\text{-}Pcis}$ = 2; Rh-^{13}C*H*$_3$*;* *J* values gathered from multiple experiments), 2.38 (2H, br m, PC*H*$_2$), 2.45 (2H, br s, PC*H*$_2$) 6.8-7.1 (20H, m, dppp aromatic).

$^{13}C\{^{1}H\}$ NMR (90.6 MHz, CH_2Cl_2, -80 °C) δ -5.7 (ddd, $^{2}J_{C\text{-}Ptrans}$ = 56, $^{1}J_{C\text{-}Rh}$ = 19,, $^{2}J_{C\text{-}Pcis}$ = 10; Rh-$^{13}CH_3$) 124.7, 125.0, 125.2, 127.5, 127.8, 128.1, 128.4, 128.7, 128.9, 137.2 (all s, dppp aromatic). $^{31}P\{^{1}H\}$ NMR (145.8 MHz, CH_2Cl_2, -80 °C): δ 10.7 (ddd, $^{1}J_{P\text{-}Rh}$ = 104, $^{2}J_{P\text{-}C}$ = 56, $^{2}J_{P\text{-}P}$ = 48), 18.1 (ddd, $^{1}J_{P\text{-}Rh}$ = 131, $^{2}J_{P\text{-}P}$ = 48, $^{2}J_{P\text{-}C}$, = 10)

Rh($^{13}CH_3$)(CO)(dpppOEt) (^{13}C-9$_{OEt}$): Yield: 56.1 % (NMR). ^{1}H NMR (360.1 MHz, CH_2Cl_2, -30 °C): δ -0.50 (br dt, $^{1}J_{H\text{-}C}$ = 126, $J_{H\text{-}Ptrans,\ H\text{-}Rh}$ = 7; Rh-$^{13}CH_3$. $^{13}C\{^{1}H\}$ NMR (90.6 MHz, CH_2Cl_2, -80 °C) δ -6.1 (ddd, $^{2}J_{C\text{-}Ptrans}$ = 58, $^{1}J_{C\text{-}Rh}$ = 20,, $^{2}J_{C\text{-}Pcis}$ = 10; Rh-$^{13}CH_3$). $^{31}P\{^{1}H\}$ NMR (145.8 MHz, CH_2Cl_2, -80 °C): δ 10.5 (m), 19.9 (ddd, $^{1}J_{P\text{-}Rh}$ = 134, $^{2}J_{P\text{-}P}$ = 47, $^{3}J_{P\text{-}C}$ = 10).

Rh($^{13}CH_3$)(CO)$_2$(dppp) (^{13}C-9CO): Solution of $[Rh(CO)_2(dppp)]BF_4$ (0.0152 mmol) prepared by aforementioned method in septum-capped NMR tube at -78 °C in dry ice/isopropanol bath was added with $^{13}CH_3Li$ (0.26 M in Et_2O, 0.25 mL, 0.065 mmol) by syringe. The NMR tube was inverted quickly a few times for mixing. Yield: 100 % (NMR). ^{1}H NMR (599.7 MHz, CH_2Cl_2, -75 °C): δ -0.14 ppm (dddd, $^{1}J_{H\text{-}C}$ = 134, $^{3}J_{H\text{-}P\textit{trans}}$ = 10, $^{2}J_{H\text{-}Rh}$ = 5, $^{3}J_{H\text{-}Pcis}$ = 1.4, Rh-$^{13}CH_3$; *J* values gathered from multiple experiments), 1.58 (2H, br m, PCH_2CH_2), 2.31 (2H, br m, PCH2), 2.38 (2H, br m, PCH_2), 7.1-7.4 (20H, m, dppp aromatic). $^{13}C\{^{1}H\}$ NMR (150.8 MHz, CH_2Cl_2, -75 °C) δ -18.5 (ddd, $^{2}J_{C\text{-}Ptrans}$ = 54, $^{1}J_{C\text{-}Rh}$ = 15,, $^{2}J_{C\text{-}Pcis}$ = 5; Rh-$^{13}CH_3$), 128.1 (d, *J* = 10), 128.4 (d, *J* = 8), 129.4 (s), 129.8 (s), 132.3 (m) (aromatic dppp). $^{31}P\{^{1}H\}$ NMR (242.8 MHz, CH_2Cl_2, -75 °C): δ 9.2 (dd, $^{1}J_{P\text{-}Rh}$ = 126, $^{2}J_{P\text{-}P}$ = 47), 17.8 (ddd, $^{1}J_{P\text{-}Rh}$ = 84, $^{2}J_{P\text{-}C}$ = 54, $^{2}J_{P\text{-}P}$ = 47).

Rh($^{13}CH_3$)(CO)$_2$(dpppOEt) (^{13}C-9$_{OEt}$CO): Yield: 83.1 % (NMR). ^{1}H NMR (500.2 MHz, CD_2Cl_2, -80 °C): δ -0.53 (br d, $^{1}J_{H\text{-}C}$ = 133). $^{13}C\{^{1}H\}$ NMR (125.8 MHz, CD_2Cl_2, -80 °C) δ -17.7 (dd, *J* = 57, 11, Rh-$^{13}CH_3$). $^{31}P\{^{1}H\}$ NMR (202.5 MHz, CD_2Cl_2, -80 °C): δ 12.7

(m, $^{1}J_{P\text{-}Rh}$ = 87, $^{2}J_{P\text{-}C}$ = 57, $^{2}J_{P\text{-}P}$ = 45), 19.8 (ddd, $^{1}J_{P\text{-}Rh}$ = 121, $^{2}J_{P\text{-}P}$ = 45).

Rh(CO^{13}CH$_3$)(CO)(dppp) (^{13}C-10): Solution of Rh(^{13}CH$_3$)(CO)$_2$(dppp) was warmed immediately to -30 °C. Yield: 80% (NMR). ^{1}H NMR (500.2 MHz, CD_2Cl_2, -30 °C): δ 2.10 (3H, d, $^{1}J_{H\text{-}C}$ = 125, Rh-CO^{13}C*H$_3$*), 2.64 (2H, br m, PC*H$_2$*), 2.80 (2H, br s, PC*H$_2$*) 6.7-8.0 (20H, m, dppp aromatic). ^{13}C{^{1}H} NMR (125.8 MHz, CD_2Cl_2, -30 °C) δ 50.1 (ddd, $^{3}J_{C\text{-}P\textit{trans}}$ = 21, $^{2}J_{C\text{-}Rh}$ = 11, $^{3}J_{C\text{-}P\textit{cis}}$ = 7, Rh-CO*^{13}C*H$_3$), 127 - 134 (br m, dppp aromatic). ^{31}P{^{1}H} NMR (202.4 MHz, CD_2Cl_2, -30 °C): δ 1.0 (dd, $^{1}J_{P\text{-}Rh}$ = 159, $^{2}J_{P\text{-}P}$ = 56), 8.9 (ddd, $^{1}J_{P\text{-}Rh}$ = 83, $^{2}J_{P\text{-}P}$ = 56, $^{3}J_{P\text{-}C}$ = 21)

Rh(CO^{13}CH$_3$)(CO)$_2$(dppp) (^{13}C-10CO): Solution of Rh(^{13}CH$_3$)(CO)$_2$(dppp) was slowly warmed up to -30 °C and bubbled with CO if needed. Yield: 100% (NMR). ^{1}H NMR (599.7 MHz, CH_2Cl_2, -30 °C): δ 1.70 (2H, br m, PCH$_2$C*H$_2$*), 2.04 (d, $^{1}J_{H\text{-}C}$ = 127, Rh-CO^{13}C*H$_3$*), 2.35 (2H, br m, PCH2), 2.42 (2H, br m, PC*H$_2$*), 7.1-7.6 (20H, m, dppp aromatic). ^{13}C{^{1}H} NMR (150.8 MHz, CH_2Cl_2, -30 °C) δ 52.9 (dt, $^{3}J_{C\text{-}P\textit{trans}}$ = 28, $^{3}J_{C\text{-}P\textit{cis}}$ = 4, $^{2}J_{C\text{-}Rh}$ = 4), 128.3 (d, *J* = 10), 128.7 (d, *J* = 8), 129.8 (s), 130.1 (s), 132.3 (t, *J* = 12) (aromatic dppp). ^{31}P{^{1}H} NMR (242.8 MHz, CH_2Cl_2, -30 °C): δ 1.5 (dd, $^{1}J_{P\text{-}Rh}$ = 136, $^{2}J_{P\text{-}P}$ = 53), 9.0 (ddd, $^{1}J_{P\text{-}Rh}$ = 65, $^{2}J_{P\text{-}P}$ = 53, $^{3}J_{PC}$ = 28).

Rh(CO^{13}CH$_3$)(CO)$_2$(dpppOEt) (^{13}C-10$_{OEt}$CO): Yield: 62 % (NMR). ^{1}H NMR (500.2 MHz, CD_2Cl_2, -80 °C): δ -0.53 (br d, $^{1}J_{H\text{-}C}$ = 133), 6.3 - 8.6 (16H, m, dpppOEt aromatic). ^{13}C{^{1}H} NMR (125.8 MHz, CD_2Cl_2, -80 °C) δ 51.1 (br d, $^{3}J_{C\text{-}P\textit{trans}}$ = 28). ^{31}P{^{1}H} NMR (202.5 MHz, CD_2Cl_2, -80 °C): δ 12.7 (m, $^{1}J_{P\text{-}Rh}$ = 87, $^{2}J_{P\text{-}C}$ = 57, $^{2}J_{P\text{-}P}$ = 45), 19.8 (ddd, $^{1}J_{P\text{-}Rh}$ = 121, $^{2}J_{P\text{-}P}$ = 45).

RhI$_2$(CO^{13}CH$_3$)(dpppOEt) (^{13}C-3OEt): Solution of RhI(CO)(dpppOEt) (0.0189 g, 0.0247 mmol) and $^{13}CH_3I$ (0.0045 mL, 0.045 mmol), both in CD_2Cl_2, were mixed at 25 °C

overnight. Excess $^{13}CH_3I$ was removed under vacuum. Yield: 96% (NMR) ^1H NMR (500.2 MHz, CD_2Cl_2, -30 °C): δ 0.6-1.4 (12H, m, OCH_2CH_3), 2.08 (2H, br m, PCH_2CH_2), 2.50 (4H, br m, PCH_2), 3.7-4.1 (8H, m, OCH_2CH_3), 6.5 – 8.3 (16H, m, aromatic dpppOEt). $^{13}C\{^1H\}$ NMR (125.8 MHz, CD_2Cl_2, -50 °C) δ 50.5 (s, Rh-$CO^{13}CH_3$). $^{31}P\{^1H\}$ NMR (202.5 MHz, CD_2Cl_2, -30 °C): δ 15.79 (dd, $^1J_{P\text{-}Rh}$ = 143, $^2J_{P\text{-}P}$ = 22), 26.48 (dd, $^1J_{P\text{-}Rh}$ = 133, $^2J_{P\text{-}P}$ = 21). $^{31}P\{^1H\}$ NMR (202.5 MHz, CD_2Cl_2, 24 °C): δ 16.9 (br s).

Reaction of RhI(CO)(dppp) with $^{13}CH_3I$, synthesis of $RhI_2(CO^{13}CH_3)$(dppp): The complex RhI(CO)(dppp) (0.0241 g, 0.0360 mmol) in CH_2Cl_2 in a septum-capped NMR tube was cooled to -78 °C in dry ice/isopropanol bath. Solution of $^{13}CH_3I$ (0.045 mL, 0.072 mmol) was injected with syringe. The reaction was monitored at -30 °C, -10 °C and 24 °C, respectively. Yield 100% (NMR). ^1H NMR (500.22 MHz, CH_2Cl_2, 24 °C): δ 1.58 (2H, br m, PCH_2CH_2), 2.43 (2H, br m, PCH_2), 3.09 (2H, br m, PCH_2), 3.01 (d, $^1J_{H\text{-}C}$ = 134, Rh-$CO^{13}CH_3$), 7.1-7.7 (20H, m, dppp aromatic).

$RhHI_2$(CO)(dppp) (11): $RhI_2(COCH_3)$(dppp) (0.036 mmol) in THF was stirred at 120 °C under 120 psig H_2 for 5 h. The product was crystalized after many monthes in freezer at -30 °C. The complex also observed when mix RhI(CO)(dppp) with HI generated in situ from mixing PhOH and $(CH_3)_3Si$, but it was not as clean. Yield 93.6% (NMR).

Attempted synthesis of $RhHI(CH_3)$(CO)(dppp) (6): *Method A.* Solution of $RhH(CO)_2$(dppp) (0.0360 mmol, prepared in situ) in CH_2Cl_2 in NMR tube at -78 °C was added with CH_3I (3.60 mmol, 0.224 mL) and bubbled with N_2 for 30 min. *Method B.* Solution of $RhHI_2$(CO)(dppp) (0.0248 mmol) in THF was added with solution of CH_3MgI (0.030 mmol) in Et_2O at -78 °C. *Method C*. Solution of $Rh(CH_3)$(CO)(dppp) (0.0298 mmol) in CD_2Cl_2 was added with a mixture of Me_3SiI (0.035 mmol, 0.005 mL) and PhOH (0.035

mmol, 0.0033 g) at -78 °C.

Reaction of $RhH(CO)_2(dppp)$ with CH_3I: Solution of $RhH(CO)_2(dppp)$ (0.0246 mmol) in CD_2Cl_2 at -30 °C in an NMR tube was added with CH_3I (0.015 mL, 0.246 mmol,10 equiv) and slowly warmed up to room temperature while it was observing by NMR spectroscopy. Alternative reaction setup was carried out for comparison by adding 1 equiv of CH_3I each time, or adding CH_3I at room temperature where the starting complex had been converted to the dimer.

Reaction of $RhI_2(CO^{13}CH_3)(dppp)$ with synthesis gas: Solution of $RhI_2(CO^{13}CH_3)(dppp)$ (0.0360 mL) in MeOH in pressure bottle reactor was prepared in the glovebox. The reactor was pressurized with H_2 to 50 psig and vented 3 times to remove N_2 and pressurized with 160 psig 2:1 H_2/CO before it was lowered into oil bath at 120 °C and stirred for 5 h. The sample was transferred to NMR tube and analyzed under H_2 atmosphere without removing CO.

2.10 References

(1) Castellanos-Páez, A.; Castillón, S.; Claver, C.; van Leeuwen, P. W. N. M.; de Lange, W. G. J. *Organometallics* **1998**, *17*, 2543–2552.

(2) Brown, J. M.; Kent, A. G. *J. Chem. Soc. Perkin Trans. 2,* **1987**, 1597.

(3) Bregman, F. R.; Ernsting, J. M.; Muller, F.; Boele, M. D. K.; van der Veen, L. A.; Elsevier, C. J. *J. Organomet. Chem.* **1999**, *592*, 306–311.

(4) Evans, D.; Yagupsky, G.; Wilkinson, G. *J. Chem. Soc. A* **1968**, 2660.

(5) Brown, C. K.; Wilkinson, G. *J. Chem. Soc. A* **1970**, 2753–2764.

(6) Del Río, I.; de Lange, W. G. J.; van Leeuwen, P. W. N. M.; Claver, C. *J. Chem. Soc. Dalt. Trans.* **2001**, *2*, 1293–1300.

(7) James, B. R.; Mahajan, D.; Rettig, S. J.; Williams, G. M. *Organometallics* **1983**, *2*, 1452–1458.

(8) Fung, D. C. M.; James, B. R. *Gazz. Chim. Ital.* **1992**, *122*, 329–334.

(9) Freeman, M. A.; Young, D. A. *Inorg. Chem.* **1986**, *25*, 1556–1560.

(10) Yoshida, T.; Okano, T.; Ueda, Y.; Otsuka, S. *J. Am. Chem. Soc.* **1981**, *103*, 3411–3422.

(11) Ohno, K.; Tsuji, J. *J. Am. Chem. Soc.* **1968**, *90*, 99–107.

(12) Doughty, D. H.; Anderson, M. P.; Casalnuovo, A. L.; McGuiggan, M. F.; Tso, C. C.; Wang, H. H.; Pignolet, L. H. In *Catalytic Aspects of Metal Phosphine Complexes*; Alyea, E. C.; Meek, D. W. Eds.; Advances in Chemistry Vol. 196; American Chemical Society: Washington, DC, 1982; pp. 65–83.

(13) Moloy, K. G.; Wegman, R. W. *Organometallics* **1989**, *8*, 2883–2892.

(14) Panthi, B. D.; Gipson, S. L.; Franken, A. *Organometallics* **2010**, *29*, 5890–5896.

(15) Macdougall, J.; Simpson, M.; Cole-Hamilton, D. J. *Polyhedron* **1993**, *12*, 2877–2881.

(16) Boyd, S. E.; Field, L. D.; Hambley, T. W.; Partridge, M. G. *Organometallics* **1993**, *12*, 1720–1724.

(17) Krug, C.; Hartwig, J. F. *J. Am. Chem. Soc.* **2002**, *124*, 1674–1679.

(18) Hegedus, L. S.; Kendall, P. M.; Lo, S. M.; Sheats, J. R. *J. Am. Chem. Soc.* **1975**, *97*, 5448–5452.

(19) Urtel, H.; Meier, C.; Eisenträger, F.; Rominger, F.; Joschek, J. P.; Hofmann, P. *Angew. Chemie Int. Ed.* **2001**, *40*, 781–784.

(20) Nelsen, E. R.; Landis, C. R. *J. Am. Chem. Soc.* **2013**, *135*, 9636–9639.

(21) Cheliatsidou, P.; White, D. F. S.; Cole-Hamilton, D. J. *Dalton Trans.* **2004**, 3425–

3427.

(22) Yagupsky, G.; Brown, C. K.; Wilkinson, G. *J. Chem. Soc. A Inorganic, Phys. Theor.* **1970**, 1392.

(23) Thaler, E. G.; Folting, K.; Caulton, K. G. *J. Am. Chem. Soc.* **1990**, *112*, 2664–2672.

(24) Hanh Nguyen, D.; Lassauque, N.; Vendier, L.; Mallet-Ladeira, S.; Le Berre, C.; Serp, P.; Kalck, P. *Eur. J. Inorg. Chem.* **2014**, *2014*, 326–336.

(25) Montag, M.; Schwartsburd, L.; Cohen, R.; Leitus, G.; Ben-David, Y.; Martin, J. M. L.; Milstein, D. *Angew. Chemie Int. Ed.* **2007**, *46*, 1901–1904.

Chapter 3

Kinetic Studies of Rh(diphosphine)-Catalyzed Methanol Reductive Carbonylation – Demonstration of *In Situ* High Pressure NMR Spectroscopy and Support for an Ionization Mechanism

3.1 Introduction

In the previous chapter, we investigated the mechanism of rhodium-catalyzed methanol reductive carbonylation (MRC), a process for converting methanol to acetaldehyde under a syngas atmosphere. Two mechanisms were considered, one originally proposed by Wegman and Moloy and one, the hydride mechanism, based on the intermediacy of the same rhodium hydrido carbonyl intermediate that plays a key role in hydroformylation.[1,2] Our investigations utilized the capability of NMR spectroscopy to observe a variety of intermediate complexes and their reactivity at low or ambient temperature and atmospheric pressure of syngas. Many complexes implicated by both reaction mechanisms were characterized and their reactivity patterns led us to conclude that the reaction is unlikely to occur through the hydride complex. In addition, a number of observations suggest that at the critical hydrogenolysis step, the active catalyst species is an ionized, cationic rhodium acyl complex. The rate dependencies on H_2 and CO partial pressure are markedly different between dppp- and dpppOEt-based catalysts as shown in equation (3.1) and (3.2).* The different rate laws for the two closely related ligands are consistent with faster hydrogenolysis of acetyl complexes for the dpppOEt ligated catalysts. However, the direct spectroscopy study of the hydrogenolysis reaction requires monitoring the process under high pressure of syngas at elevated temperature; otherwise the reaction does not occur. Such conditions are not commonly accessible in an NMR spectrometer or other instruments capable of monitoring reaction progress. This limitation hampered our understanding of the

* The rate laws were estimated by Dow from the analysis of the product mixtures from the reactions run under different conditions.[13]

product-forming step in the reductive carbonylation of methanol.

$$\text{Rate law of Rh-dppp catalyzed MRC:} \qquad Rate = k[Rh] \tag{3.1}$$

$$\text{Rate law of Rh-dpppOEt catalyzed MRC:} \qquad Rate = \frac{k[Rh][CH_3I][H_2]^x}{[CO]^y} \tag{3.2}$$

In order to study gas-liquid reactions under high pressures and temperature by NMR spectroscopy, our group has developed a new apparatus that we call the **Wi**sconsin **H**igh **P**ressure **NMR R**eactor (WiHP-NMRR). In its current form, the instrument is able to collect data at elevated pressure (up to 750 psig) and temperature (150 °C; the temperature is limited by the base NMR probe). It is equipped with a high-pressure liquid injection port allowing the user to inject a solution of substrate or catalyst into the reaction at working conditions without having to lower the pressure or temperature of the reactor. A gas circulation system bubbles headspace gas into the liquid phase so as to maintain a constant concentration of dissolved gases. These features are very useful for monitoring the reaction with fast kinetics without loss of initial rate information and with precise knowledge of gas concentrations. Moreover, the system has an attached washing system. After each experiment, wash solvents are run through the system and then removed under vacuum. This is done without the need to remove the apparatus from the NMR instrument, greatly reducing the inactive time of the instrument.[3–7]

In this chapter, we demonstrate that the WiHP-NMRR can be successfully used to monitor MRC *in situ*. The ability to follow the decay of the starting material and formation of the products at high gas pressure allowed us to obtain kinetic information that was not previously achievable. Unexpectedly, we also observed an ionized intermediate when the Rh-dpppOEt catalyst was used in place of the Rh-dppp catalyst, which supports an ionization mechanism for MRC.

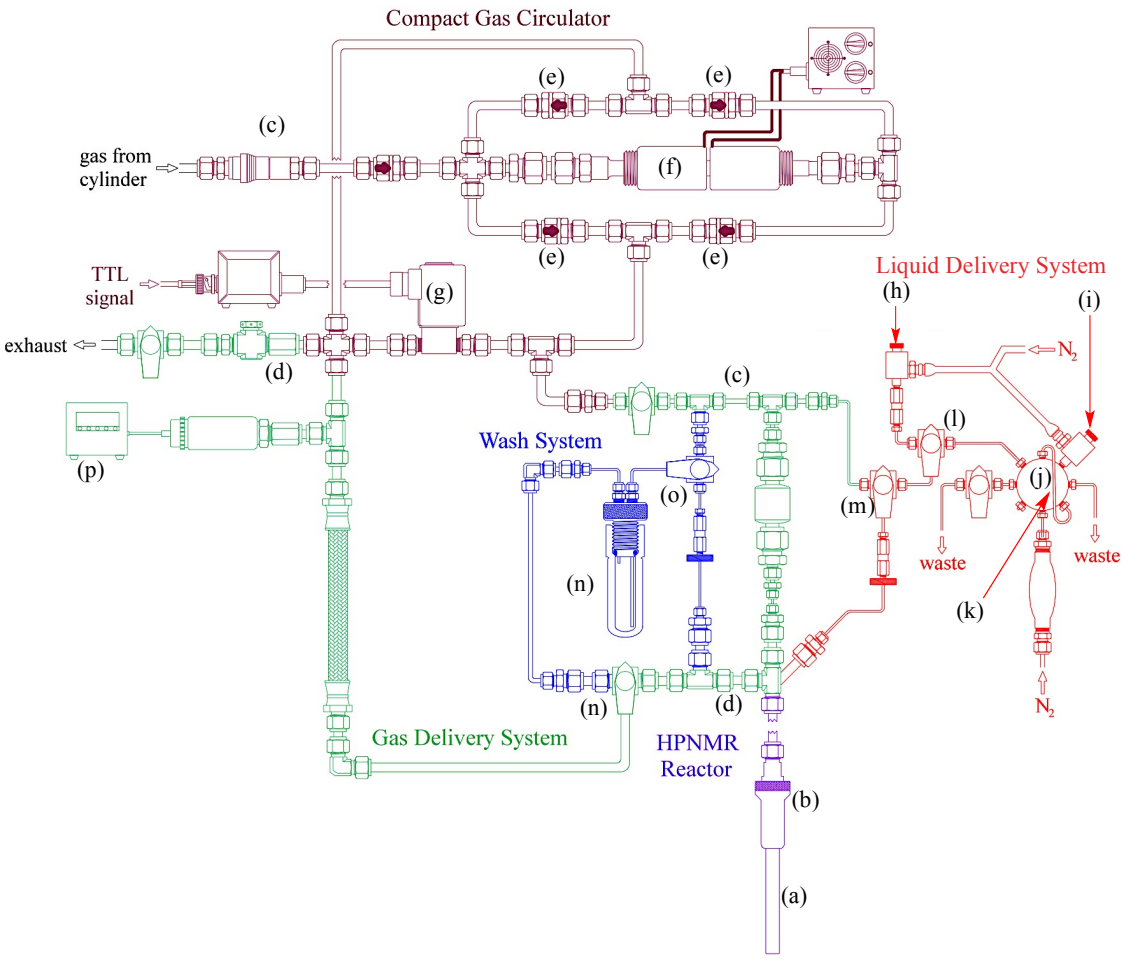

(a) sapphire NMR tube
(b) titanium holder
(c) feed route
(d) recycle route
(e) check valves
(f) solenoid coils
(g) solenoid valves (for circulation control)
(h) manual injection port
(i) HPLC injection port
(j) HPLC valve
(k) sample loop
(l) injection selection valve
(m) injection/gas feed valve
(n) wash bottle
(o) wash valves
(p) pressure transducer

Figure 3.1. Diagram of WiHP-NMRR.

3.2 WiHP-NMRR Apparatus and Setup

The WiHP-NMRR apparatus was created by Dr. Nicholas Beach and is currently under development by Dr. Spring Knapp. The apparatus was designed to be a removable

component that inserts into a standard NMR spectrometer in the place of an NMR tube. The current design fits the 10 mm probe of Bruker Avance-360 spectrometer. At the stage where the research described in this thesis was conducted, the apparatus comprised the following functional parts.

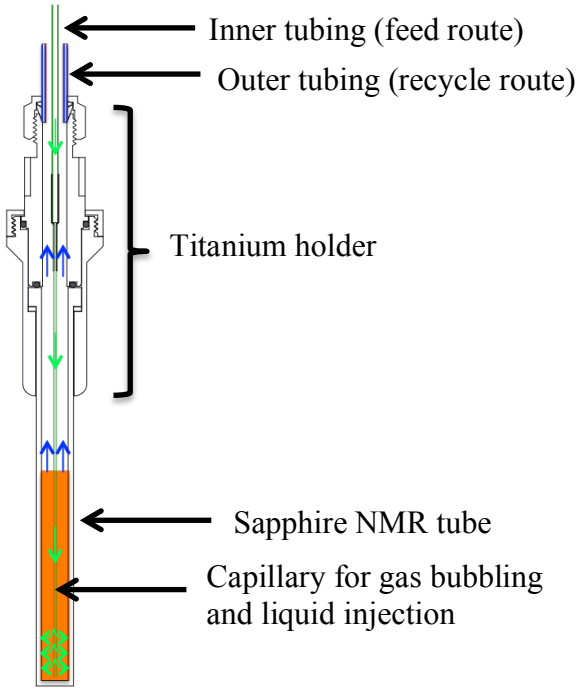

Figure 3.2. Sapphire NMR tube reactor and titanium holder. The inside shows the gas flow path with gas proceeding through the central capillary, bubbling through the solution, and exiting through the interannular space (arrows indicating flow direction).

a) Thick-walled sapphire NMR tube with titanium holder (Figure 3.2). The sapphire NMR tube functions like standard NMR tubes, but its thick wall allows working pressure up to 3000 psi. The top of the tube attaches to a holder made of titanium for physical strength, chemical resistance and non-magnetic property. The holder connects to stainless steel tubing that serves as gas/liquid delivery route.

b) Gas delivery system. The system connects to two gas inlets, one for N_2 and the

other one for working (reaction) gas. The working gas inlet also connects to a regulator and gas reservoir bottle, which receives and stores working gas from the gas cylinder. This setup continuously supplies working gas through the regulator and keeps the system pressure constant throughout the experiment without having the cylinders of toxic or flammable gas like syngas opened. The gas delivery system connects to the NMR tube reactor by two routes. The "feed" route runs through the circulator and connects to small stainless steel tube inside the outer tub that attaches to the titanium holder. The inner tube terminates with a glass capillary, which extends to the bottom of the NMR tube reactor, serving as a gas bubbling capillary (Figure 3.2). This same capillary is also used to deliver liquid in the high-pressure liquid injection system and to remove liquid when cleaning using the wash system (see below). The other route, called the "recycle" route, connects to the outer tube and receives gas from the reactor, which is then fed back to the circulator.

c) Circulator. The circulator is a small pump made of a magnetic stainless steel piston placed inside a honed stainless steel tube that is surrounded by two solenoid coils. This piston separates two chambers, each of which has two check valves to control the direction of gas flow in a one-way fashion. When electricity is applied through the control unit, the solenoid coils alternately pull the piston to move back and forth in the tube, constantly pressurizing one chamber and depressurizing the opposite. The pressure chamber vents gas through the check valve, while the partial vacuum of the other chamber draws gas in. An example of this mechanism is shown by blue arrows in Figure 3.3. When the piston moves toward the left chamber, the chamber is pressurized and vents out, while the right chamber is depressurized and draws more gas into it. The red arrows show the other half of the cycle. The alternate push and pull movement of the piston causes nearly continuous flow of gas.

The gas flow rate is controlled by the distance between two solenoid coils, which determines how far the piston moves, and the frequency of the piston motion.

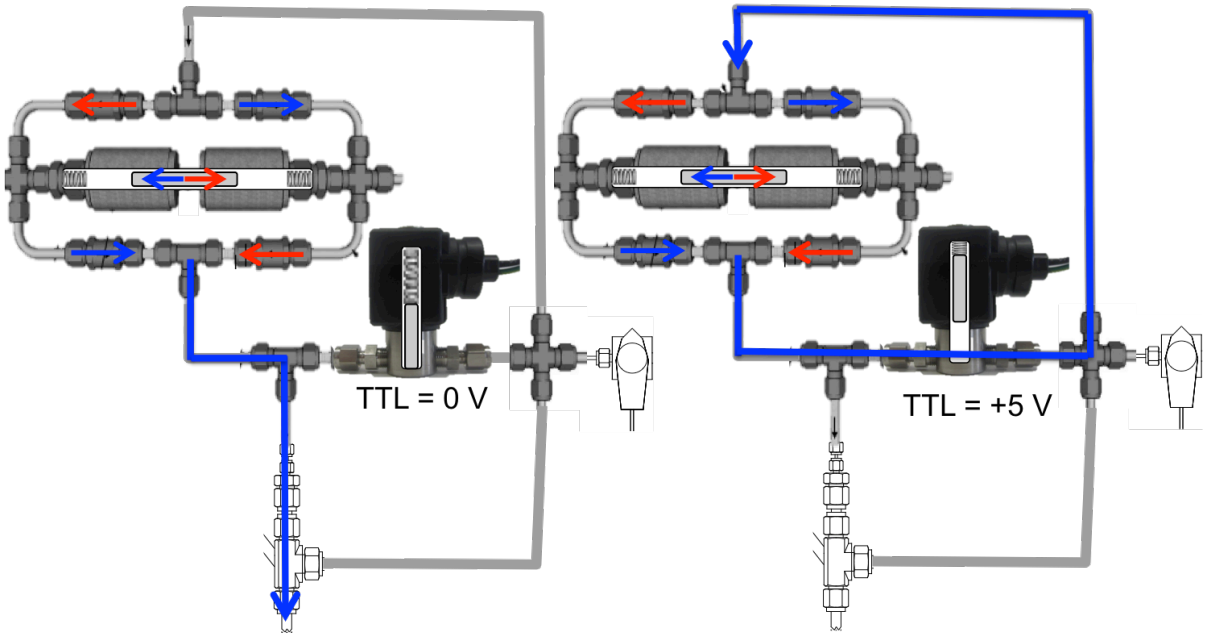

Figure 3.3. The compact circulator mechanism. When it is signaled ON (left), the solenoid valve is closed and the gas flows to the NMR tube. When it is signaled OFF (right), the solenoid valve is open and the gas flows around the circulator with no gas flow to the NMR tube.

Spectrum quality is maintained by turning the circulator off during data acquisition, and back on when not actively acquiring data. The circulator inlet and outlet are connected with a solenoid valve in order to control the flow of gas. When this bypass valve is open, gas flowing out from the circulator follows the path of least resistance back to the inlet of the circulator, resulting in no flow through the NMR sample (Figure 3.3, right). When the bypass valve is closed, flow continues through the capillary tube submerged in the NMR sample as described in the gas delivery system (Figure 3.3, left). The solenoid bypass valve is controlled by a signal sent from the spectrometer; the signal is integrated as a part of the

pulse program. An example pulse program, used for acquisition of a ^{1}H NMR spectrum, is shown in Figure 3.4. The normal relaxation delay before the excitation pulse is split into two intervals. The solenoid valve is normally open (no circulation) until the first TTL signal closes the solenoid valve and circulates gas throughout the first delay period, d1. At the end of d1, the solenoid valve opens – stopping the circulation through the sample – and is followed by the second delay, d2, during which gas bubbles in solution dissipate before the NMR excitation pulse and data acquisition sequence. These two delays are, therefore, called circulation delay and bubble dissipation delay, respectively. Adjusting these delays controls the fraction of reaction time (or duty cycle) during which gas is actively circulated. Commonly, the bubble dissipation delay is set to 0.5 s, enough for all bubbles to disappear, while the circulation delay is maximized for good gas-liquid mixing. The sum of d1 and d2 is equivalent to the interpulse relaxation delay and should still be more than five times of the longest T1 for an accurate quantitative analysis. In common applications the duty cycle is 70% or greater meaning that gas is bubbling during 70% or more of the total reaction time.

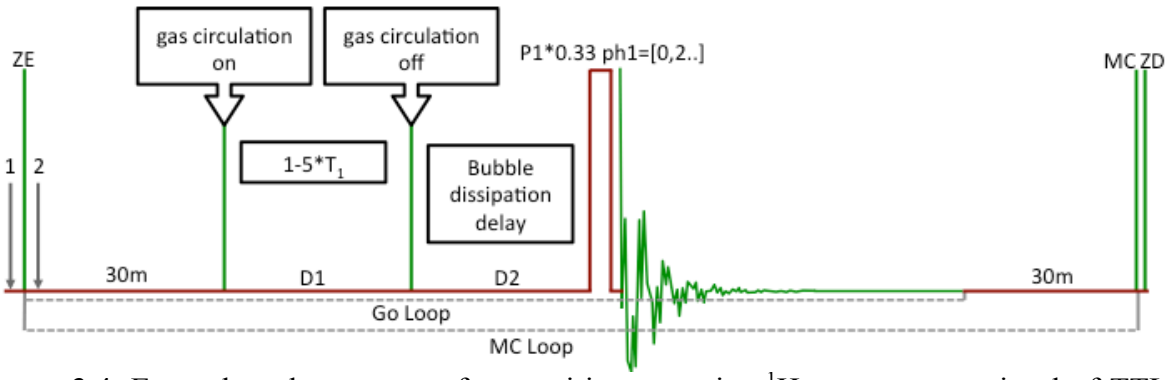

Figure 3.4. Example pulse program for acquiring a routine ^{1}H spectrum consisted of TTL signals to turn the circulator on and off.

d) Liquid delivery system. The liquid injection system connects to the inner tubing sharing it with the gas delivery feed route down to the capillary inside the NMR tube. The

gas and liquid delivery system are, however, separated by a three-way injection selector valve, i.e., when the NMR tube reactor is open to one, the other is closed automatically. There are two injection ports, manual and HPLC (See Figure 3.1, liquid delivery system). The manual injection port receives liquid from a syringe injected by hand. This port is good for injection at ambient pressure; commonly this port is used for all additions that can be made without high pressure (solvents, some reactants, catalyst precursors). For liquid injection to the system under high pressure, the HPLC port is used. The initial injection through this port is also from syringe by hand, but instead of going straight to the NMR tube, which is not possible under high pressure, the liquid injected runs through an HPLC valve into small loop of tubing. When the HPLC valve is turned, liquid inside the loop is pushed down to the NMR tube with high pressure gas (N_2 or reaction gas) connected to the other side of the HPLC valve. In use, the loop is usually filled with reaction solvent before loading the solution of desired compound. Because what is loaded into the loop later is injected to the system first (last in, first out), the prefilling solvent then serves as a chaser to wash down any sample solution that might be wetting the tubing wall during injection.

e) Wash system. The wash system contains a thick-walled pressure bottle connected to the recycle side of the gas delivery system. To clean the WiHP-NMRR, the bottle is filled with the washing solvent, the selector valve is open to the liquid delivery system (see above), and the manual sample injection port is attached with a waste bottle. Turning the injection/gas feed selector valve to the liquid injection side automatically closes the system to gas deliverty through this valve. Low N_2 pressure (ca. 15 psig) introduced to the wash bottle pushes solvent through the recycle route down to the NMR tube. The solvent washes the wall of the outer tubing that attaches to the titanium holder and then is forced out of the system

through the inner capillary and injection port, similar to the method of cannula transfer on a Schlenk line. Thus, all parts of the reactor that contact liquid are rinsed thoroughly. After rinsing with several cycles of washing solvent, the reactor is purged and dried with N_2 and then evacuated to remove all solvent residues. The active washing process usually takes less than 20 minutes. Not having to uninstall/reinstall the WiHP-NMRR apparatus for cleaning reduces both the amount of time consumed in setup, and also the chances of leakage or major changes in magnetic field shim settings after each reaction.

3.3 Monitoring of Overall MRC Reaction Catalyzed by Rh-dppp Catalyst

The kinetics of the overall MRC reaction was monitored with ^{2}H NMR spectroscopy by injecting CD_3I substrate to a solution of the monocarbonyl Rh-iodo complex **1-I** in 50%(v/v) MeOH/sulfolane under the syngas pressure of interest at 90 °C (Figure 3.5). The ^{2}H NMR allows direct observation of the CD_3I starting material, the desired MRC product $CD_3CH(OCH_3)_2$ (formed spontaneously from acetaldehyde and methanol), the CD_3COOCH_3 side product (from acyl iodide and methanol), and CD_3H. In order to ensure that the reaction is not starved of dissolved gas, the reactor pressure was regulated by continuous feed of 1:1 H_2/CO that was circulated at 17 mL/min, 70% duty cycle. However, because of the volatile nature of many components in the sample, mass loss due to evaporation is inevitable with this rate of gas circulation and high working temperature conditions; thus preventing a normal kinetic time course analysis of the decay of starting material and the growth of the products over time. In this situation, reaction progress kinetics analysis, where instantaneous rate at each time point is calculated and plotted against substrate concentration, is a more appropriate method to obtain kinetic parameters.

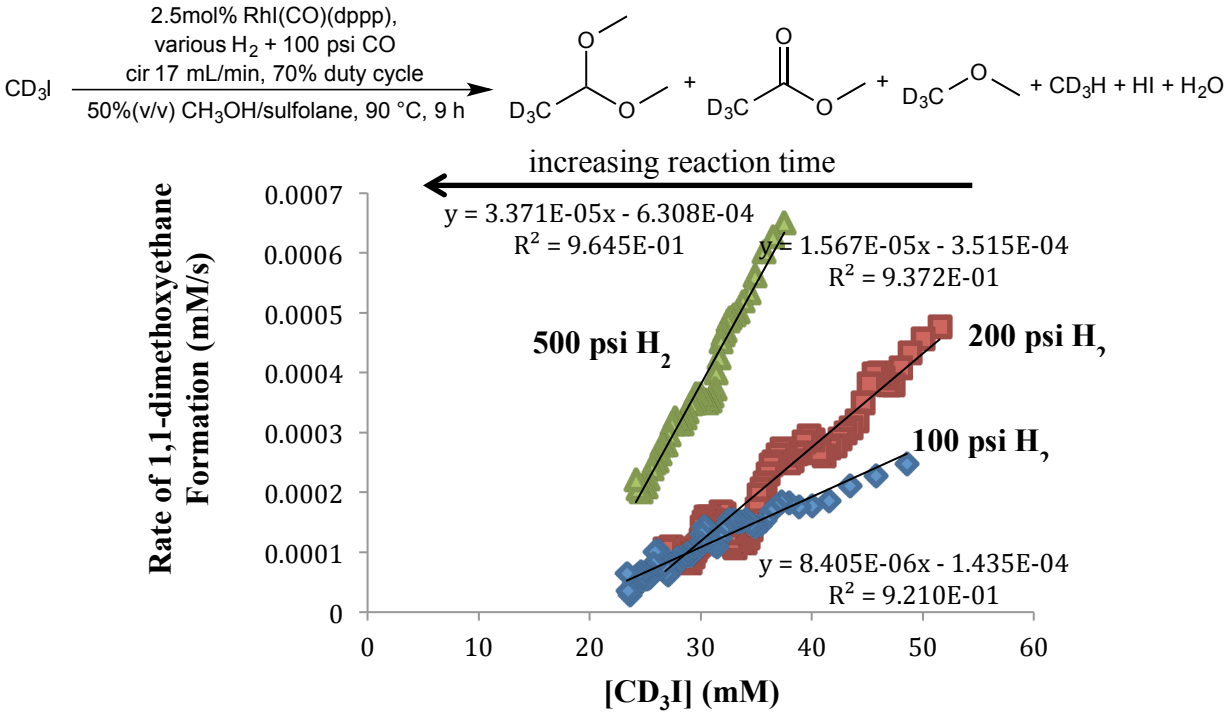

Figure 3.5. Reaction progress as measured by 1,1-dimethoxyethane formation at various H_2 pressure. Note that the reaction progresses from high to low concentration of CD_3I, i.e., from right to left of the plot.

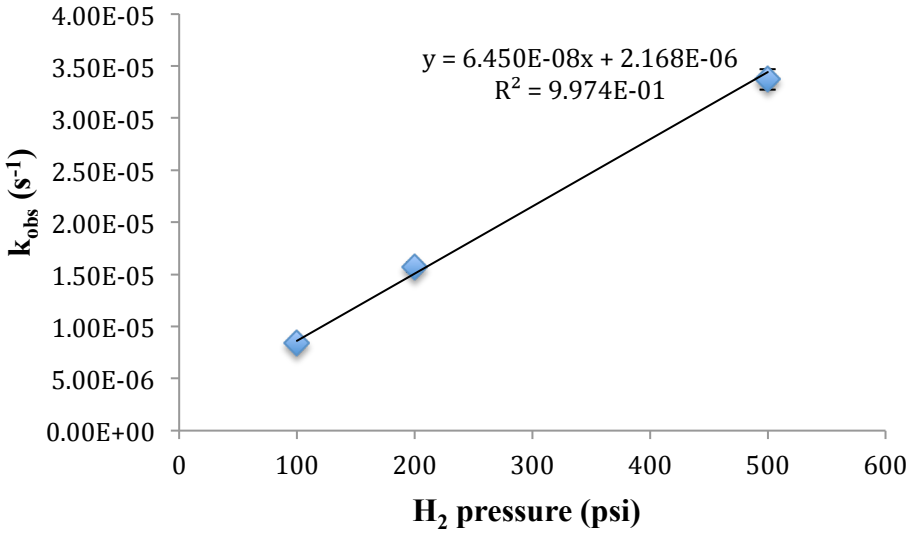

Figure 3.6. Plot of k_{obs} obtained from reaction progress analysis vs H_2 pressure.

Investigation of the H_2 dependency of the reaction rate was conducted under constant

CO partial pressure and varied H_2 partial pressure. The plots of the instantaneous rate of 1,1-dimethoxyethane formation against concentration of CD_3I (Figure 3.5) reveal correlation between the rate and H_2 partial pressure. Slopes *taken from the linear region* of the plots of instantaneous rate plots as a function of instantaneous [CH_3I] depend on the H_2 partial (Figure 3.6). Initially, this analysis seemed to fit well with the rate law:

$$Rate = k'[H_2][CH_3I]$$

where slopes or k_{obs} in the instantaneous rate plot is equal to $k'[H_2]$.

This apparent rate law, however, does not agree with kinetic measurements by Wegman and Moloy and by Dow that suggest a zero-order dependence on [CH_3I]. Moreover, the Rh-acetyl **D-3-Ac (Scheme 3.1)** was observed as the dominant Rh-containing species throughout the reactions, suggesting that it is the resting state which requires that the oxidative addition of CD_3I is fast relative to hydrogenolysis. We also noticed the non-zero x-intercept in the plots of k_{obs} vs. P_{H2}. It is important to note that in this plot of reaction progress kinetics analysis, the reaction timecourse progresses from the right, where the concentration of CD_3I is high, to the left, where the concentration of CD_3I is low. A non-zero x-intercept, therefore, means that at a certain point before all CD_3I is consumed, the reaction shuts down. This behavior agrees better with a scenario where product inhibition occurs rather than the first order kinetics. Based on our proposed ionization mechanism and the fact that the rate slows down as CD_3I is consumed, we hypothesized that the inhibition arises from an increase in the concentration of iodide ion (produced as HI, which then ionizes) as CD_3I is consumed. This proposed inhibition by iodide was tested by intentionally adding the iodide salt, Ph_3EtPI, to the reaction. A similar decrease in the rate of the reaction was observed when a higher concentration of iodide ions was present.[8]

Scheme 3.1. Simplified ionization kinetic model and HI formation pathway.

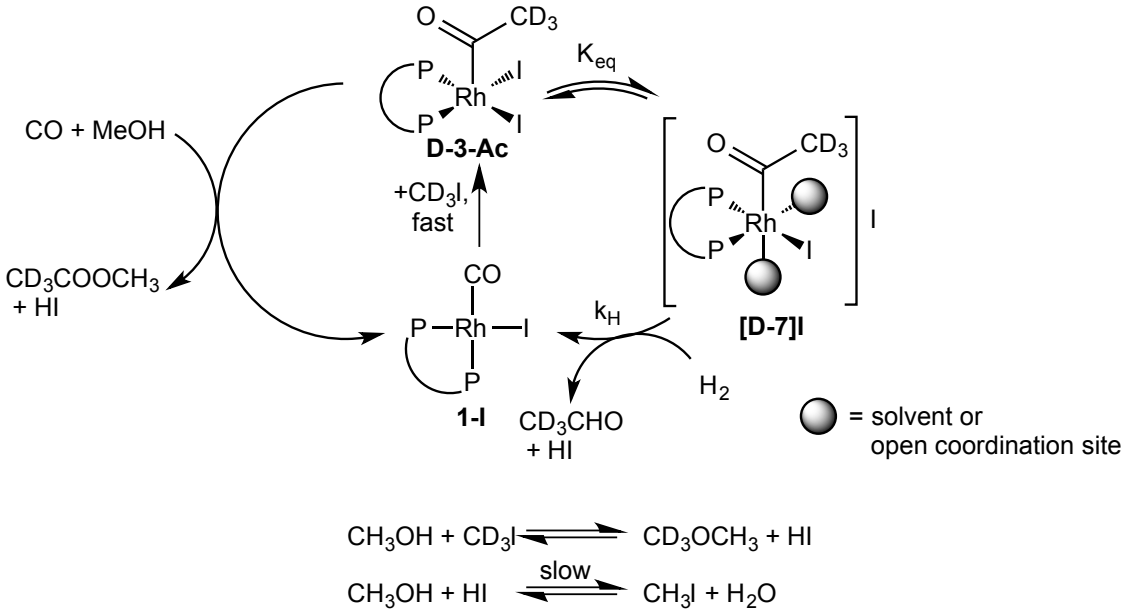

To better understand the inhibition behavior, we devise a simplified model according to our hypothesis shown in Scheme 3.1. The production of 1,1-dimethoxyethane is controlled by the concentration of ionized species **[D-7]I** and H_2 according to the rate law:

$$Rate = k_H[\textbf{[D-7]I}][H_2] \qquad (3.3)$$

With the assumption that the oxidative addition is fast so that **1-I** is at negligible steady state concentration, we can derive the following relationships for the concentration of **D-3-Ac**.

$$[Rh] = [\mathbf{1\text{-}I}] + [\mathbf{D\text{-}3\text{-}Ac}] + [\mathbf{[D\text{-}7]I}]$$

[**1**] is negligible when CD_3I oxidative addition is fast

$$\begin{aligned}[Rh] &= [\mathbf{D\text{-}3\text{-}Ac}] + [\mathbf{[D\text{-}7]I}]] \\ &= \frac{[\mathbf{[D\text{-}7]I}][I^-]}{K_{eq}} + [\mathbf{[D\text{-}7]I}] \\ &= [\mathbf{[D\text{-}7]I}]\left(1 + \frac{[I^-]}{K_{eq}}\right) \\ [\mathbf{[D\text{-}7]I}] &= \frac{[Rh]}{1 + \frac{[I^-]}{K_{eq}}} \end{aligned} \tag{3.4}$$

When the reaction is run at the higher temperature, 140 °C for catalytic conditions, the conversion of HI back to CH_3I in methanol is fast enough that CH_3I is present in excess at all times, which is not necessarily true for our reaction at 90 °C. We hypothesize that the converstion of iodide ion (as HI) into CH_3I and water is slow compared to its formation under the lower temperature conditions of our study. Thus iodide accumulates over the course of reaction as a function of the concentration of observable products: $CD_3CH(OCH_3)_2$, CD_3OCH_3, and CD_3COOCH_3.

$$[I^-] = C\left([CD_3CH(OCH_3)_2] + [CD_3OCH_3] + [CD_3COOCH_3]\right) \tag{3.5}$$

Substituting equation (3.4) and (3.5) into (3.3), the rate law can be written as:

$$\begin{aligned} Rate &= \frac{k_H[Rh][H_2]}{1 + \frac{[I^-]}{K_{eq}}} \\ &= \frac{k_H[Rh][H_2]}{1 + \frac{C\left([CD_3CH(OCH_3)_2] + [CD_3OCH_3] + [CD_3COOCH_3]\right)}{K_{eq}}} \end{aligned} \tag{3.6}$$

The only terms that change over the reaction period are the rate and the summation of the products, so equation (3.6) is simplified as equation (3.7) for fitting purposes.

$$Rate = \frac{a}{1 + b[Products]} \tag{3.7}$$

where

$$a = k_H[Rh][H_2]$$

$$b = \frac{C}{K_{eq}}$$

$$[Products] = [CD_3CH(OCH_3)_2] + [CD_3OCH_3] + [CD_3COOCH_3]$$

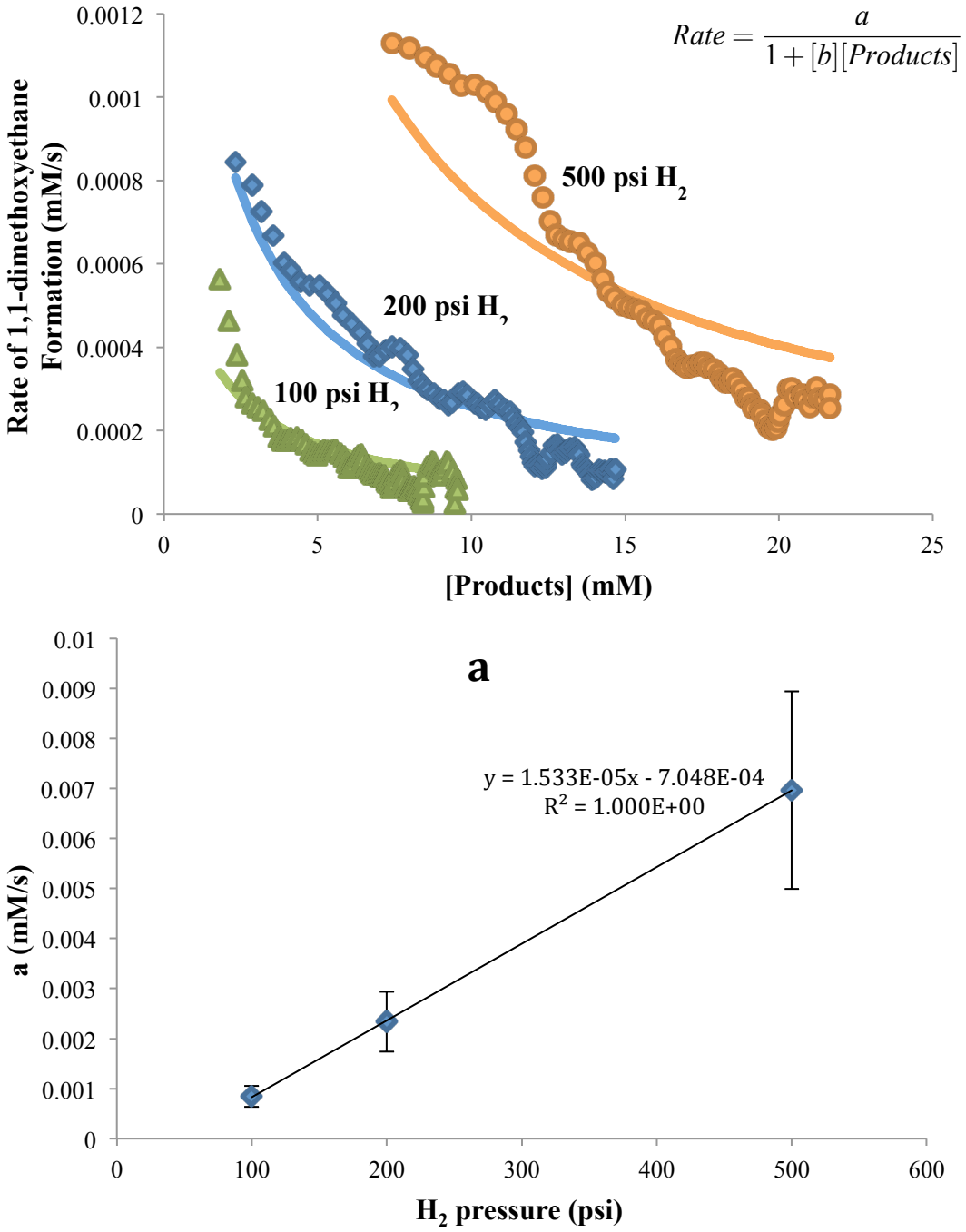

Figure 3.7. Reaction progress data fitting with solid line fitted curves (top) and H_2 dependence on parameter *a* (bottom) according to equation (3.7) for model with inhibition by iodide ions.

Table 3.1. Fitted parameters *a* and *b* from model of inhibition by iodide ions.

Parameter	Value	S.D.
a (100 psi H_2)	8.94 x 10^{-4} mM s^{-1}	2 x 10^{-4}
a (200 psi H_2)	2.06 x 10^{-3} mM s^{-1}	6 x 10^{-4}
a (500 psi H_2)	5.56 x 10^{-3} mM s^{-1}	2 x 10^{-3}
b	8.11 x 10^{-1} mM s^{-1}	3 x 10^{-1}

Although the data quality is not very good (this is a general feature of instantaneous rate analyses when the concentration differences between time points are small, making the instantaneous rates very sensitive to noise) it is consistent with the model. The reaction rate slows down as more CD_3I is converted to products, but to a lesser degree toward the end of the reaction. The parameter *a*, fitted variably in different experiments, shows linear correlation with H_2 pressure as expected, justifying the first order kinetics with respect to H_2. In contrast, the parameter *b* is fitted as a fixed parameter over the experiments. According to the fitting, we can calculate k_H from the slope of the plot of parameter *a* with H_2 pressure (Figure 3.7, bottom).

$$a = k_H[Rh][H_2]$$

$$slope = k_H[Rh]$$

$$k_H = \frac{1.53 \times 10^{-5} mM\, psi^{-1}\, s^{-1}}{4.0\ mM} = 3.8 \pm 1.2 \times 10^{-6} psi^{-1}\, s^{-1}$$

Unfortunately, the WiHP-NMRR, still under development at the time that these experiments were being conducted, was not very robust and required regular maintenance, preventing us from collecting data at exactly the same reaction conditions for comparison. Other sets of experiments were carried out to provide a fuller description of the reaction mechanism.

3.4 Monitoring Oxidative Addition of CH_3I to RhI(CO)(P^P)

In the characterization work described in the previous chapter, monocarbonyl Rh-iodo complex **1-I** has been found to form dicarbonyl Rh-iodo complex **4-I** under an atmosphere of CO (Scheme 3.2). The five-coordinate complex **4-I** is an $18e^-$ coordinatively saturated complex, so we expect it to be unreactive with CH_3I unless CO dissociates. In order to test the hypothesis, the oxidative addition reaction of CH_3I to **1-I** was investigated kinetically in the presence and absence of CO.

Scheme 3.2. Equilibrium between **1-I** and **4-I** under an atmosphere of CO

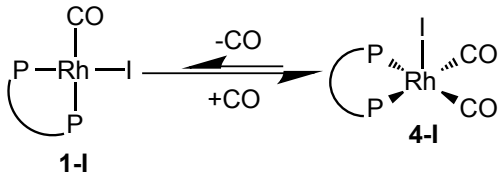

Our preliminary investigation of the reaction by ^{31}P NMR spectroscopy revealed that there are four observable complexes involved in the reaction: starting material **1-I**, two isomeric intermediates, **2-Me(maj)** and **2-Me(min)**, and final product **3-Ac** as shown in Scheme 3.3. Only the major isomer **2-Me(maj)** of two intermediate species possesses the *cis* arrangement of methyl and CO ligands that is required for migratory insertion to the final product. Although seen initially, the minor isomer **2-Me(min)** is not observed at the end of the reaction. In fact, complex **3-Ac** was the only observed species after the reaction had been completed. These data suggest that the formation of isomer **2-Me(min)** is reversible, while formation of **3-Ac** is irreversible, or its reverse reaction is negligible under the reaction conditions. Our kinetic model, also shown in Scheme 3.3, was devised accordingly.

Scheme 3.3. Kinetic model of oxidative addition of CH_3I to **1-I**.

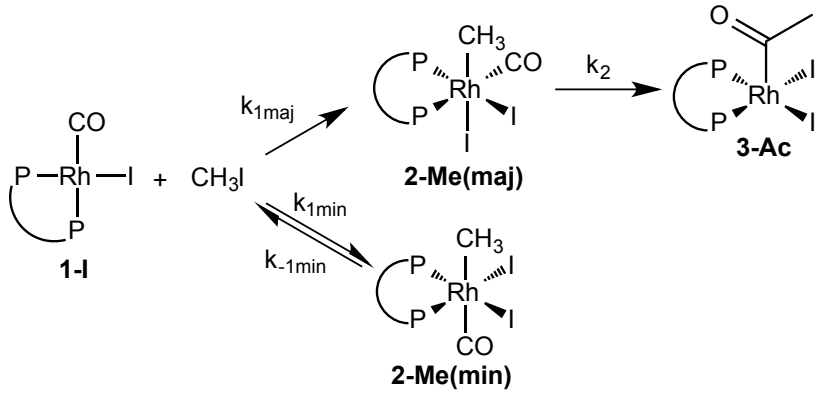

*3.4.1 Monitoring Reaction of CH_3I to **1-I** in the absence of CO*

This oxidative addition event, in the absence of CO, was monitored by ^{31}P NMR spectroscopy at 0 °C in CH_2Cl_2 and fitted to the kinetic model with Copasi software. Figure 3.8 and Figure 3.9 show that the time course data of all rhodium species fit very well with our model and the rate of reaction correlates with the concentration of CH_3I. The kinetic parameter associated with each step is also shown in Table 3.2. The rate constant for the formation of the major intermediate is about 7 times greater than that for the formation of the minor one. The analytical solution for this type of rate law, bimolecular consecutive reaction, can be very complicated, but the plots shows that about after 3000 s, the intermediate **2-Me(maj)** has built up to almost constant concentration, which allowed us to use the steady state approximation for qualitative interpretation, even though not all conditions for the steady state approximation are satisfied. In the approximation, after the concentration of **2-Me(maj)** reaches the steady state, the rate of formation of **3-Ac** is controlled by the oxidative addition reaction, k_{1maj}[**1-I**][CH_3I].

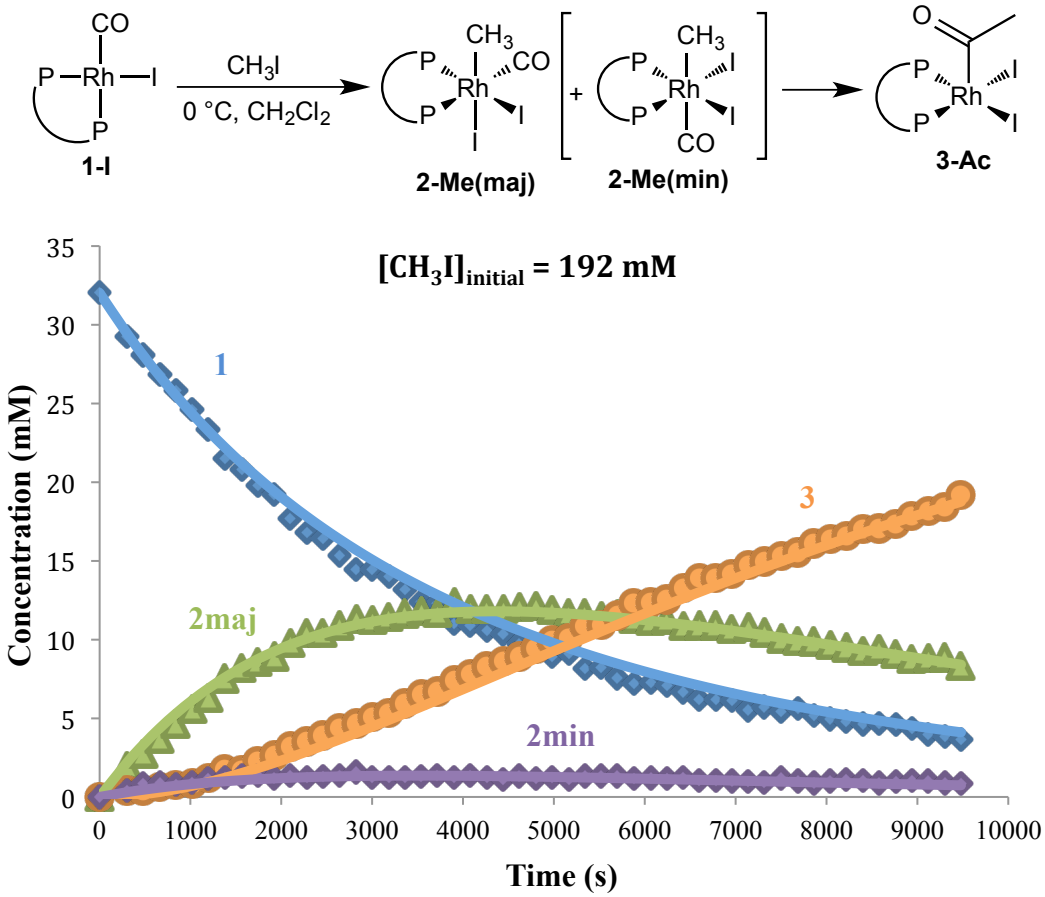

Figure 3.8. Oxidative addition of CH_3I to **1-I** at 0 °C in CH_2Cl_2 monitored by ^{31}P NMR spectroscopy, experimental data shown as solid symbols and fitted curves shown as solid lines. (See appendix for data at the other initial concentration of CH_3I).

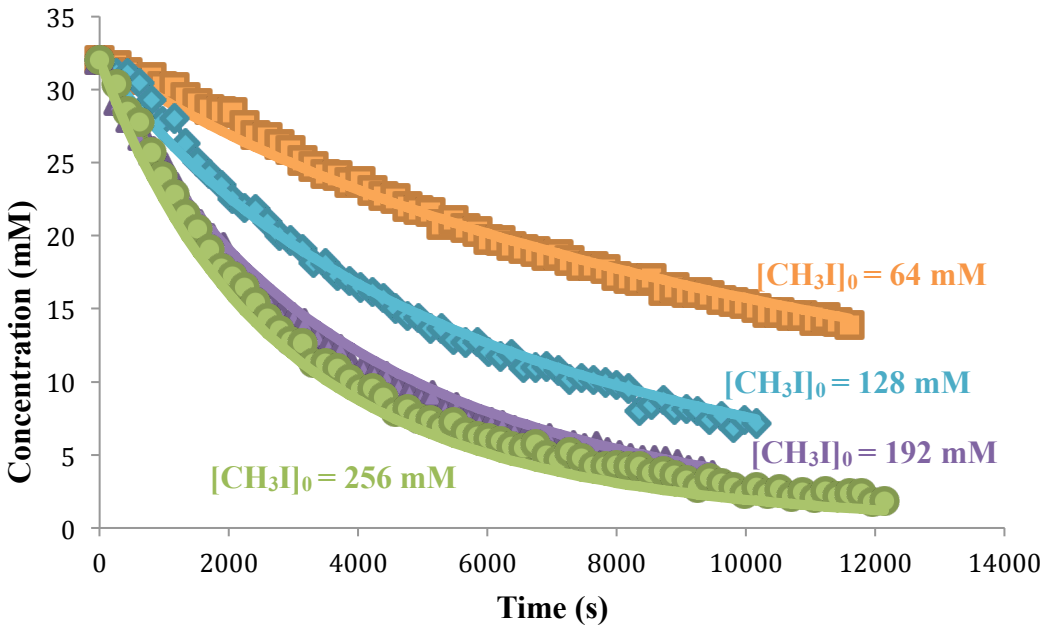

Figure 3.9. Plot showing the decay of **1-I**, only, during reaction with CH_3I in the absence of CO. Initial concentration of CH_3I are 64, 128, 192, and 256 mM (top to bottom), experimental data shown as solid symbols and fitted curves shown as solid lines.

Table 3.2. Fitted parameters (top) and correlation matrix[†] (bottom) (parameters associated with Scheme 3.2) for oxidative addition of CH_3I to **1-I** in the absence of CO at 0 °C in CH_2Cl_2.

Parameter	Value	S.D.
k_{1maj}	1.28×10^{-6} mM^{-1} s^{-1}	7.0×10^{-10}
k_{1min}	1.80×10^{-7} mM^{-1} s^{-1}	2.0×10^{-9}
k_{-1min}	3.11×10^{-4} s^{-1}	4.6×10^{-6}
k_2	2.07×10^{-4} s^{-1}	1.5×10^{-7}

Parameter	k_2	k_{1maj}	k_{1min}	k_{-1min}
k_2	1	-0.166208	0.12434	0.108902
k_{1maj}	-0.166208	1	0.254062	0.257829
k_{1min}	0.12434	0.254062	1	0.896173
k_{-1min}	0.108902	0.257829	0.896173	1

[†] The correlation matrix provides the correlation between fitted parameters. The closer the correlation in the matrix to 1 or -1, the stronger positive or negative correlation, respectively, between corresponding parameters. When two parameters are strongly correlated, their values cannot be determined independently. In this case the values of k_{1min} and k_{-1min} are not well-determined.

*3.4.2 Monitoring Reaction of CH_3I to **1** in the presence of CO*

The oxidative addition reactions were performed under CO atmosphere for comparison with the results shown in Figure 3.10. In spite of the similarity in the experimental procedure, it is important to note that the starting complex **1-I** had been converted completely under CO to a saturated complex **4-I** before CH_3I was injected. Therefore, the reaction is monitored as if **4-I** is the starting material. Moreover, the reactions conducted under atmospheric pressure of CO are much slower than reactions conducted in the absence of CO, necessitating an increase of the reaction temperature to 25 °C and increased initial concentration of CH_3I in order to have the reaction proceed at an appreciable rate. Figure 3.11 shows the decrease in the rate of reaction when CO is present at 25 °C. The kinetic model is shown in Scheme 3.4. According to our hypothesis, CO dissociation from dicarbonyl complex **4-I** to generate **1-I** is added to our model as the first step for the mechanism. The complexes **4-I** and **3-Ac** were observed as major species during the reaction while the major isomer of the intermediates, **2-Me(maj)**, was also observed at a small steady state concentration. The monocarbonyl complex **1-I** is consumed quickly once it forms, so it does not accumulate to high enough concentration to be visible by NMR spectroscopy.

Scheme 3.4. Kinetic model for oxidative addition of CH_3I to **1-I** under CO.

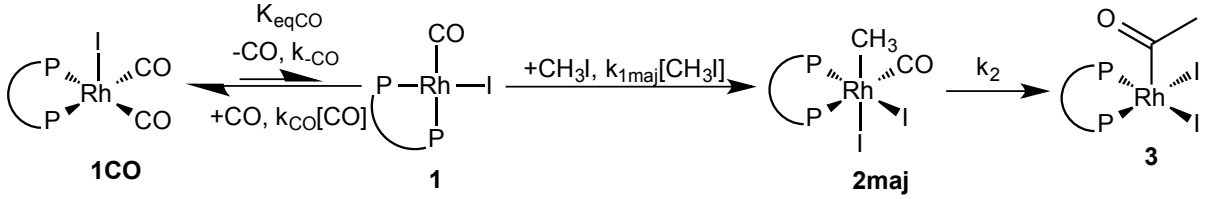

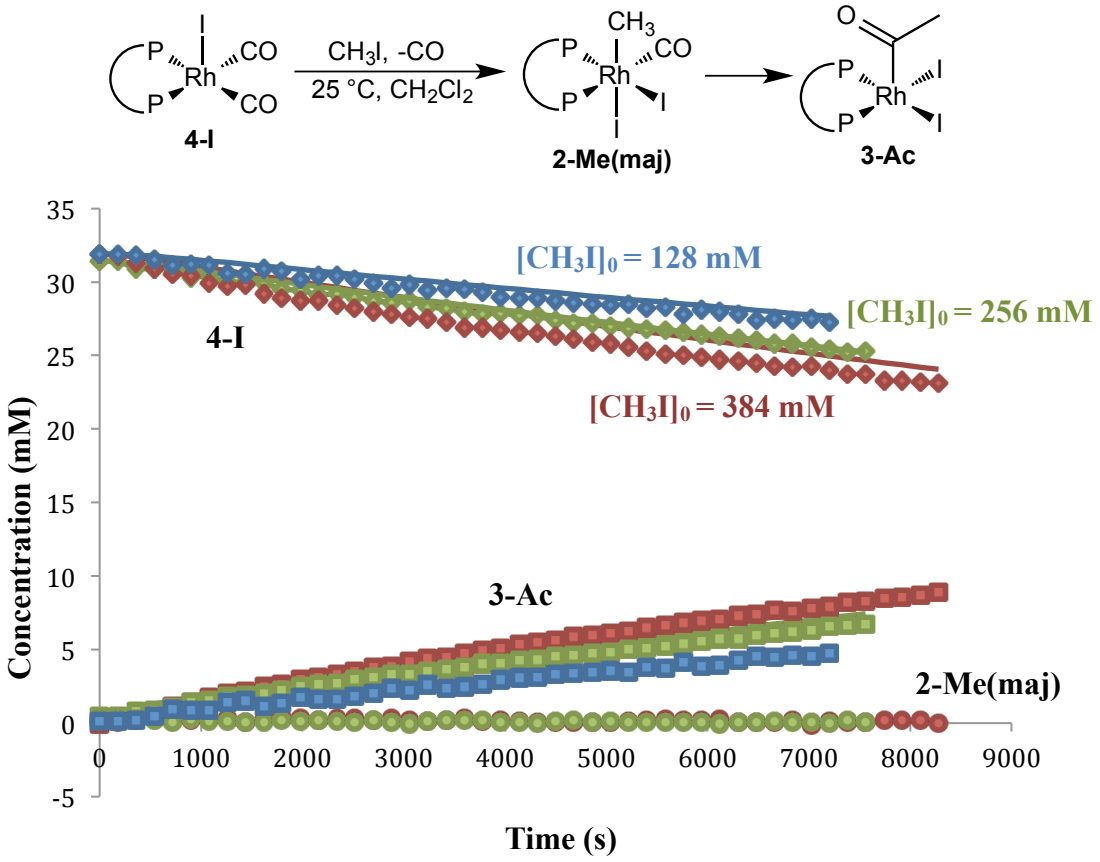

Figure 3.10. Oxidative addition of CH_3I to **1-I** in CH_2Cl_2 at 25 °C under an atmospheric pressure of CO with initial concentration of CH_3I of 128 (blue), 256 (green), and 384 (red) mM monitored by ^{31}P NMR spectroscopy), experimental data shown as solid symbols and fitted curves shown as solid lines.

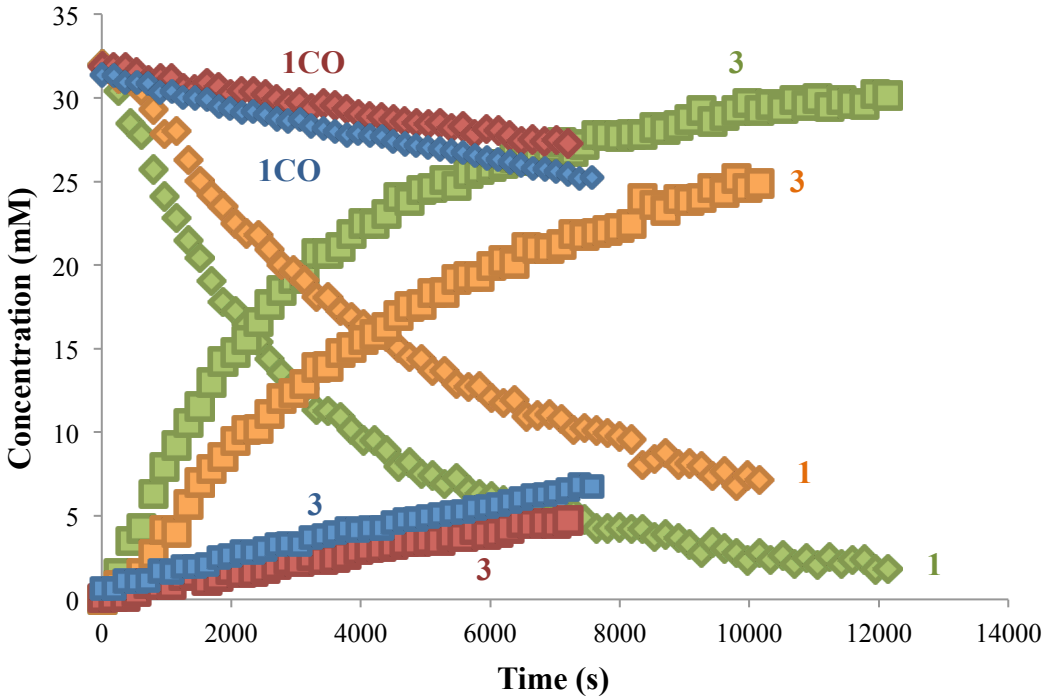

Figure 3.11. Comparison between the oxidative addition of CH_3I to **1-I** in the presence (25 °C, $[CH_3I]_0$ = 128 (red) and 256 (blue) mM) and absence (0 °C, $[CH_3I]_0$ = 128 (yellow) and 256 (green) mM of CO.

Table 3.3. Fitted parameters (top) and correlation matrix (bottom) (parameters associated with Scheme 3.4) for oxidative addition of CH_3I to **1-I** in the presence of CO at 25 °C in CH_2Cl_2.

Parameter	Value	S.D.
k_{-CO}	5.19×10^{-5} s^{-1}	2.2×10^{-7}
k_{CO}	1.03×10^{-7} $mpsi^{-1}s^{-1}$‡	5.0×10^{-9}
k_{1maj}	8.51×10^{-6} $mM^{-1}s^{-1}$	4.0×10^{-7}
k_2	6.85×10^{-3} s^{-1}	2.3×10^{-4}

Parameter	k_2	k_{1maj}	k_{-CO}	k_{CO}
k_2	1	-0.0185735	0.100166	0.01866
k_{1maj}	-0.0185735	1	0.0611785	0.980484
k_{-CO}	0.100166	0.0611785	1	0.250553
k_{CO}	0.01866	0.980484	0.250553	1

‡ Concentration of CO is used as partial pressure at mpsi (15,000 mpsi at atmospheric pressure) to make CO concentration large and relatively unchanged during the experiment.

From our kinetic model, we can derive the rate law of decay of **4-I** as follows.

$$\frac{d[3-Ac]}{dt} = k_2[\textbf{2-Me(maj)}]$$

$$\frac{d[\textbf{2-Me(maj)}]}{dt} = k_{1maj}[\textbf{1-I}][CH_3I] - k_2[\textbf{2-Me(maj)}] = 0 \qquad \text{by steady state approximation}$$

$$[\textbf{2-Me(maj)}] = \frac{k_{1maj}[\textbf{1-I}][CH_3I]}{k_2}$$

$$\frac{d[\textbf{3-Ac}]}{dt} = k_2\left(\frac{k_{1maj}[\textbf{1-I}][CH_3I]}{k_2}\right)$$

$$= k_{1maj}[\textbf{1-I}][CH_3I]$$

Assume the reaction to and from **2-Me(min)** is negligible

$$\frac{d[\textbf{1-I}]}{dt} = k_{-CO}[\textbf{4-I}] - k_{CO}[\textbf{1-I}][CO] - k_{1maj}[\textbf{1-I}][CH_3I] = 0 \quad \text{by steady state approximation}$$

$$[\textbf{1-I}] = \frac{k_{-CO}[\textbf{4-I}]}{k_{CO}[CO] + k_{1maj}[CH_3I]}$$

$$\frac{d[\textbf{3-Ac}]}{dt} = k_{1maj}[CH_3I]\left(\frac{k_{-CO}[\textbf{4-I}]}{k_{CO}[CO] + k_{1maj}[CH_3I]}\right)$$

$$\frac{d[\textbf{3-Ac}]}{dt} = \frac{k_{-CO}k_{1maj}[CH_3I][\textbf{4-I}]}{k_{CO}[CO] + k_{1maj}[CH_3I]} \qquad (3.8)$$

The rate expression in equation (3.8) shows that dissociation of CO should strongly affect the reaction rate. As the rate is proportional to k_{-CO} but inversely proportional to k_{CO}[CO], the apparent rate constant with respect to concentration of Rh catalyst and CH_3I is much lower than the rate in the absence of CO. Based on the calculated rate laws, the initial rate of **3-Ac** formation at initial concentration of CH_3I of 128 mM in the absence of CO is about 7.5 times faster than the same reaction in the presence of CO, even if one disregards the 25 °C increase in temperature. Note that k_{1maj} for the two conditions cannot be compared directly, even after the temperature change is taken into account, because the concentration of **1-I** is extremely small and cannot be measured directly in the presence of CO. The small

error in estimation can lead to orders of magnitude of error in k_{1maj}. Furthermore, for reactions performed under a CO atmosphere the rate constants for k_{1maj} and k_{CO} are strongly correlated (0.98) and their values cannot be determined independently.

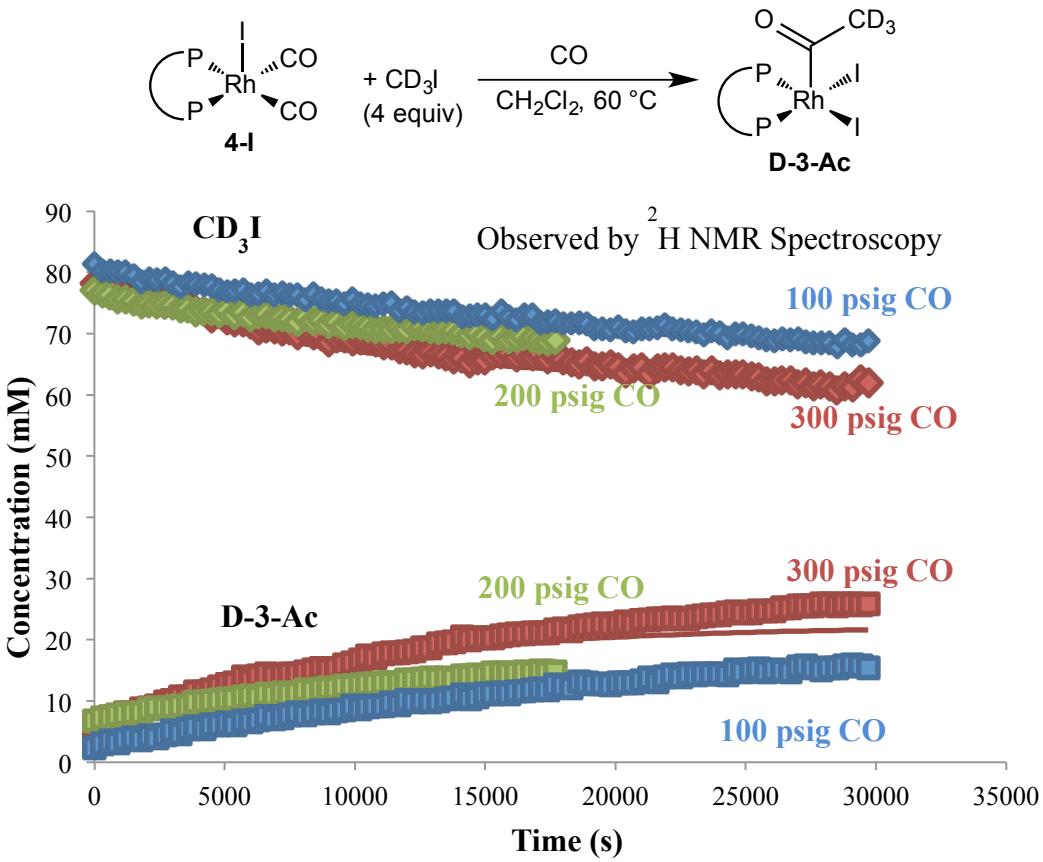

Figure 3.12. Oxidative addition of CD_3I to **1-I** under high CO pressure at 60 °C, observed by ^2H NMR spectroscopy. Experimental data is shown as solid symbols and fitted curves shown as solid lines.

Scheme 3.5. Kinetic model for oxidative addition of CD_3I to RhI(CO)(dppp) under high pressure of CO.

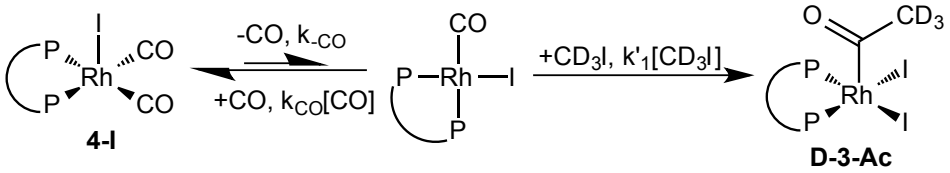

Table 3.4. Fitted parameters (top) and correlation matrix (bottom) (parameters associated with Scheme 3.5) for oxidative addition of CH_3I to **1-I** under high pressure of CO at 60 °C in CH_2Cl_2.

Parameter	Value	S.D.
k_{-CO}	1.18×10^{-1} s^{-1}	2.7
k_{CO}	8.93×10^{-2} $mpsi^{-1}s^{-1}$	1.1
k'_2	1.18×10^{-1} $mM^{-1}s^{-1}$	2.4

Parameter	k'_2	k_{-CO}	k_{CO}
k'_2	1	-0.840814	0.0634908
k_{-CO}	-0.840814	1	0.486848
k_{CO}	0.0634908	0.486848	1

On the other hand, reactions at higher CO pressures were carried out at 60 °C to observe the effect of CO partial pressure. Under these conditions, the reactions were monitored by ^2H NMR spectroscopy (Figure 3.12) by using CD_3I substrate because ^{31}P NMR signals were too broad to be reliable for quantitative analysis. Although the change in rate is subtle under these conditions, it is obvious that the dependency on CO pressure is less pronounced. It is reasonable that the equilibrium constant for endothermic CO dissociation is larger as the temperature increases. The rate law of product **3-Ac** formation (equation (3.9)) according to the model can be derived by the steady state approximation, similar to equation

(3.8).

$$\frac{d[\mathbf{3\text{-}Ac}]}{dt} = \frac{k_{-CO}k_1'[CH_3I][\mathbf{4\text{-}I}]}{k_{CO}[CO] + k_1'[CH_3I]} \qquad (3.9)$$

For comparison, the initial rate of the oxidative addition and overall reactions at 25 °C and 60 °C, when conducted under 500 psi H_2, 100 psi CO, $[CH_3I]_0$ = 128 mM, and $[Rh]_0$ = 4.0 mM, are calculated using parameters from Tables 3.3, 3.4, and 3.1 respectively.

Oxidative addition at 25 °C

$$Rate = \frac{(5.19 \times 10^{-5} s^{-1})(8.51 \times 10^{-6} mM^{-1} s^{-1})(128\ mM\ CH_3I)(4.0\ mM\ Rh)}{(1.03 \times 10^{-7} mpsi^{-1} s^{-1})(10^5 mpsi\ CO) + (8.51 \times 10^{-6} mM^{-1} s^{-1})(128\ mM\ CH_3I)}$$

$$= 1.98 \times 10^{-5}\ mM\, s^{-1}$$

Oxidative addition at 60 °C

$$Rate = \frac{(1.18 \times 10^{-1} s^{-1})(1.18 \times 10^{-1} mM^{-1} s^{-1})(128\ mM\ CH_3I)(4.0\ mM\ Rh)}{(8.93 \times 10^{-2} mpsi^{-1} s^{-1})(10^5 mpsi\ CO) + (1.18 \times 10^{-1} mM^{-1} s^{-1})(128\ mM\ CH_3I)}$$

$$= 7.97 \times 10^{-4}\ mM\, s^{-1}$$

Overall reaction at 90 °C

$$Rate = (3.8 \times 10^{-6}\ psi^{-1}\ s^{-1})(500\ psi\ H_2)(4.0\ mM\ Rh)$$

$$= 7.6 \times 10^{-3}\ mM\, s^{-1}$$

Using the crude approximation that rate doubles for every 10 degrees increase in temperature from 60 °C to 90 °C, the oxidative addition rate at 90 °C would be 6.38 x 10^{-3} mM s^{-1}. This is slightly lower than the rate of overall reaction at 90 ºC. Comparison of the rate of oxidative addition at 25 °C and 60 °C shows that the rate increases about 40 times over a 35 °C temperature increase, more than the approximately 13-fold increase expected based on doubling of the rate every 10°C. This could, as mentioned above, be due to the

change of equilibrium constant of CO dissociation. Hence, we can reasonably assume that the rate of oxidative addition at 90 °C is substantially larger than the rate of overall reaction, which agrees with the hypothesis that hydrogenolysis is the rate determining step under our experimental conditions.

*3.4.3 Monitoring Reaction of CH_3I to **1-I_{OEt}** in the absence of CO.*

The kinetics of the oxidative addition of CH_3I and the subsequent CO insertion were studied in the dpppOEt ligand system. Unfortunately, the signal sharpness of Rh-dpppOEt complexes is much poorer than that of dppp complexes, and several peaks overlap in the ^{31}P NMR spectrum. Thus, the Rh-methyl intermediate from the oxidative addition step and the Rh-acetyl final products from CO insertion cannot be measured separately. All of the species formed after oxidative addition were combined for fitting with the model to extract the rate information.

Under the same reaction conditions as dppp, 0 °C in the absence of CO, we found that the data fit well with the first order kinetics with respect to the RhI(CO)(dpppOEt) starting material. The rate constant of 1.34×10^{-6} mM^{-1} s^{-1} is similar to the rate constant of 1.28×10^{-6} mM^{-1} s^{-1} for the oxidative addition of CH_3I to the corresponding dppp complex.

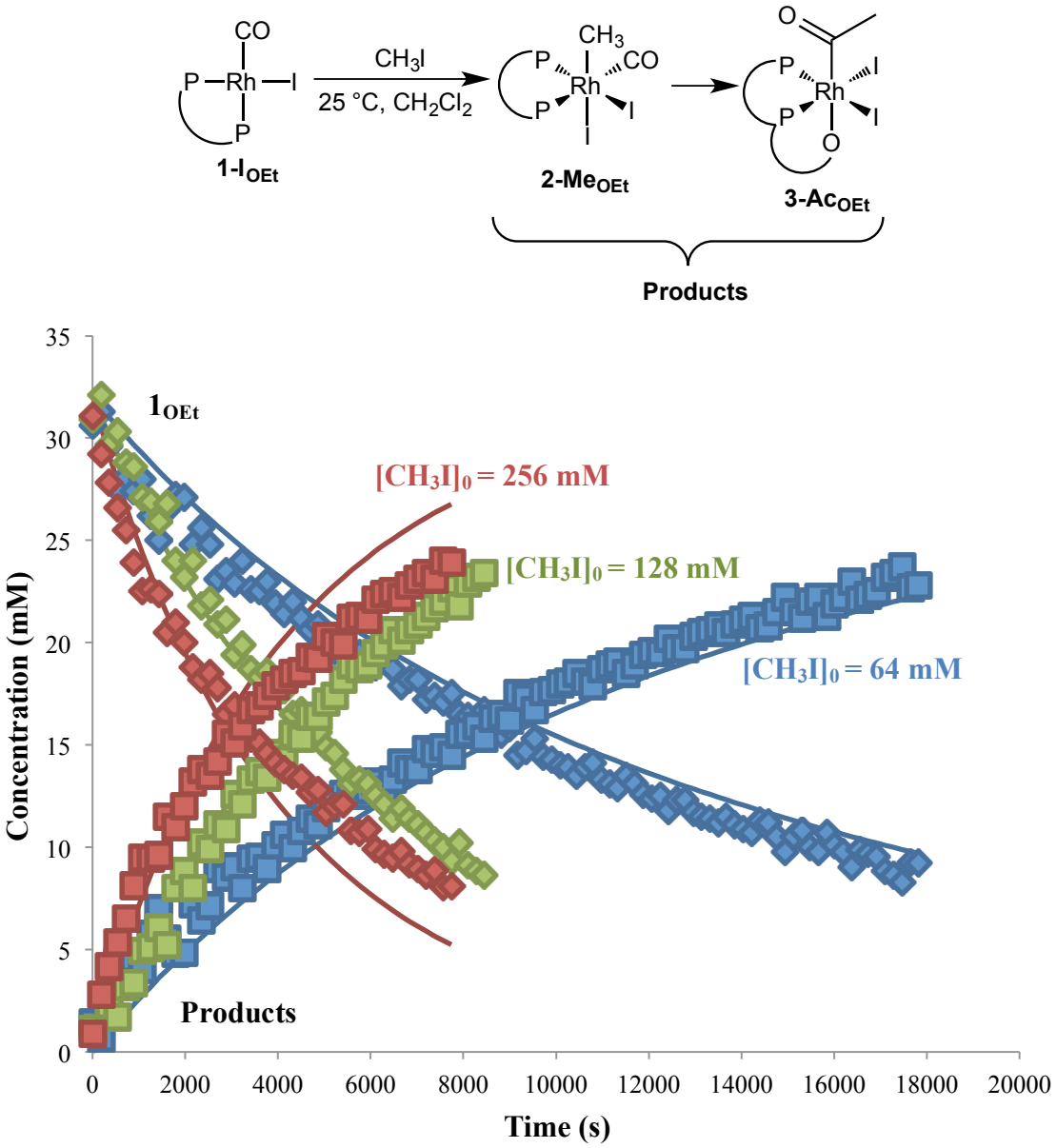

Figure 3.13. Oxidative addition of CH_3I to **1-I$_{OEt}$** at 0 °C in CH_2Cl_2 at initial concentration of CH_3I of 64 (blue), 128 (green), and 192 (red) mM monitored by ^{31}P NMR, experimental data shown as solid symbols, and fitted curves shown as solid lines.

Scheme 3.6. Kinetic model for oxidative addition of CD_3I to **1-I$_{OEt}$**

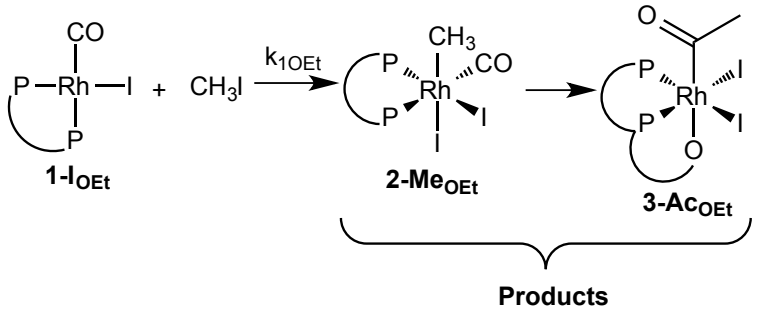

Table 3.5. Fitted parameters for oxidative addition of CH_3I to **1-I$_{OEt}$** at 0 °C in CH_2Cl_2, value from dppp complex provided for comparison.

Rate Constant	Value	S.D.
k_{1OEt}	1.34×10^{-6} mM^{-1} s^{-1}	7.4×10^{-9}
k_{1maj} (dppp, from Table 3.2)	1.28×10^{-6} mM^{-1} s^{-1}	7.0×10^{-10}

*3.4.4 Comparison of non-reductive methanol carbonylation catalyzed by **1-I** and **1-I$_{OEt}$***

Further comparison between dppp and dpppOEt ligands was done by reactions of **1-I** and **1-I$_{OEt}$** with CO at higher temperature pressure, 80 °C and 400 psig CO. These conditions are forceful enough to push the reaction toward formation of ester, i.e., the carbonylation reaction. Importantly, the rates of **3-Ac$_{(OEt)}$** formation, and even the rate of ester formation are comparable between complexes containing the dpppOEt and dppp ligands. This supports our hypothesis that the difference in activity between the two catalysts for MRC originates from the differences in hydrogenolysis rates, not the rates of oxidative addition of CH_3I or acetic acid formation.

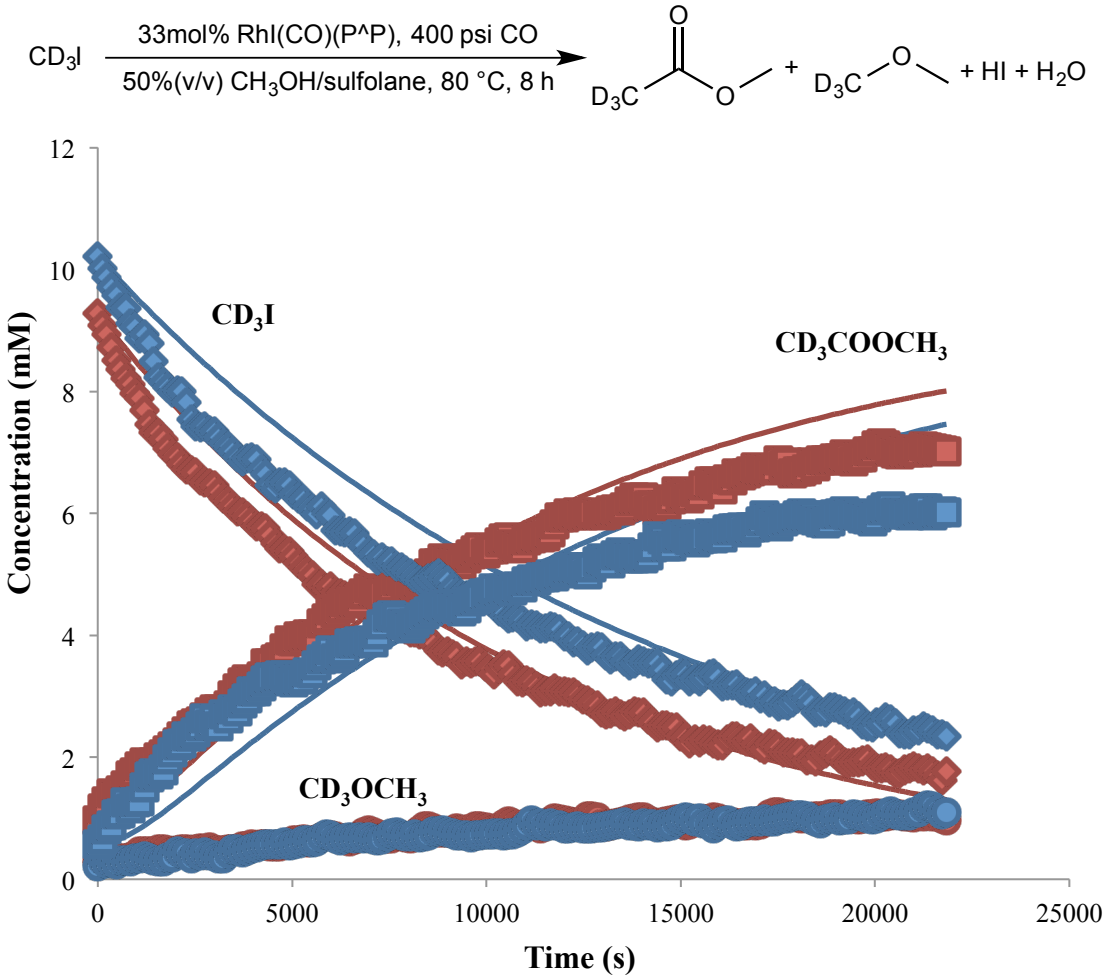

Figure 3.14. Comparison between Rh catalysts of dppp (red) and dpppOEt (blue) in carbonylation of CD_3I at 400 psig CO, 80 °, experimental data shown as solid symbols and fitted curves shown as solid lines.

Scheme 3.7. Kinetic model for carbonylation of CD_3I to methyl acetate.

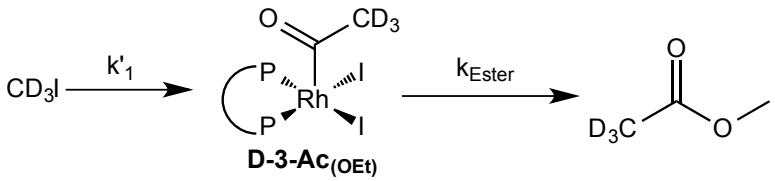

Table 3.6. Fitted parameters for carbonylation of CH_3I to methyl acetate catalyzed by Rh-dppp and Rh-dpppOEt catalysts at 80 °C, 400 psi CO in 50%(v/v) MeOH/sulfolane.

Rate Constant	Value	S.D.
k'_1	8.10×10^{-5} s^{-1}	1.2×10^{-7}
k_{Ester}	8.62×10^{-4} s^{-1}	1.1×10^{-5}
k'_{1OEt}	6.09×10^{-5} s^{-1}	1.2×10^{-7}
$k_{EsterOEt}$	1.01×10^{-3} s^{-1}	2.1×10^{-5}

3.5 Hydrogenolysis of 3-Ac and 3-Ac_{OEt}

Previous studies demonstrated that the hydrogenolysis of the Rh-acetyl complex, $[RhI_2(COCH_3)(P\hat{}P)]$, is the important acetaldehyde forming step in the catalytic cycle. We monitored this elementary step by ^2H NMR spectroscopy under conditions similar to those used for observation of the overall reaction. The complex **D-3-$Ac_{(OEt)}$** in 50%(v/v) methanol/sulfolane mixture was heated up to 80 °C, and then the reaction was pressurized with 500 psig 4:1 H_2/CO without gas circulation .

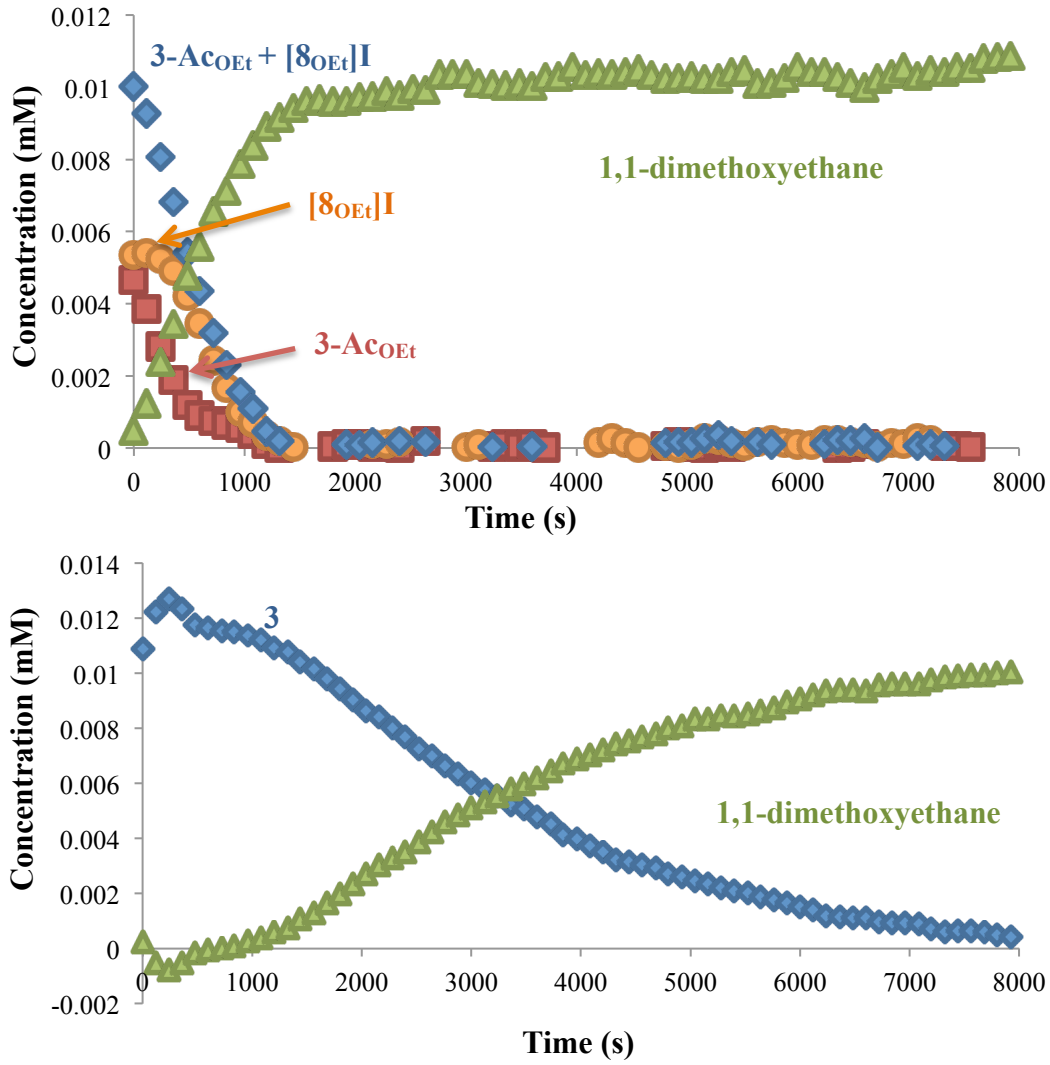

Figure 3.15. Hydrogenolysis of **D-3-Ac$_{OEt}$** (top) and **D-3-Ac** (bottom) at 500 psig 4:1 H_2/CO, 80 °C, monitored by ^{2}H NMR spectroscopy.

Without circulation, the reaction with **D-3-Ac** started with an apparent induction period believed to be caused by slow diffusion of syngas to the complex in the detection region of the spectrometer. Interestingly, there is an additional signal at 1.6 ppm in ^{2}H NMR spectrum observed when using complex **D-3-Ac$_{OEt}$**. This species is characterized later as [RhI(CD$_3$)(dpppOEt)]I, **[D-8$_{OEt}$]I** (see section 3.6 below). Both **D-3-Ac$_{OEt}$** and **[D-8$_{OEt}$]I** species exist in pseudo-equilibrium with one another and completely disappear at about the

point where the formation of 1,1-dimethoxyethane reached maximum (see Figure 3.15). This short induction period might come from coordination of CO to reform **D-3-Ac$_{OEt}$.** The ionized complex **D-3$_{OEt}$** readily reacts with H_2 once the gas dissolves into the solution, resulting in an unnoticeably short induction period. The half-lives of decay in the combined concentration of the two starting Rh-dpppOEt species are about 530 s, much shorter than that of Rh-dppp complex at 3000 s. This 5.7 fold increase in the reaction rate with the Rh-dpppOEt catalyst is in accordance with relative catalytic efficiencies observed by Dow, and it is obvious that the rate enhancement effected by the dpppOEt ligand occurs during the hydrogenolysis step.

3.6 Evidence of Ionized Species in Rh-dpppOEt Catalyzed MRC

During the hydrogenolysis of complex **D-3-Ac$_{OEt}$** as monitored by ^{2}H NMR spectroscopy, we observed a signal around 1.6 ppm at the beginning of the reaction. The signal, assigned to the ionized methyl iodo carbonyl complex **[D-8$_{OEt}$]I**, decays at a rate that is roughly similar to the rate at which the acetyl complex **D-3-Ac$_{OEt}$** decays. This behavior suggested that it is an important intermediate on the catalytic cycle or an off-cycle complex that is in equilibrium with **D-3-Ac$_{OEt}$**. Our initial observation found that the complex **[8$_{OEt}$]I** can form simply by dissolving **3-Ac$_{OEt}$** in methanol or methanol/sulfolane mixture without the need for high pressure or temperature. In addition to the signal at 1.6 ppm in the ^{2}H NMR spectrum, we observe signals at 17.9 ppm (br d, $J \approx 119$) and 40.5 ppm (br d, $J \approx 159$) in the ^{31}P NMR spectrum and at 1.7 ppm (br d, $^1J_{C\text{-}Rh} = 26$, Rh-$^{13}CH_3$) in the ^{13}C NMR spectrum for **[^{13}C-8$_{OEt}$]I** when the sample was prepared from **^{13}C-3-Ac$_{OEt}$**. The ^{13}C NMR signal correlates to a ^{1}H signal at 1.76 ppm (br d, $^1J_{H\text{-}C} = 138$) in a ^{13}C-^{1}H HSQC experiment. The NMR data assigned to **[8$_{OEt}$]I** as formed by simple dissolution of **3-Ac$_{OEt}$** in methanol or

methanol/sulfolane mixture are consistent with the signals observed during the reaction with H_2, as the chemical shifts of the same compound are generally similar in ^1H and ^2H NMR spectra. Based on the chemical shifts and strong Rh-C coupling constant of 26 Hz, **[8$_{OEt}$]I** appears to be more consistent with a Rh-methyl complex rather than Rh-acetyl complex, despite having Rh-acetyl **3-Ac$_{OEt}$** as a starting complex. It is interesting that we did not observe **[8$_{OEt}$]I** when **3-Ac$_{OEt}$** was dissolved in CH_2Cl_2.

Scheme 3.8. Formation of ionized species **[7$_{OEt}$]I**, **[8$_{OEt}$]I**, and **[7$_{OEt}$-CO]I**

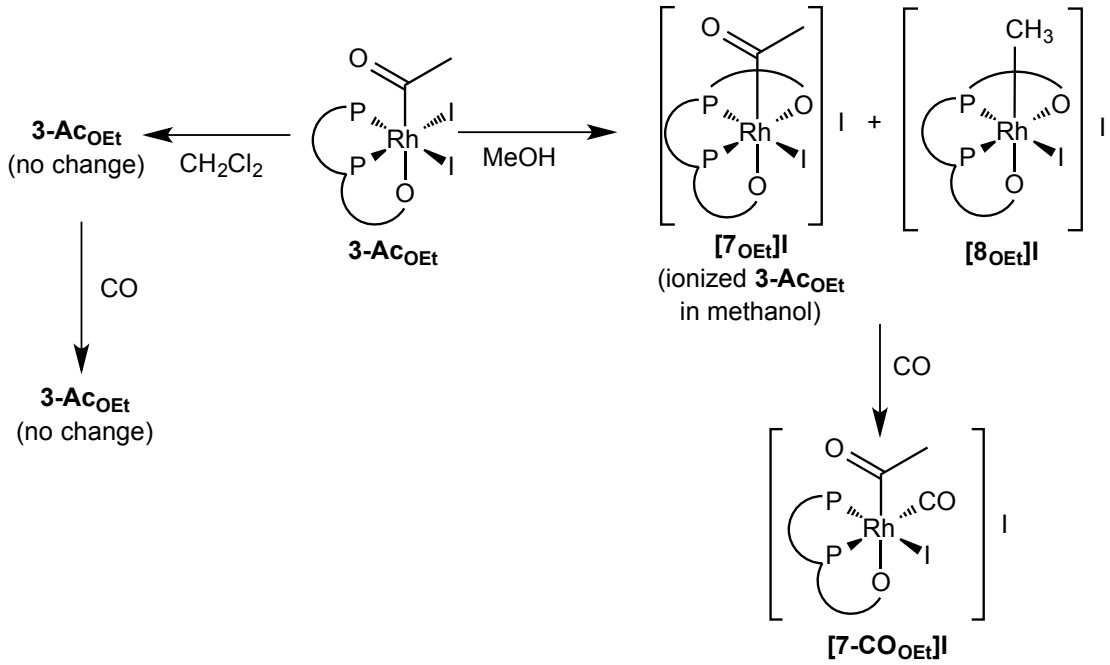

Since the NMR data suggested that **[8$_{OEt}$]I** is a methyl complex, it means that the complex **3-Ac$_{OEt}$** has to undergo decarbonylation. We tested this hypothesis by bubbling CO through the mixture of **D-3-Ac$_{OEt}$** and **[D-8$_{OEt}$]I** in methanol/sulfolane. Unexpectedly, the signals of both complexes disappeared immediately (see Scheme 3.8). ^{31}P NMR spectrum shows a very broad signal of the product at 5.0 ppm (br s) at 24 °C, assigned as **[D-7-CO$_{OEt}$]**I. At -30 °C the signal decoalesces to 3 pairs of doublet of doublets at 16.5 ppm (dd, $J_{P\text{-}Rh,\ P\text{-}P}$ = 114, 36), 4.8 (dd, $J_{P\text{-}Rh,\ P\text{-}P}$ = 124, 37); 13.6 (dd, $J_{P\text{-}Rh,\ P\text{-}P}$ = 116, 26), 5.6 (dd, $J_{P\text{-}Rh,}$

$_{P\text{-}P}$ = 123, 26); 8.1 (br dd, $J_{P\text{-}Rh,\ P\text{-}P}$ = 111, 28), ~6.3 (br dd, too broad to obtained *J* and overlap with peak at 5.6). The signal at 1.6 ppm in ^{2}H NMR spectrum **[D-8$_{OEt}$]I** also disappeared immediately upon CO bubbling, while a new acetyl signal at 3.0 ppm is observed in the ^{2}H NMR spectrum. When a ^{13}C-enriched mixture of **^{13}C-3-Ac$_{OEt}$** and **[^{13}C-8$_{OEt}$]I** was bubbled with CO, we similarly observed that the ^{13}C NMR signal at 1.7 ppm disappeared. An apparent new acetyl signal in the ^{13}C NMR spectrum overlaps with CD_3OD solvent peak and is not clearly seen. This reactivity of CO with both **3-Ac$_{OEt}$** and **[8$_{OEt}$]I** was also not observed when the reaction was conducted in CH_2Cl_2 or for the dppp system. In fact, no complex like **[8]I** forms with the dppp complex **3-Ac** even in methanol/sulfolane. We hypothesized that complex **[8$_{OEt}$]I** is an ionized Rh-methyl species, [RhI(CH_3)(CO)$_x$(dpppOEt)]I where x = 0 or 1, from its selective formation in polar solvent. The CO-saturated complex **[7-CO$_{OEt}$]I** is proposed to be the ionized Rh-acetyl species, [RhI($COCH_3$)(CO)(dpppOEt)]I, formed from **[7$_{OEt}$]I** (ionized form of **3-Ac$_{OEt}$**), based on the difference in reactivity of **3-Ac$_{OEt}$** with CO in methanol and CH_2Cl_2. The three species observed from the sample of **[7-CO$_{OEt}$]I** at low temperature (Figure 3.16) are believed to be interchangeable isomers arising from coordination of different, inequivalent ethoxy groups.

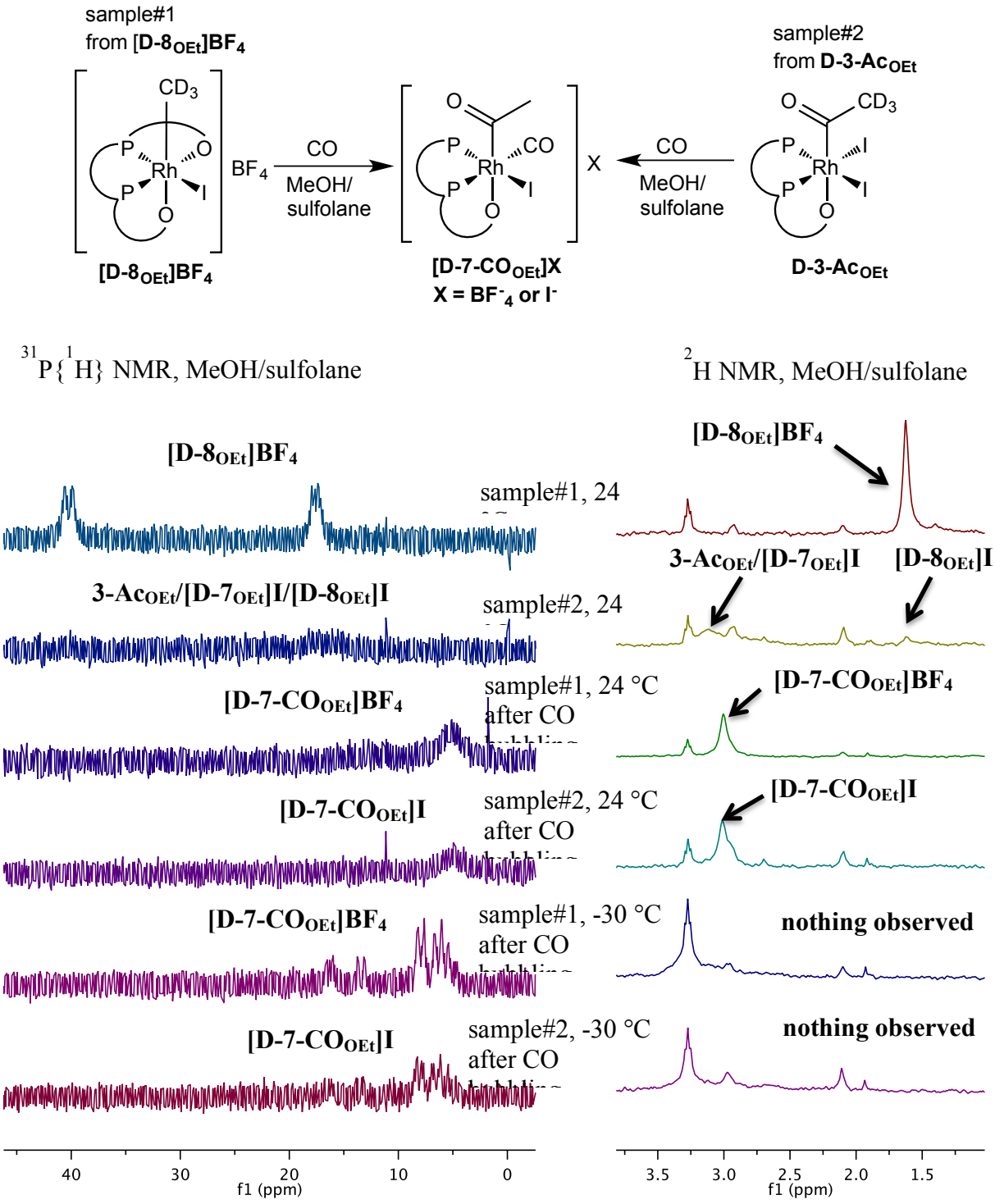

Figure 3.16. ^{31}P and ^{2}H NMR spectra of formation of **[D-7-CO$_{OEt}$]X** where X = BF^-_4 or I^- from different starting materials, **[D-8$_{OEt}$]BF$_4$** and **D-3$_{OEt}$**.

We further investigated the nature of the complex **[7-CO$_{OEt}$]I** by synthesizing the complex, [RhI(CH$_3$)(dpppOEt)]BF$_4$, **[8$_{OEt}$]BF$_4$**. Reaction of [Rh(nbd)$_2$]BF$_4$ (nbd = norbornadiene) with 1 equiv of dpppOEt followed by hydrogenation of the nbd ligand in CD$_3$OD results in [Rh(dpppOEt)(solv)$_2$]BF$_4$. Reaction of this cationic rhodium complex with CH$_3$I yields the target complex. The CO-free precursor was used intentionally to clarify if there is CO coordination on **[8$_{OEt}$]BF$_4$**. The characterization of **[8$_{OEt}$]BF$_4$** by ^{31}P, ^{13}C and ^{2}H NMR spectroscopy (with isotopically labeled material) as well as its reactivity with CO allow us to conclude that **[8$_{OEt}$]BF$_4$** and **[8$_{OEt}$]I** are ionic species sharing the same cation, [RhI(CH$_3$)(dpppOEt)]$^+$ with different counterions, BF^-_4 in **[8$_{OEt}$]BF$_4$** and I^- in **[8$_{OEt}$]I**. X-ray crystallography ultimately confirmed the identity of **[8$_{OEt}$]BF$_4$** as a cationic complex with the dpppOEt ligand coordinating in a tetradentate fashion where one of ethoxy group *ortho* to each phosphorus atom participates in coordination (Figure 3.17). The fact that the cationic species with non-coordinating BF^-_4 produces the similar products, spectroscopically, in the reaction with CO is a strong evidence that the products **[7-CO$_{OEt}$]I/[7-CO$_{OEt}$]BF$_4$** share the same cationic species with only one coordinating iodide ligand, [RhI(COCH$_3$)(CO)(dpppOEt)]$^+$ in accordance to our proposal (see Figure 3.16).

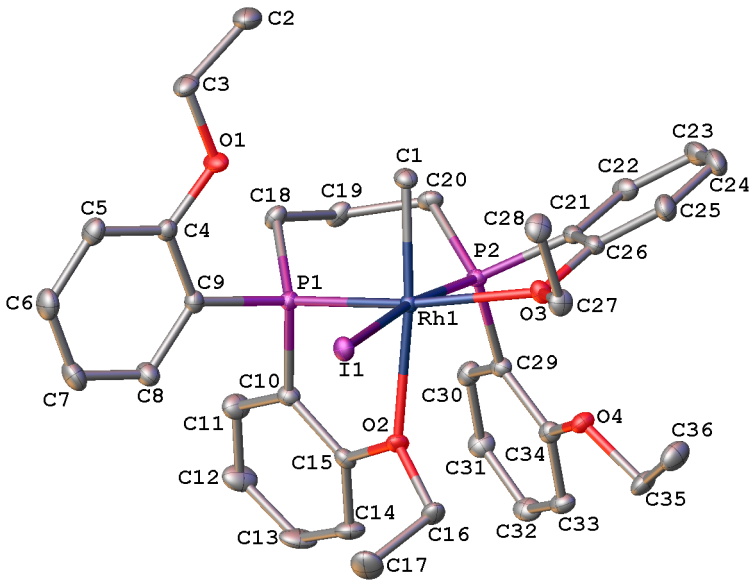

Figure 3.17. Crystallographic structure of $[\mathbf{8_{OEt}}]^+$ in $\mathbf{[8_{OEt}]BF_4}$ shown with 50% probability ellipsoids. All H atoms, anion, and minor component of the compositional disorder are omitted.

The absence of analogous **[8]I** and **[7-CO]I** for complexes containing the dppp ligand suggested that *ortho*-ethoxy groups of dpppOEt act as auxiliary coordination sites to promote ionization and stabilize the ionized complex in polar solvent. From the behavior of $\mathbf{[8_{OEt}]I}$, the cationic complex holds CO quite loosely and is subject to decarbonyalation when CO pressure is not high enough, probably because of ligand exchange by the chelating *ortho*-ethoxy group and the lower electron donating nature of a cationic complex compared to a neutral complex. However, the ether group is not expected to bind strongly to the Rh center. We believe that the cationic species, $\mathbf{[8_{OEt}]}$ and $\mathbf{[7\text{-}CO_{OEt}]}$, can easily access to the structure with an open coordination site by losing either CO or the ethoxy ligand, and allow H_2 to coordinate and react more rapidly. The hypothesis agrees with rate enhancement of hydrogenolysis of Rh-acetyl diiodo complex in dpppOEt, $\mathbf{3\text{-}Ac_{OEt}}$ compared to **3-Ac**. By the

same argument, the Rh-dppp complex, without the ether group, will stay mostly in neutral form with a small portion being ionized; thus the catalyst is slower and subject to inhibition by the iodide ion, as we observed in the overall reaction rate measurement.

3.7 Conclusions - Ionization mechanism

We conclude our studies with a new mechanistic proposal, the ionization mechanism, based on the mechanism originally proposed by Wegman and Moloy. This mechanism starts with the Rh iodo monocarbonyl complex **1-I**, which undergoes oxidative addition with CH_3I similar to the Wegman-Moloy mechanism. Complex **1-I** is found in preferential equilibrium toward inert Rh iodo dicarbonyl complex, **4-I**, under CO atmosphere, substantially decreasing the rate of oxidative addition. In spite of being inhibited by CO, this step appears to be fast and is not rate controlling at higher temperature for the dppp complex. The results also agree with zero order kinetics with respect to CH_3I in the overall rate seen in the original report of Wegman and Moloy and a recent report from Dow. In contrast, the MRC appears first order with respect to CH_3I and inversely dependent on CO with Rh-dpppOEt catalyst, despite having a comparable rate of oxidative addition. This result is explained by enhancement in the rate of hydrogenolysis by the Rh-dpppOEt catalyst, making the oxidative addition step a significant contributer in the overall rate calculation.

Scheme 3.9. Proposed ionization mechanism. The 'OEt' subscription in the case of dpppOEt ligand is omitted for clarity.

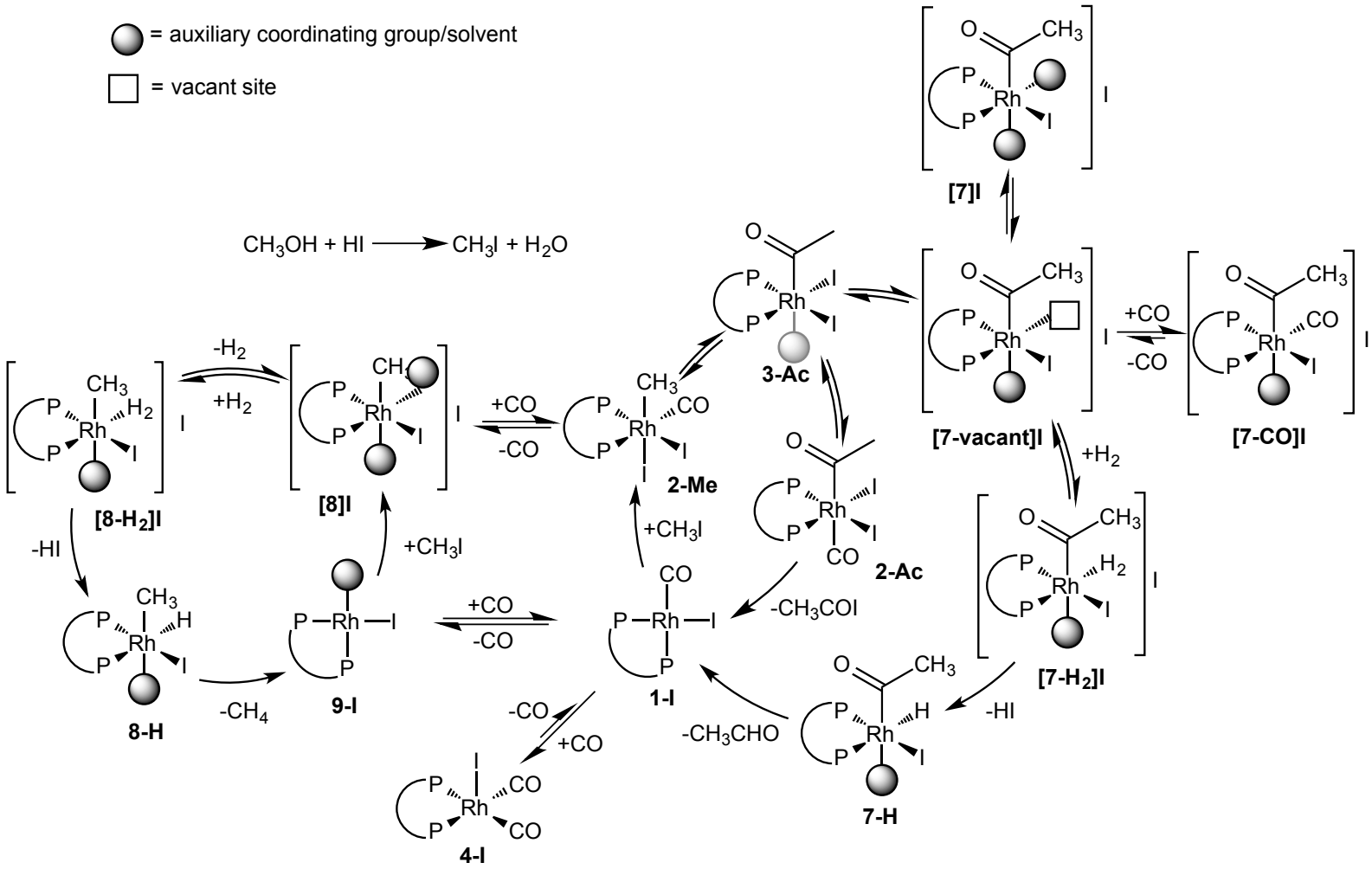

The important modification made to the original Wegman and Moloy proposal is the ionization of the diiodo Rh-acetyl complex **3-Ac**. The proposed ionization agrees with many observations, including the observed inhibition by the presence of iodide ion, both by intentional addition and by formation of HI during the reaction, and selectivity loss when less polar solvent is used. Moreover, cationic metal complexes are known to coordinate with the σ-donating molecular H_2 better than neutral complex due to an increased electrophilicity.[9–12] This ionization step causes a major deviation in the mechanism and rate laws between the dpppOEt and dppp complexes, as the former possesses ether groups believed to assist ionization. Study of the reaction rate at this particular step reveals that the dpppOEt Rh-acetyl complex, **3-Ac$_{OEt}$**, produces the hydrogenolysis product 1,1-dimethoxyethane under synthesis gas much faster than the corresponding dppp complex, **3-Ac**. Observation of the ionized complex **[8$_{OEt}$]I** during the reaction, combined with other characterization data, strongly suggests the presence of ionized species during catalysis with the Rh-dpppOEt complex. For the Rh-dpppOEt catalyst, the approximately first-order rate dependence on H_2 partial pressure is not unexpected from the mechanism. The additional inverse rate dependence on CO pressure, also, might arise from this step as evidence shows that CO can occupy the vacant coordination site of the ionized species and dissociation of CO need to occur before H_2 can react. On the other hand, the rate of MRC catalyzed by the Rh-dppp complex is zero order in H_2 and CO, as observed by Dow, is surprising and differs from our observation.[13] Kinetic studies at catalytic conditions are needed before a definite conclusion can be made. However, a plausible explanation based on our mechanism, if all the observations are accurate, is that the ionization step itself is the slow step for the Rh-dppp catalyst. Therefore, the reaction of the ionized species with H_2 is much faster and the rate

depends only on the Rh complex under catalytic conditions. In our kinetic measurements, the temperature and H_2 pressure are substantially lower than common catalytic conditions and the reaction of the ionized species with H_2 is slow enough that H_2 is not kinetically invisible.

The later steps in the proposed catalytic cycle are heterolytic cleavage of coordinated H_2 and elimination of HI, followed by reductive elimination of acetaldehyde to regenerate **1-I**. The proposal is based on computational studies that disfavor sigma bond metathesis, and milder reaction conditions required in the presence of base observed by Moloy and Petersen.[8,14]

The formation of methyl acetate is believed to be similar to the original proposal, since we did not observe significant different results between the two catalysts in the carbonylation reaction. On the other hand, methane formation is proposed to be related to the ionization pathway, since decarbonylation is facile under conditions that favor formation of the ionized intermediates. We also observed that when the reaction is CO-starved, CH_3I continues to be consumed, with a loss of selectivity due to methane formation.

In summary, we have demonstrated that the new equipment, WiHP-NMRR, is effectively capable of monitoring reactions at unusual, high temperature and pressure, conditions. This capability was used to investigate Rh(diphosphine) catalyzed MRC and allowed us obtain unique and useful data. Although further studies are necessary to completely reveal the full, definitive mechanism, we have proposed a new mechanism with ionization of the catalytic species key to the hydrogenolysis step. The ionization mechanism proposed agrees with the data we have obtained up to the current stage, and explains the origin of differences between the dppp and the superior dpppOEt complexes, which could inform future ligand design for the MRC.

3.8 Experimental

General Considerations

All manipulations were carried out under N_2 using standard Schlenk, high vacuum, and glovebox techniques. Dichloromethane, diethyl ether, $^{13}CH_3I$, dppp were obtained from Sigma-Aldrich. CD_2Cl_2 was obtained from Cambridge Isotope Laboratories. All solvents and liquid reagents were degassed by at least three freeze-pump-thaw cycles or sparging with N_2 and dried by passing through activated alumna unless otherwise noted. All MeOH/sulfolane solvent was mixed to 50%(v/v) mixture before it was degassed an dried to reduce melting point for handling. $^{13}CH_3I$ was used as received. $RhCl_3 \cdot xH_2O$ from Alfa Aesar and $Rh(acac)(CO)_2$ from Dow were used as received. Most of the Rh complexes were synthesized in NMR tube for characterization purpose and were not isolated. The isotopically unlabeled complexes were prepared similarly to the corresponding labeled complexes and the complexes of dpppOEt ligand were prepared similarly to the analogous complexes of dppp ligand. The complex $[RhCl(CO)_2]_2$ was prepared according to the reported procedure.[15,16].

Routine NMR experiments were performed on Bruker AC+ 300a, Avance-400 spectrometers. All reaction monitoring, variable temperature, and two-dimensional correlation experiments were performed on Varian Unity 500 and Inova 600; Bruker Avance-360 and Avance-500 spectrometers. ^1H NMR spectra were referenced with a solvent peak. ^{31}P and ^{13}C NMR spectra were referenced with ^1H NMR spectrum by absolute referencing. All the coupling constants are reported in hertz.

Kinetic studies of Rh-dppp catalyzed MRC, representative procedure: The sample for WiHP-NMRR was prepared into three separate airtight syringes with valve control and blunt tip needles in the glovebox: #1 solution of **1** (5.3 mM in MeOH/sulfolane, 1.75 mL, 9.3 x 10^{-3} mmol) with 0.050 mL $(CDCl_2)_2$ internal standard, #2 solution of CD_3I

(0.023 mL, 0.37 mmol) in 0.1 mL MeOH/sulfolane, #3 MeOH/sulfolane (0.50 mL) as solvent chaser. The WiHP-NMR apparatus had been pressurized and vented with H_2 gas at 50 psig at least three times before sample in syringe #1 was injected through manual injection port. The apparatus was pressurized and vented another three times to remove air that might enter the system during the injection. Then the system was pressurized with H_2 to 100 psi. The valve between reservoir bottle had been closed and the bottle had been pressurized and vented with 1:1 synthesis gas before the valve was opened to pressurize the system to the total pressure of 300 psi (of 2:1 H_2/CO gas). The valve had been closed again, and the reservoir bottle was pressurized to 700 psi 1:1 synthesis gas. The source gas cylinder was then closed. The system was filled with N_2 up to total pressure of 600 psi. The apparatus was circulated for a few minutes to push down any sample retained in the tubing. ^{1}H and ^{2}H NMR spectra was taken for reference at 25 °C and at reaction temperature, 90 °C. The pulse sequence for ^{2}H NMR spectra has d1 and d2, circulation and bubble dissipation delays, of 3.5 s and 0.5 s, respectively and acquisition of 2 s. The delays were repeated one more time before acquisition so the circulation at 70 % duty cycle occurred in intervals to reduce loss of volatile materials. Once the reaction had reached target temperature for 10 min, CH_3I was injected to the spectrometer by loading syringe #3 and #2 into the sample loop (the order matters as the last sample loaded is injected first) followed by pushing with N_2 at about 650 psi until the system pressure increased by 10 psi. The series of data collection, by multizg automation, started immediately right after. With the regulator set to 600 psi, the valve from gas reservoir bottle was now opened to continuously supply the system with synthesis gas. When the experiment was over, the system was cooled down to room temperature, depressurized and washed with methanol, acetone, and CH_2Cl_2 before placing the system

under vacuum for at least 1 h before the next use.

Kinetic studies of oxidative addition of CH_3I to RhI(CO)(P^P) under ambient pressure, representative procedure: Solution of **1** (0.0150 g, 0.0224 mmol) in CH_2Cl_2 (0.610 mL) in septum-capped NMR tube in ice/water bath was injected with CH_3I (1.00 M in CH_2Cl_2, 0.0900 mL, 0.0900 mmol) through syringe needle. The sample was injected into the spectrometer at set temperature of 0 °C, and the data collection occurred immediately by pseudo two-dimensional kinetic experiment method.

Kinetic studies of oxidative addition of CD_3I to RhI(CO)(P^P), 1 and 1_{OEt} and carbonylcation of CD_3I, under high pressure of CO, representative procedure: The sample for WiHP-NMRR was prepared into three separate airtight syringes with valve control and blunt tip needles in the glovebox: #1 solution of 1 (0.0285 g, 0.0336 mmol) in 0.8 mL CH_2Cl_2, #2 CH_2Cl_2 0.3 mL for rinsing, #3 CD_3I (1.0 M in CD_2Cl_2, 0.134 mL, 0.134 mmol, CD_2Cl_2 also used as internal standard) in 0.266 mL CH_2Cl_2. The residual air was purged with CO from the apparatus before and after sample injection by pressurizing and venting mentioned above. The sample in syringe #1 and #2 were injected through manual injection port. Then it was bubbled with CO for 10 min and left under 100 psi CO until complete conversion to 1CO as examined by ^{31}P NMR spectroscopy. The system was depressurized to atmospheric pressure of CO and the substrate in syringe #3 was injected manually. The reaction was heated up to 60 °C and equilibrated in 20 min. The data collection began right after substrate injection by ^{2}H NMR pseudo two-dimensional kinetic experiment method, but the data before 2000 s was not used in calculation due to unsettled temperature.

Kinetic studies of hydrogenolysis of $RhI_2(COCD_3)$(P^P), D-3 and $D\text{-}3_{OEt}$, under high pressure of synthesis gas, representative procedure: The sample for WiHP-NMRR was

prepared into two separate airtight syringes with valve control and blunt tip needles in the glovebox: #1 solution of D-3 (0.0151 g, 0.0185 mmol) in 0.75 mL sulfolane, #2 MeOH 0.75 mL for rinsing with 0.050 mL benzene-d_6 internal standard. The residual air was purged with N_2 from the apparatus before and after sample injection by pressurizing and venting mentioned above. The samples in syringe #1 and #2 were injected to the system followed by heating the sample to 80 °C. The data collection by ^{2}H NMR pseudo two-dimensional kinetic experiment method started when 500 psi 4:1 H_2/CO was introduced to the system.

[RhI(CO)(dpppOEt)]BF_4, $\mathbf{14_{OEt}BF_4}$: Solution of [Rh(nbd)$_2$]BF_4 (0.0346 g, 0.0925 mmol) with dpppOEt (0.0545 g, 0.0925 mmol, 1 equiv) in CH_2Cl_2 was bubbled with H_2 to hydrogenated norbonadiene for 50 min at room temperature and briefly bubbled with N_2 to purge H_2. The sample was added with CD_3I (2.0 M in CD_2Cl_2, 0.056 mL, 0.112 mmol, 1.2 equiv) to form the product. Dimethyl ether was added slowly to the sample and the precipitated product was filter and dried under vacuum.

3.9 References

(1) Moloy, K. G.; Wegman, R. W. *Organometallics* **1989**, *8*, 2883–2892.

(2) Sheldon, R. A. In *Chemicals from Synthesis Gas - Catalytic Reactions of CO and H2*; Catalysis by Metal Complexes; Springer Netherlands: Dordrecht, Holland, 1983; pp. 149–153.

(3) Torres, A.; Molina Perez, N.; Overend, G.; Hodge, N.; Heaton, B. T.; Iggo, J. A.; Satherley, J.; Whyman, R.; Eastham, G. R.; Gobby, D. *ACS Catal.* **2012**, *2*, 2281–2289.

(4) Overend, G.; Iggo, J. A.; Heaton, B. T.; Whyman, R. *Magn. Reson. Chem.* **2008**, *46*, S100–S106.

(5) Christopher Roe, D. *J. Magn. Reson.* **1985**, *63*, 388–391.

(6) Elsevier, C. J. *J. Mol. Catal.* **1994**, *92*, 285–297.

(7) Horvath, I. T.; Millar, J. M. *Chem. Rev.* **1991**, *91*, 1339–1351.

(8) Margl, P.; Klamo, S. B.; Patyk, R. A. Personal Communication.

(9) Kubas, G. J. *Chem. Rev.* **2007**, *107*, 4152–4205.

(10) Heinekey, D. M.; Oldham, W. J. *Chem. Rev.* **1993**, *93*, 913–926.

(11) McGrady, G. S.; Guilera, G. *Chem. Soc. Rev.* **2003**, *32*, 383.

(12) Findlater, M.; Schultz, K. M.; Bernskoetter, W. H.; Cartwright-Sykes, A.; Heinekey, D. M.; Brookhart, M. *Inorg. Chem.* **2012**, *51*, 4672–4678.

(13) Clark, T. P.; Spinney, H.; Macdonald, J.; Cummins, C.; Klosin, J.; Briggs, J. unpublished results.

(14) Moloy, K. G.; Petersen, J. L. *Organometallics* **1995**, *14*, 2931–2936.

(15) Hanh Nguyen, D.; Lassauque, N.; Vendier, L.; Mallet-Ladeira, S.; Le Berre, C.; Serp, P.; Kalck, P. *Eur. J. Inorg. Chem.* **2014**, *2014*, 326–336.

(16) Montag, M.; Schwartsburd, L.; Cohen, R.; Leitus, G.; Ben-David, Y.; Martin, J. M. L.; Milstein, D. *Angew. Chemie Int. Ed.* **2007**, *46*, 1901–1904.

Appendix:

Supporting Information

A.1. NMR Spectra

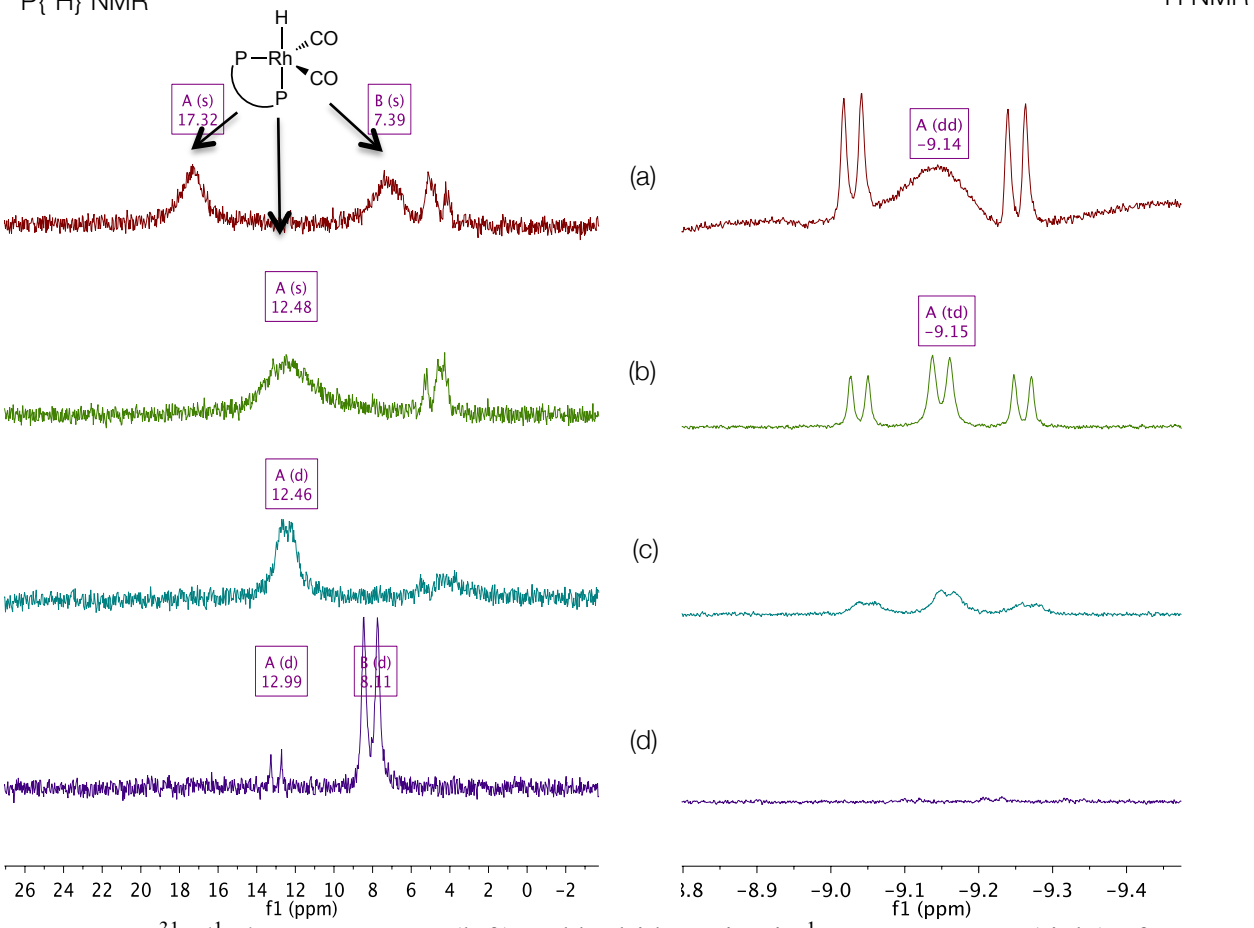

Figure A1. $^{31}P\{^{1}H\}$ NMR spectra (left) and hydride region in ^{1}H NMR spectra (right) of **4-H** at (a) -80 °C, (b) -50 °C, (c) -30 °C, and (d) 24 °C (mostly converted to **6**) in CD_2Cl_2 under atmospheric pressure of synthesis gas.

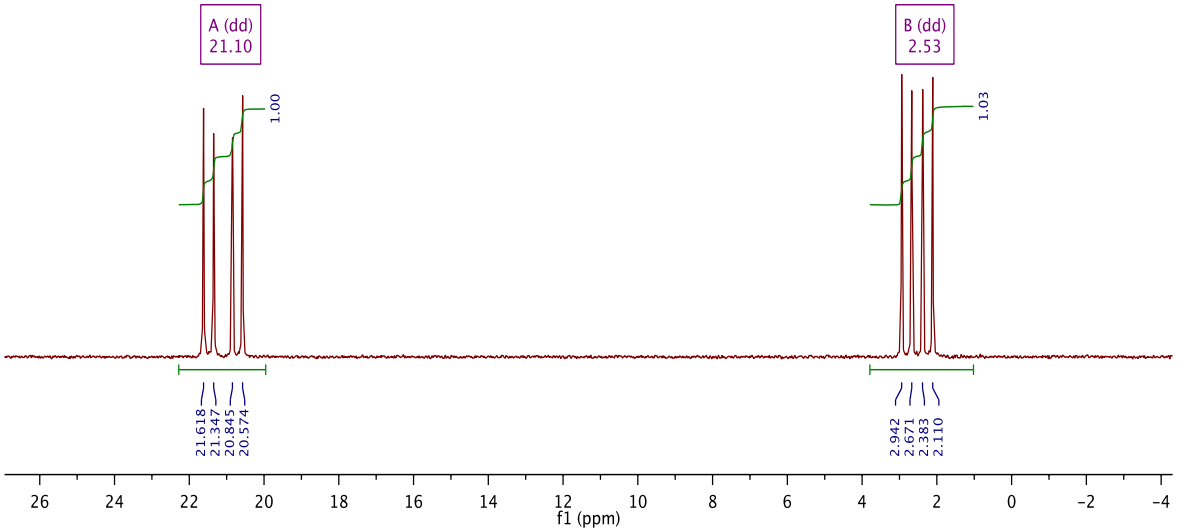

Figure A2. $^{31}P\{^{1}H\}$ NMR spectrum of **1-I** (202.5 MHz, CH_2Cl_2, -80 °C).

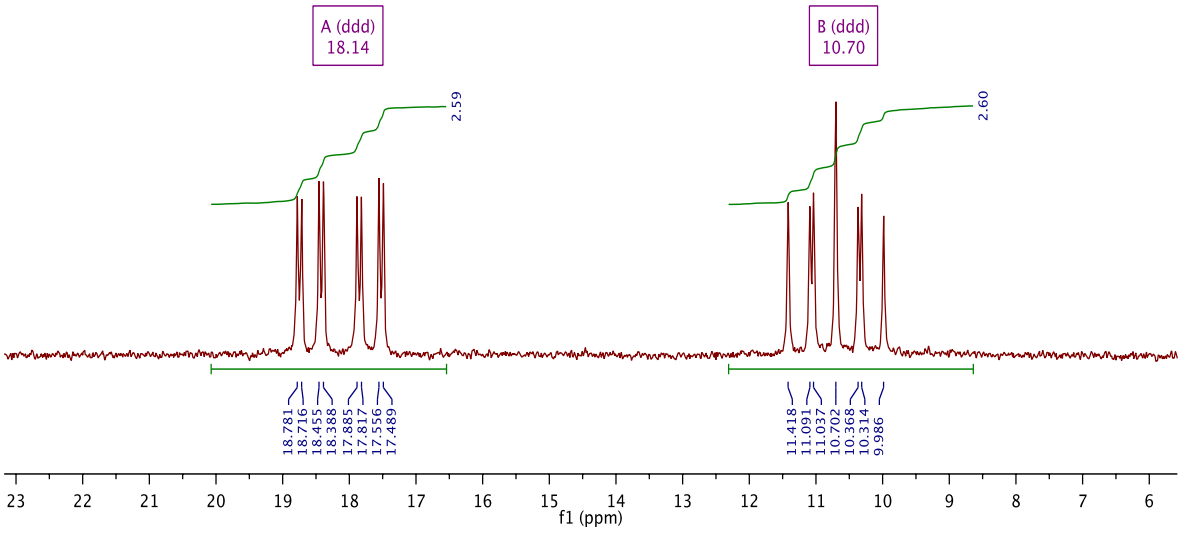

Figure A3. $^{31}P\{^{1}H\}$ NMR spectrum of **^{13}C-1-Me** (145.8 MHz, CH_2Cl_2, -80 °C).

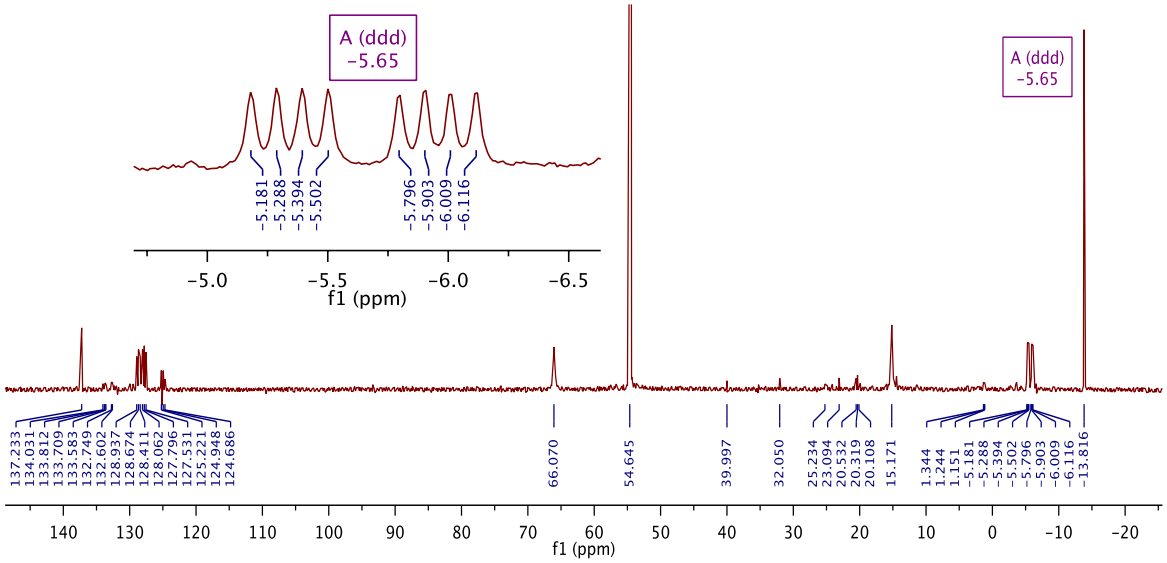

Figure A4. $^{13}C\{^{1}H\}$ NMR spectrum of **^{13}C-1-Me** (90.56 MHz, CH_2Cl_2, -80 °C).

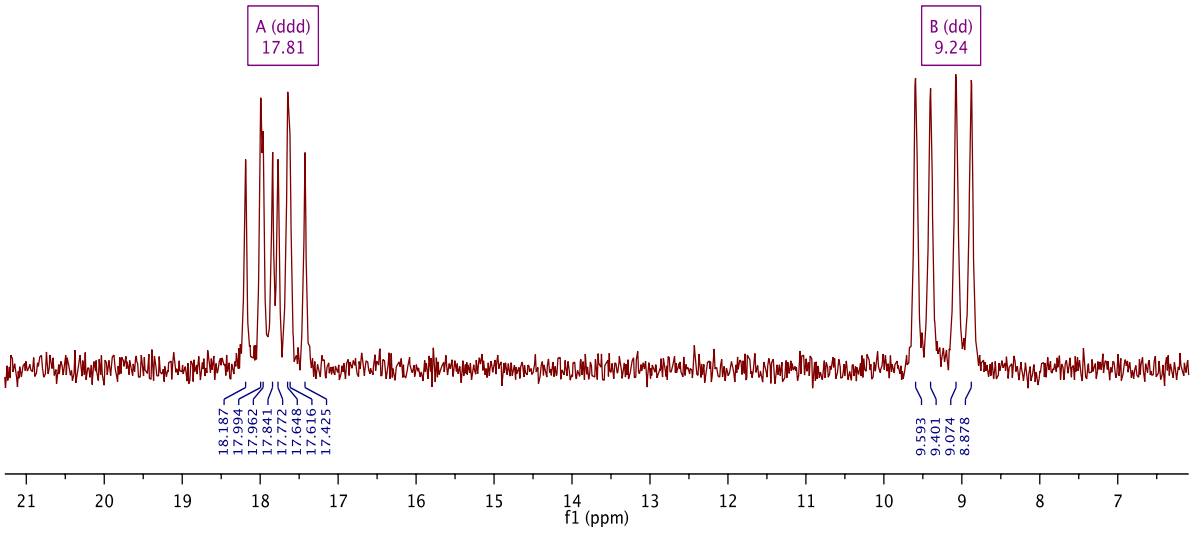

Figure A5. $^{31}P\{^{1}H\}$ NMR spectrum of **^{13}C-4-Me** (242.8 MHz, CH_2Cl_2, -75 °C).

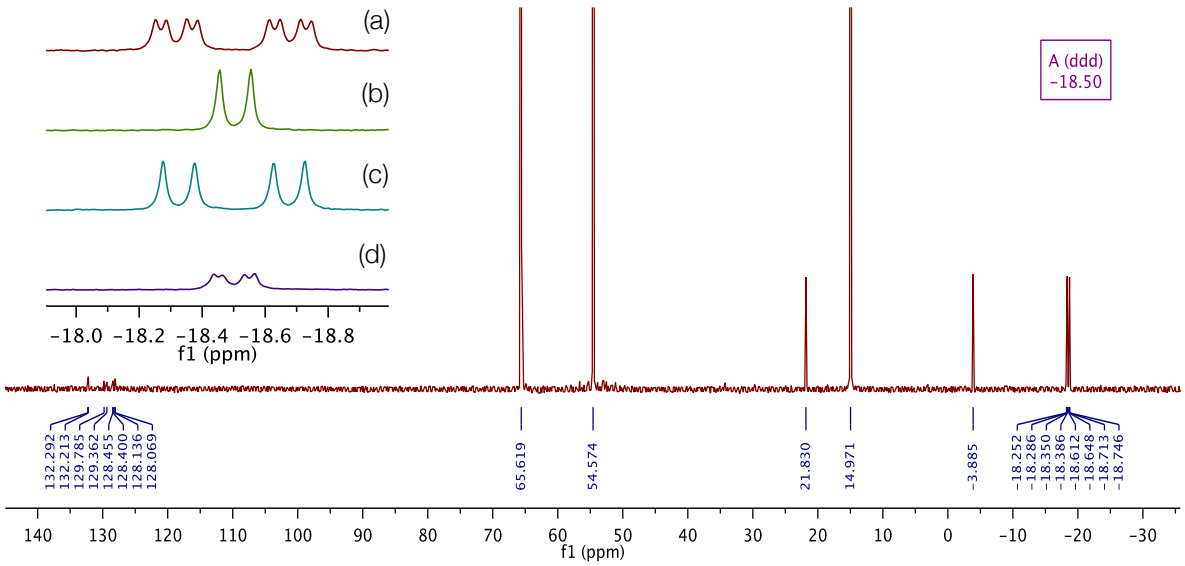

Figure A6. $^{13}C\{^{1}H\}$ NMR spectrum of **^{13}C-4-Me** (150.8 MHz, CH_2Cl_2, -75 °C). Inset shows Rh-$^{13}CH_3$ signal with (a) all ^{31}P coupled, (b) all ^{31}P decoupled, (c) upfield ^{31}P decoupled, (d) downfield ^{31}P decoupled.

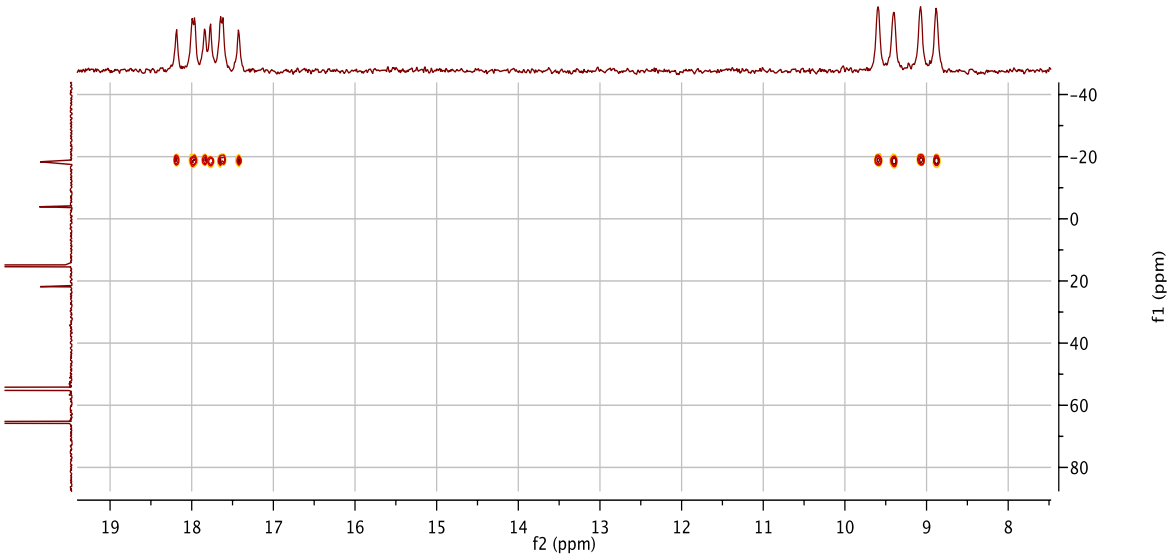

Figure A7. $^{31}P\{^{1}H\}$-$^{13}C\{^{1}H\}$ HMBC of **^{13}C-4-Me** (242.8,150.8 MHz, CH_2Cl_2, -75 °C, jnxh = 5 Hz).

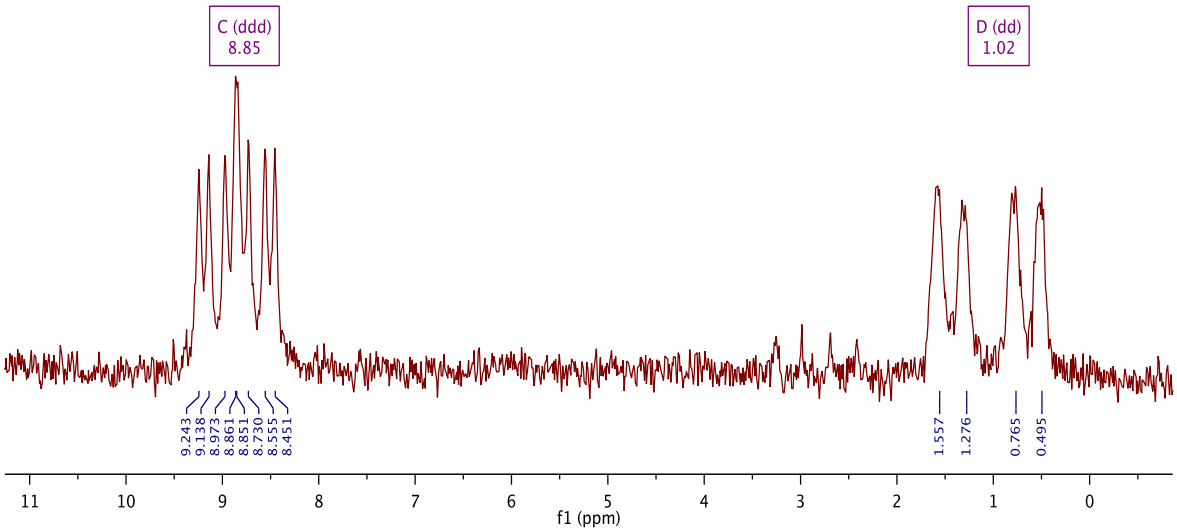

Figure A8. $^{31}P\{^{1}H\}$ NMR spectrum of **^{13}C-1-Ac** (202.5 MHz, CD_2Cl_2, -30 °C).

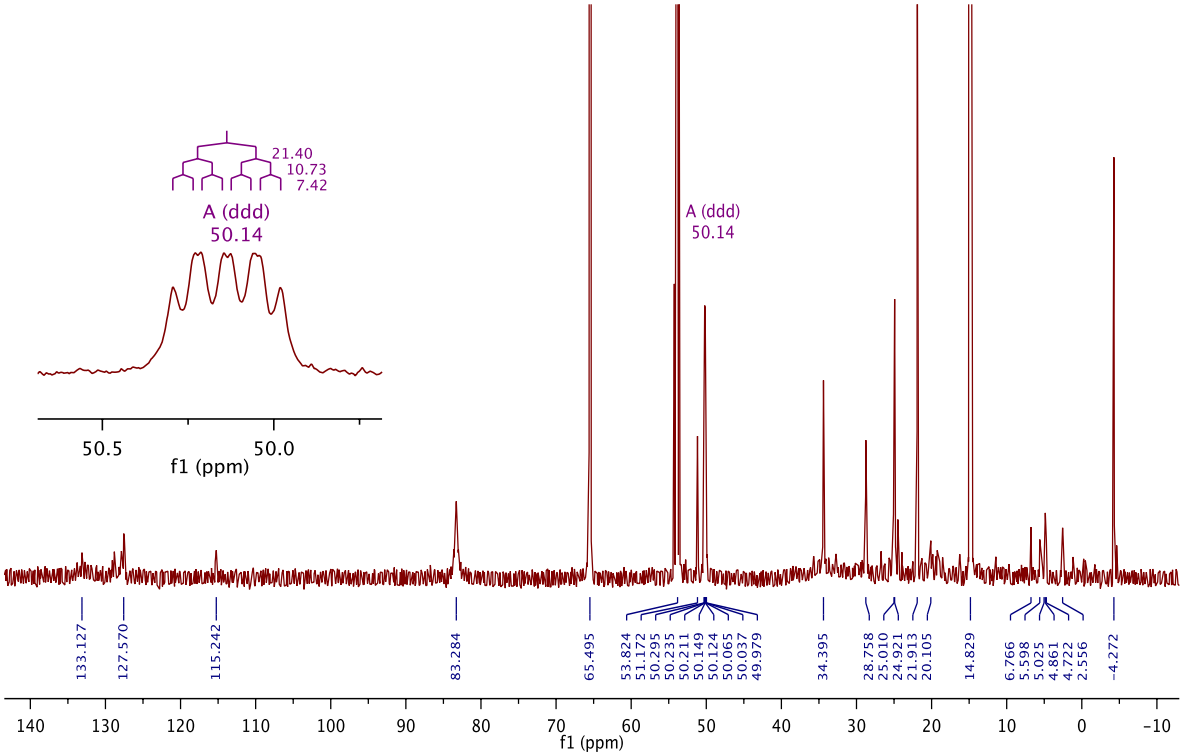

Figure A9. $^{13}C\{^{1}H\}$ NMR spectrum of **^{13}C-1-Ac** (125.8 MHz, CD_2Cl_2, -75 °C). Inset shows Rh-CO^{13}*C*H$_3$ signal.

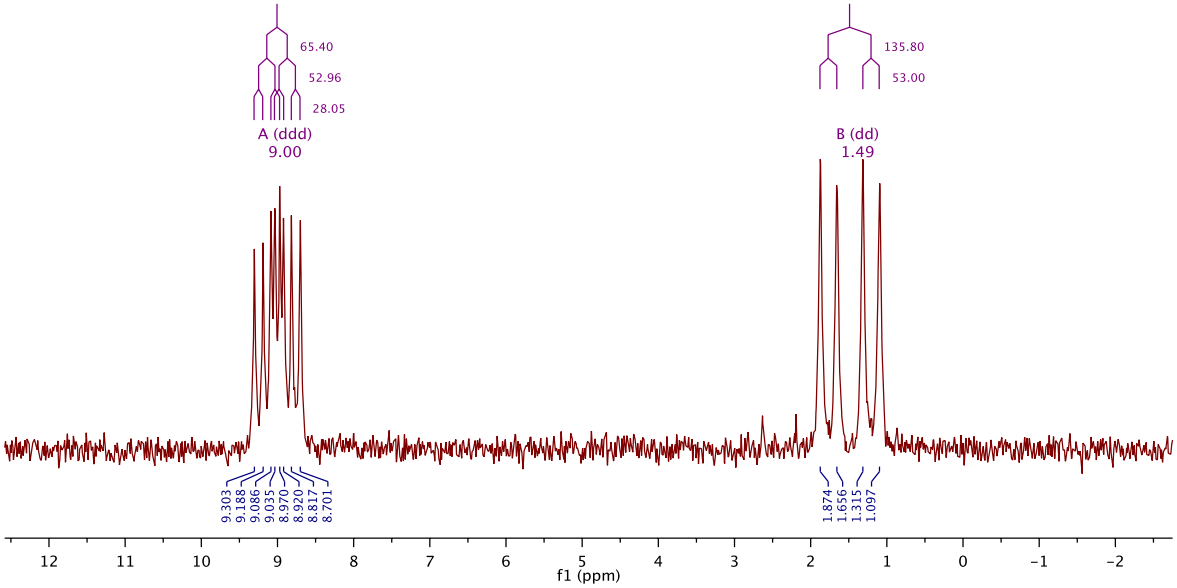

Figure A10. $^{31}P\{^{1}H\}$ NMR spectrum of **^{13}C-4-Ac** (242.8 MHz, CH_2Cl_2, -30 °C).

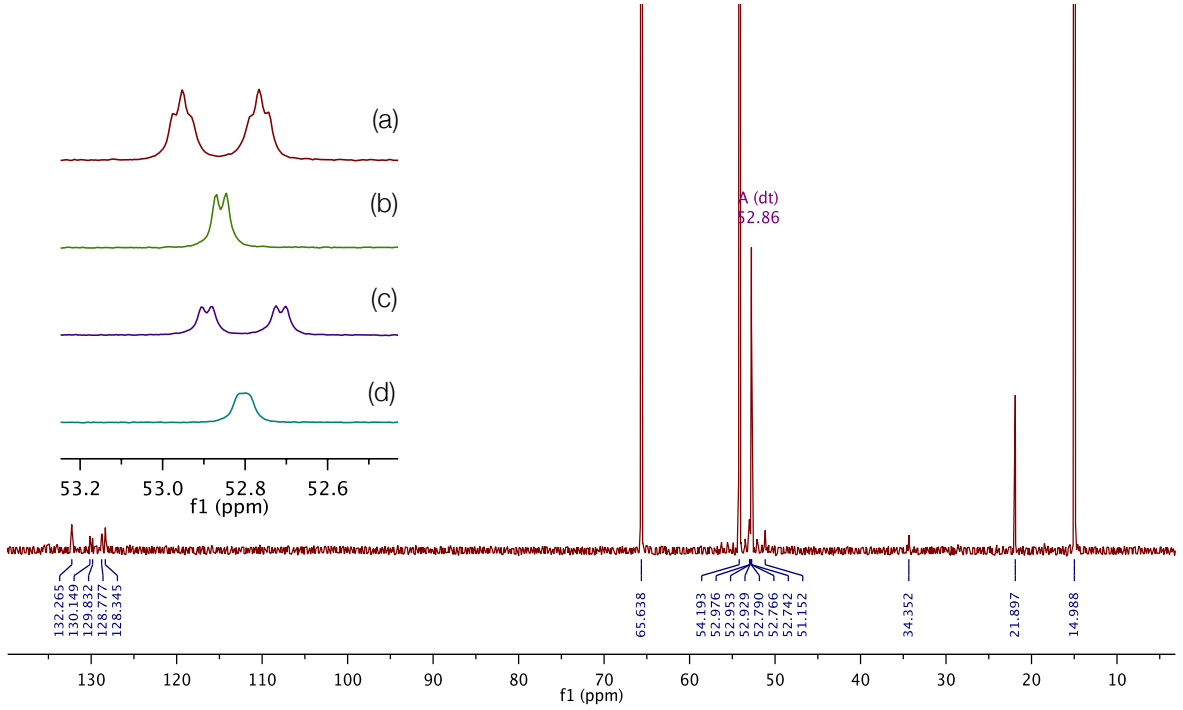

Figure A11. $^{13}C\{^{1}H\}$ NMR spectrum of **^{13}C-4-Ac** (150.8 MHz, CH_2Cl_2, -30 °C). Inset shows Rh-CO^{13}*C*H_3 signal with (a) all ^{31}P coupled, (b) all ^{31}P decoupled, (c) upfield ^{31}P decoupled, (d) downfield ^{31}P decoupled.

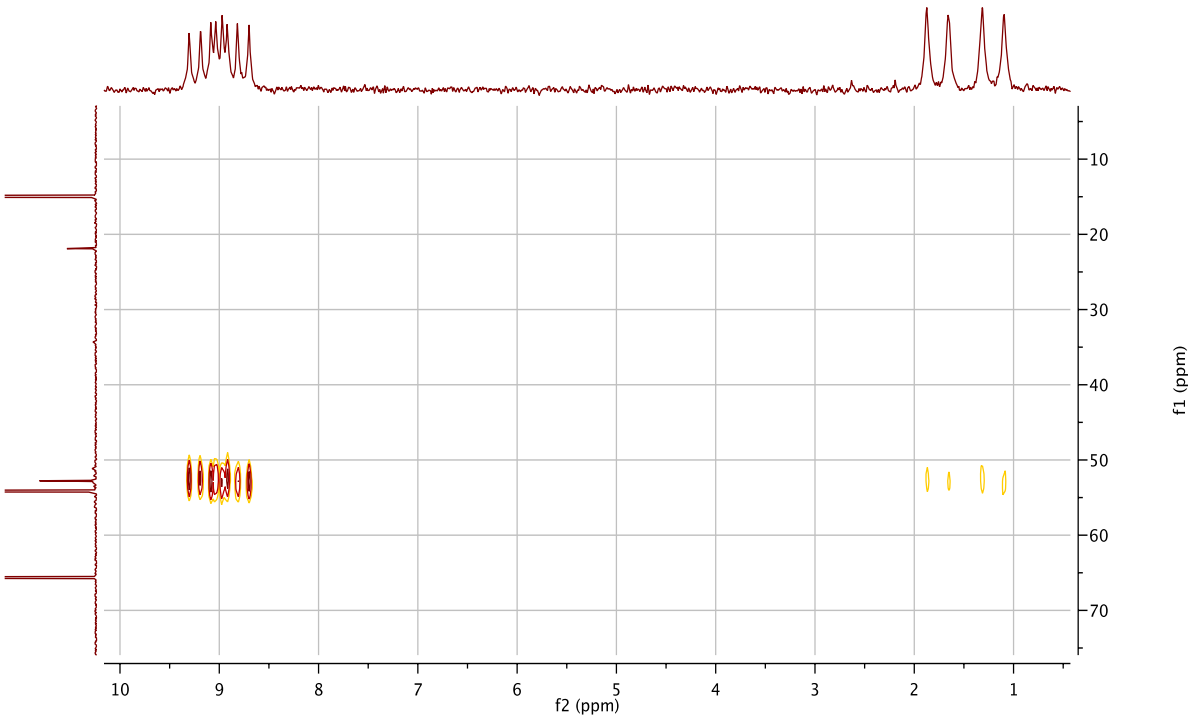

Figure A12. $^{31}P\{^{1}H\}$-$^{13}C\{^{1}H\}$ HMBC of **^{13}C-4-Ac** (242.8,150.8 MHz, CH_2Cl_2, -30 °C, jnxh = 6 Hz)

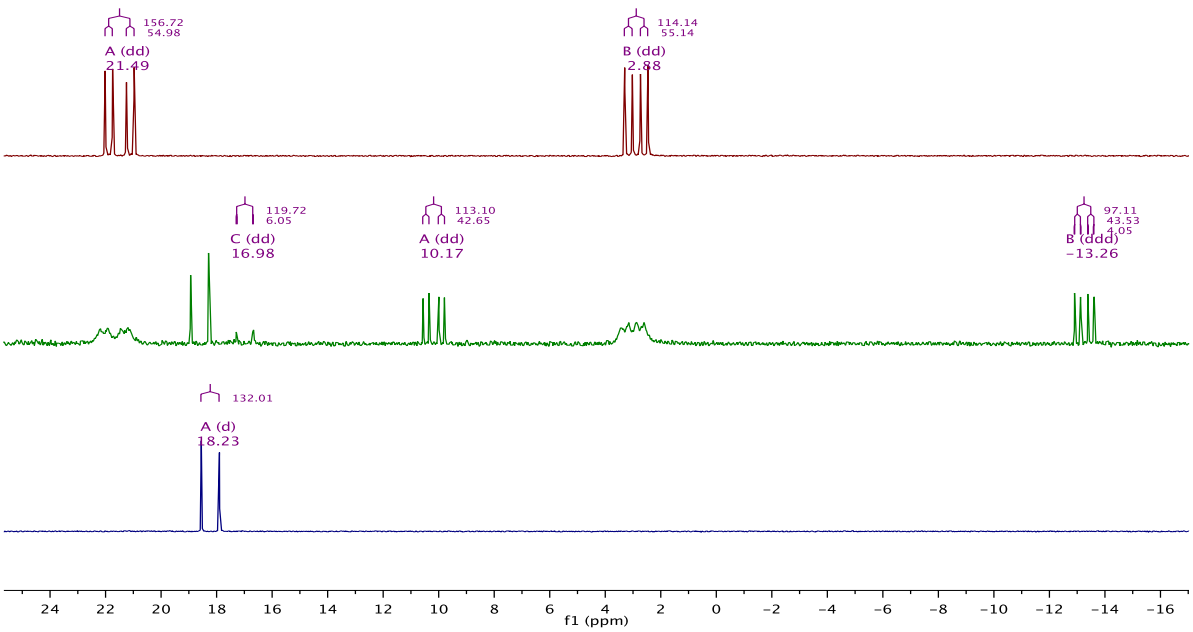

Figure A13. $^{13}P\{^{1}H\}$ NMR spectra from reaction of **1-I** with $^{13}CH_3I$ (202.5 MHz, CH_2Cl_2, -30 °C (top), -10 °C (middle), 24 °C (bottom))

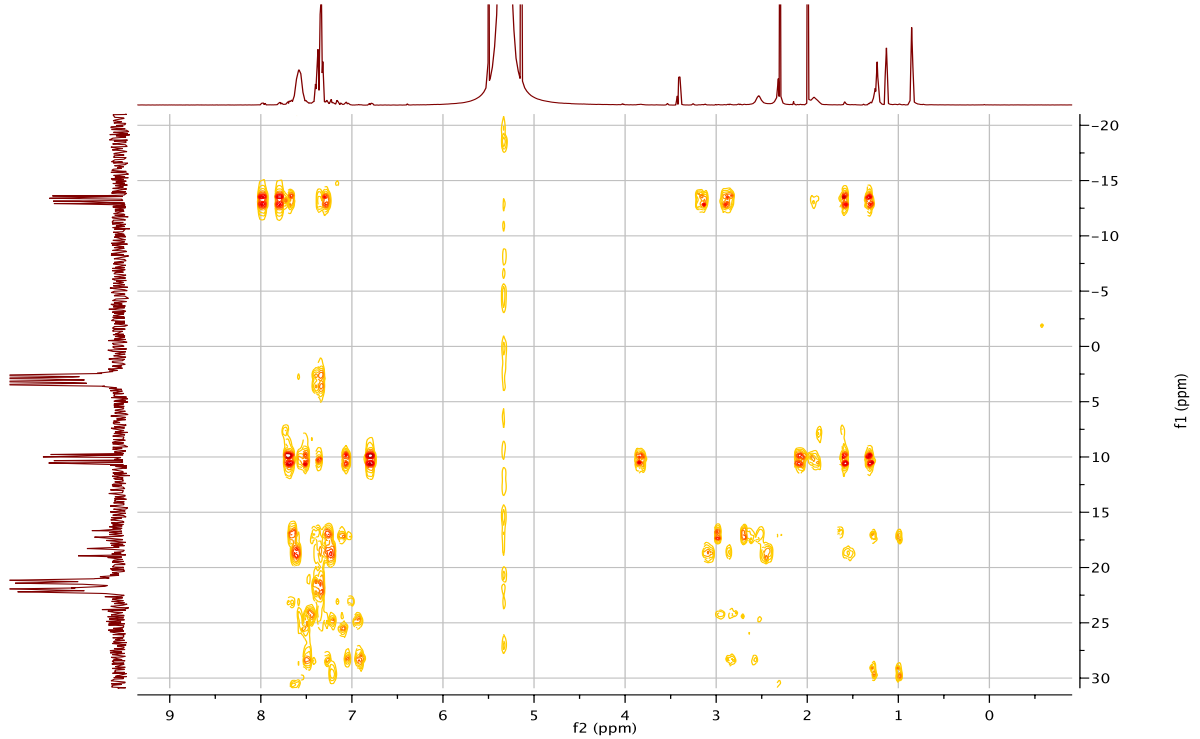

Figure A14. ^{1}H-^{31}P HMBC of reaction of **1-I** with $^{13}CH_3I$ (500.2 MHz, 202.5 MHz, CH_2Cl_2, -10 °C, jnxh = 12 Hz), corresponding to Figure A13 (middle).

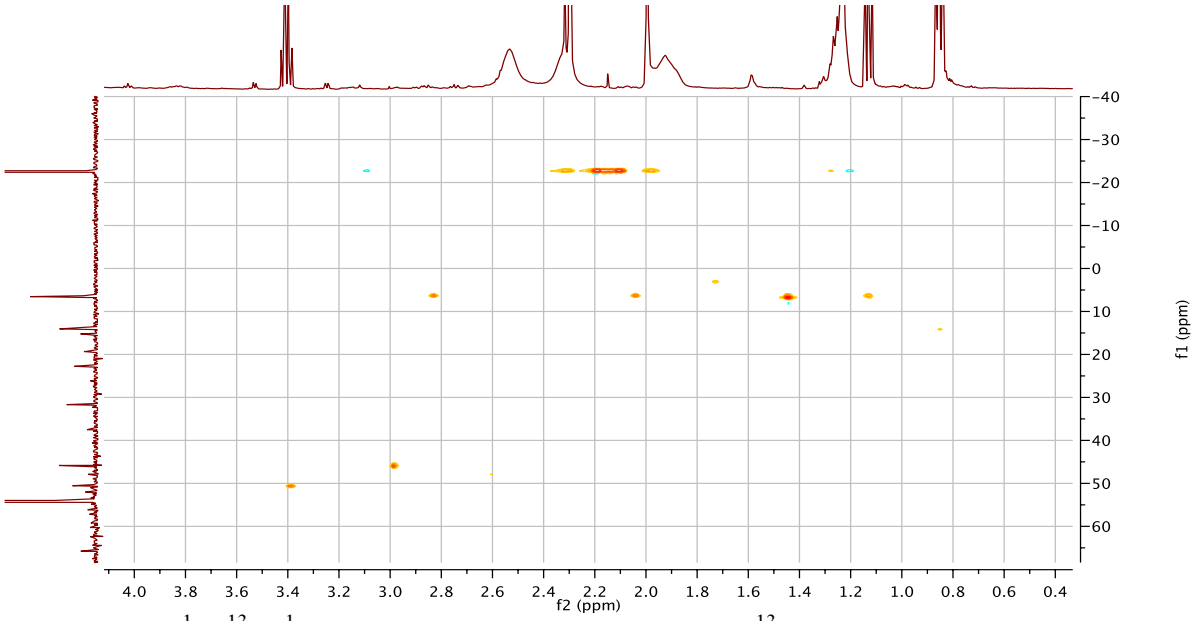

Figure A15. ^{1}H-^{13}C{^{1}H} HSQC of reaction of **1-I** with $^{13}CH_3I$ (500.2 MHz, 125.8 MHz, CH_2Cl_2, -10 °C, j1xh = 145 Hz), corresponding to Figure S13 (middle).

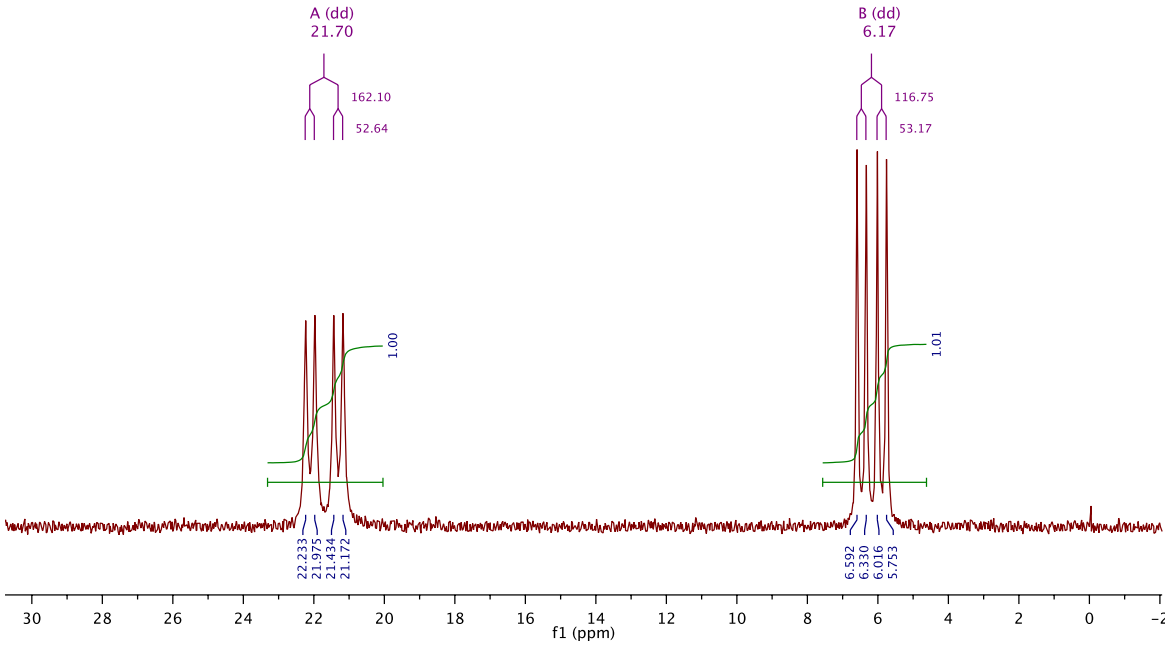

Figure A16. $^{31}P\{^{1}H\}$ NMR spectrum of **1-I$_{OEt}$** (202.5 MHz, CD_2Cl_2, 24°C).

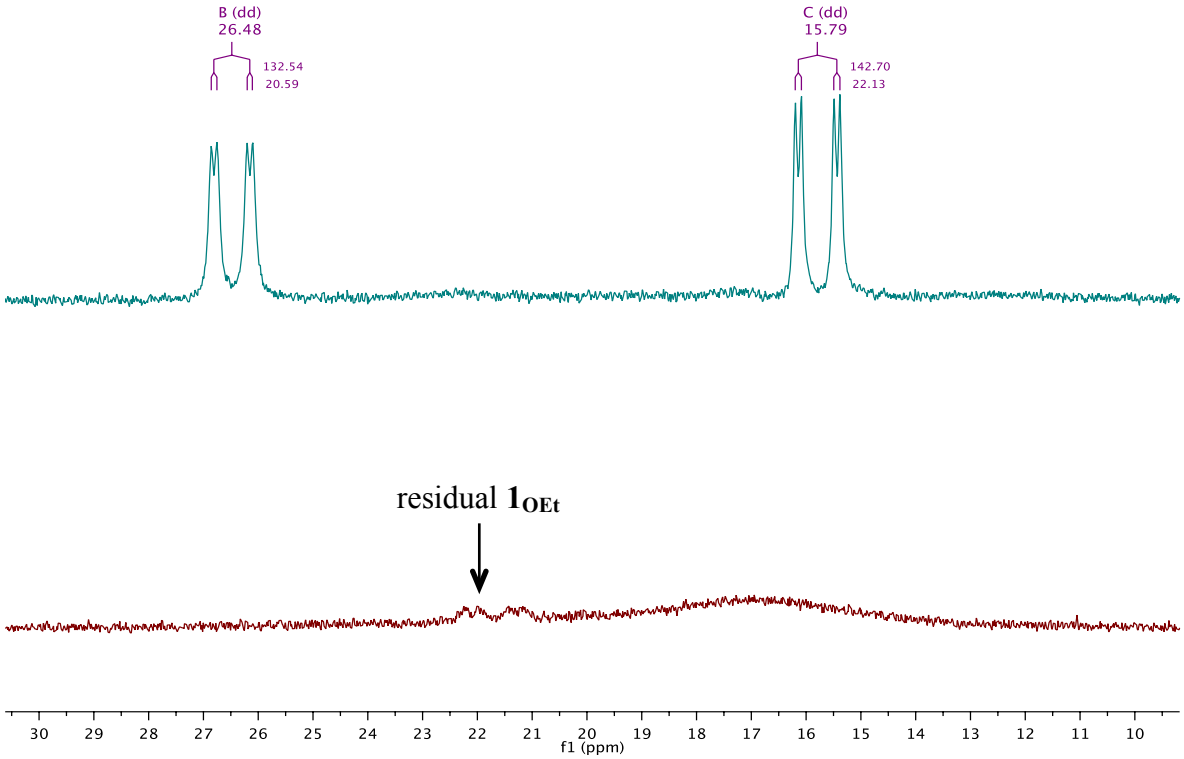

Figure A17. $^{31}P\{^{1}H\}$ NMR spectrum of **3-Ac$_{OEt}$** (202.5 MHz, CD_2Cl_2) at -30 °C (top) and 24 °C (bottom) .

A.2. Kinetic Data

*A.2.1 Overall MRC catalyzed by **1-I** monitored by WiHP-NMRR*

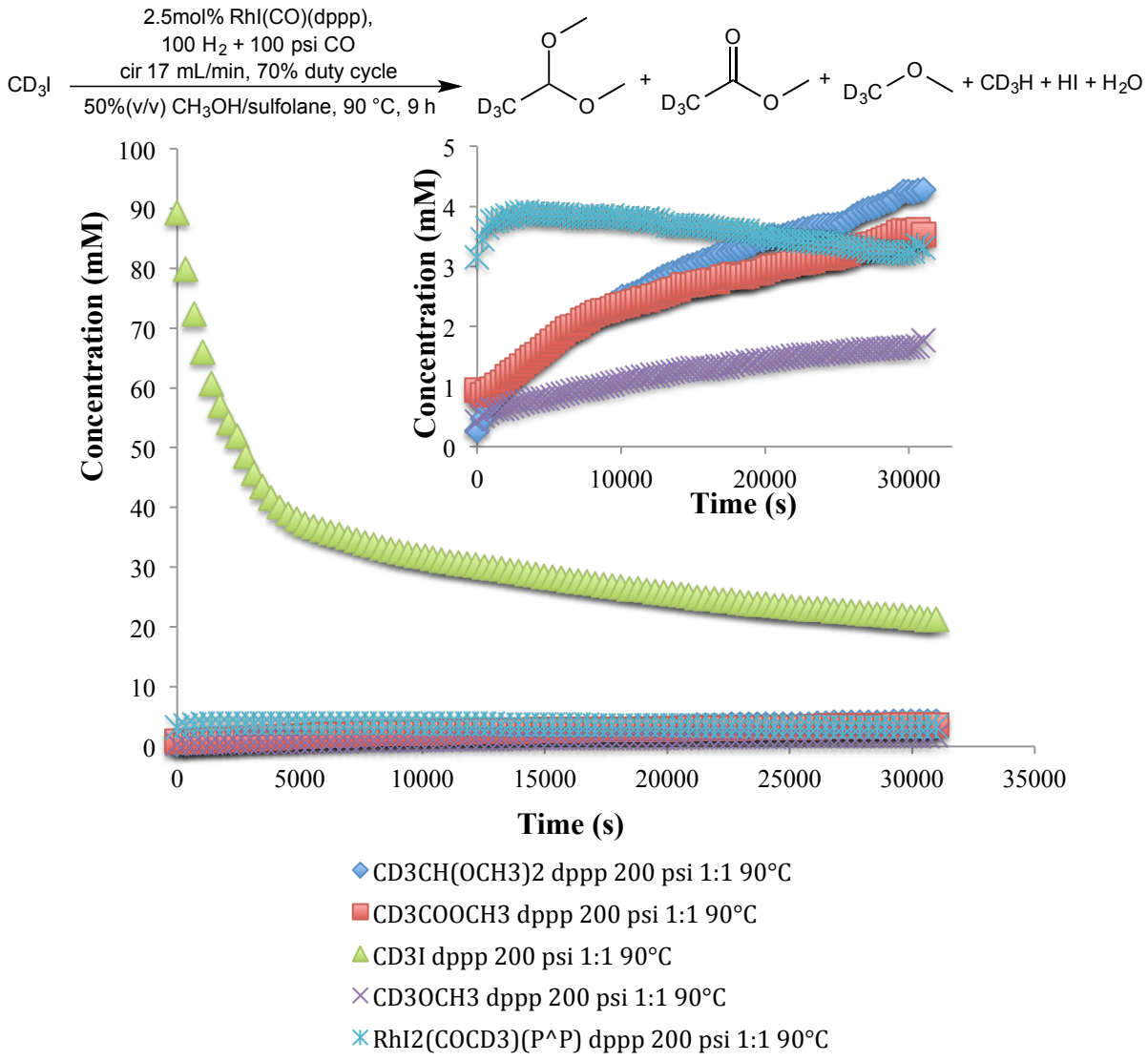

Figure A18. MRC catalyzed by **1-I** monitoring by ^{2}H NMR spectroscopy, 4.0 mM [Rh], 200 psig 1:1 H_2/CO at 90 °C in MeOH/sulfolane, inset showing low concentration region.

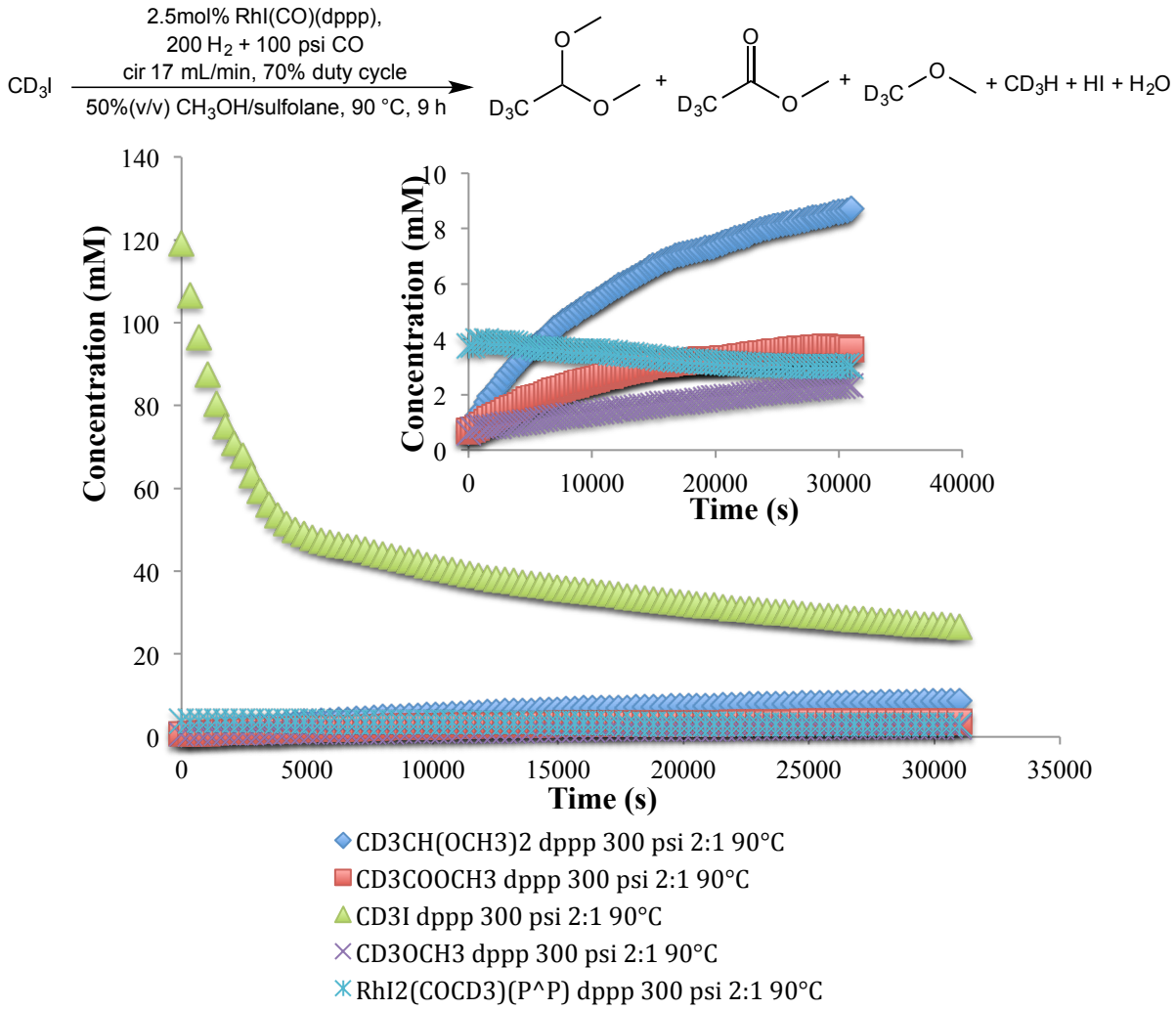

Figure A19. MRC catalyzed by **1-I** monitoring by ^{2}H NMR spectroscopy, 4.0 mM [Rh], 300 psig 2:1 H_2/CO at 90 °C in MeOH/sulfolane, inset showing low concentration region.

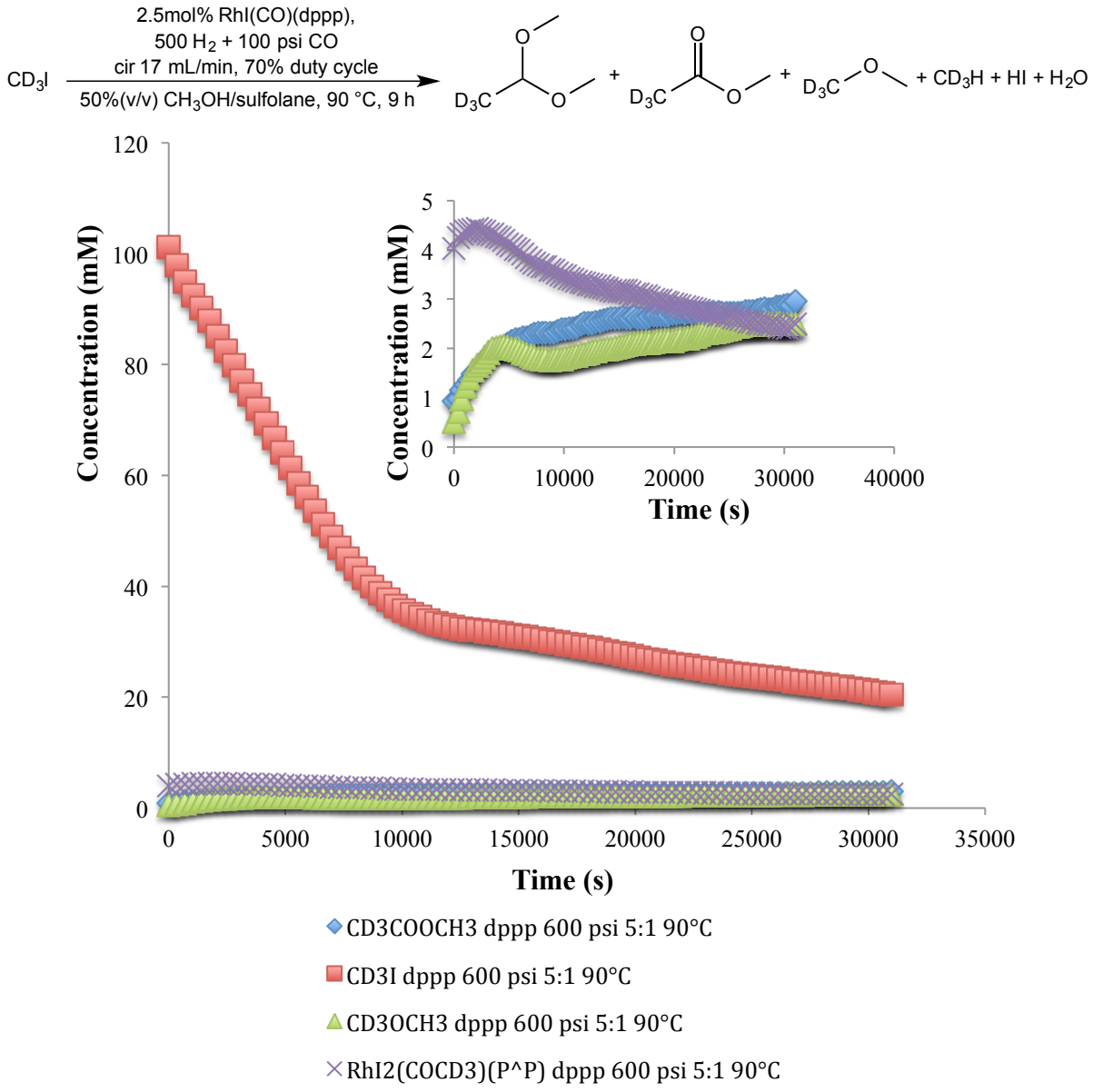

Figure A20. MRC catalyzed by **1-I** monitoring by ^{2}H NMR spectroscopy, 4.0 mM [Rh], 600 psig 5:1 H_2/CO at 90 °C in MeOH/sulfolane, inset showing low concentration region.

*A.2.2. Monitoring and data fitting of oxidative addition of CH_3I to **1-I***

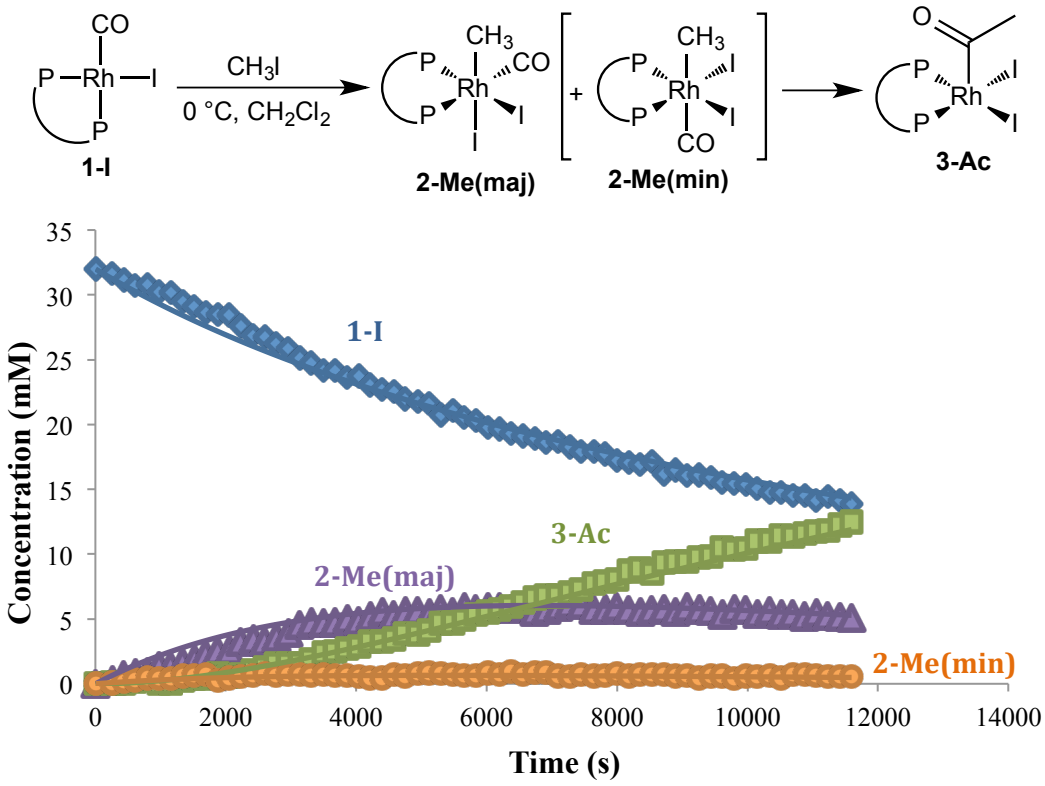

Figure A21. Oxidative addition of CH_3I to **1-I** monitoring by ^{31}P NMR spectroscopy, 0 °C in CH_2Cl_2, $[CH_3I]_0 = 64$ mM

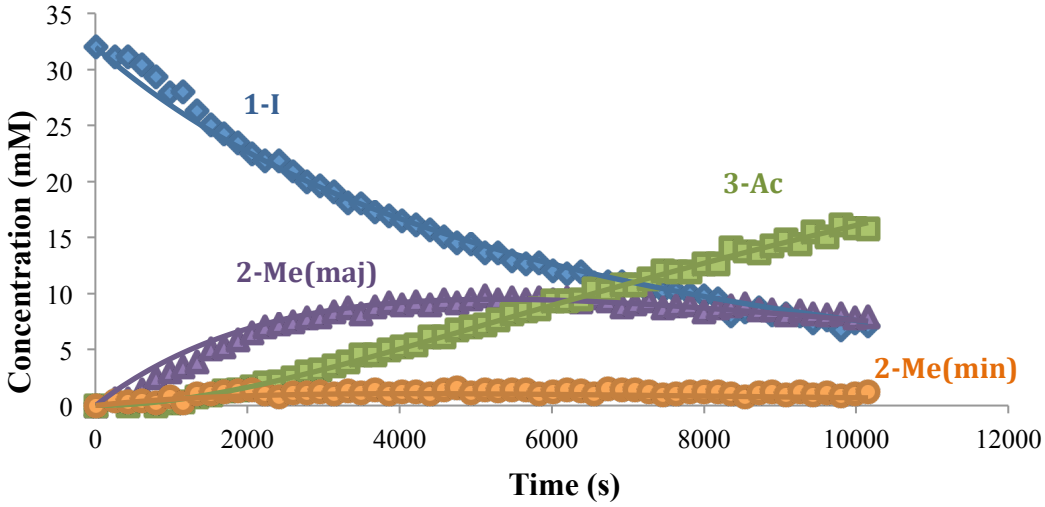

Figure A22. Oxidative addition of CH_3I to **1-I** monitoring by ^{31}P NMR spectroscopy, 0 °C in CH_2Cl_2, $[CH_3I]_0 = 128$ mM

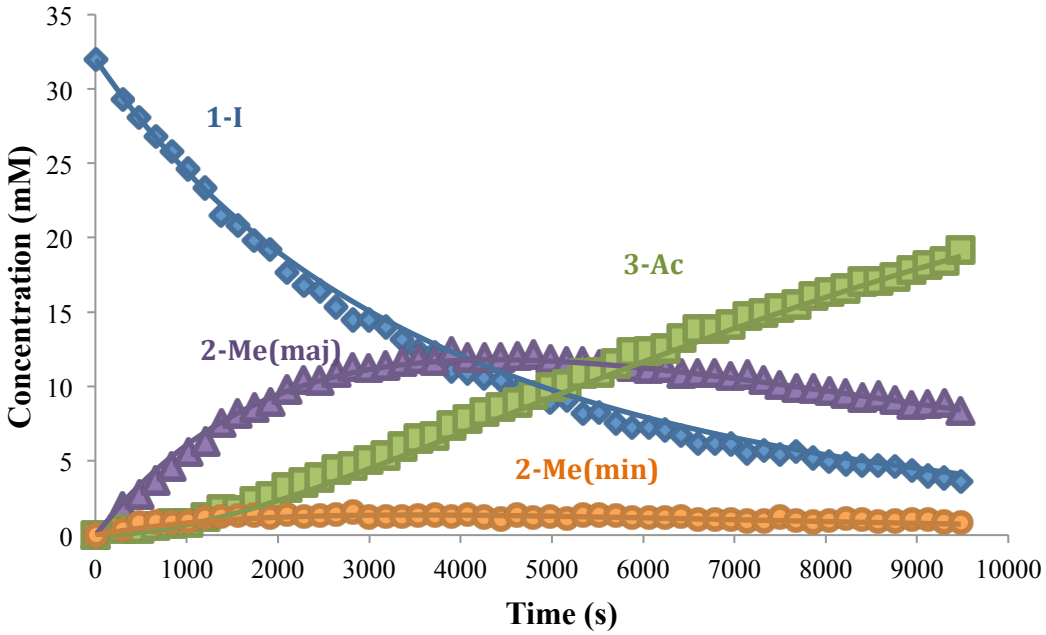

Figure A23. Oxidative addition of CH_3I to **1-I** monitoring by ^{31}P NMR spectroscopy, 0 °C in CH_2Cl_2, $[CH_3I]_0 = 192$ mM

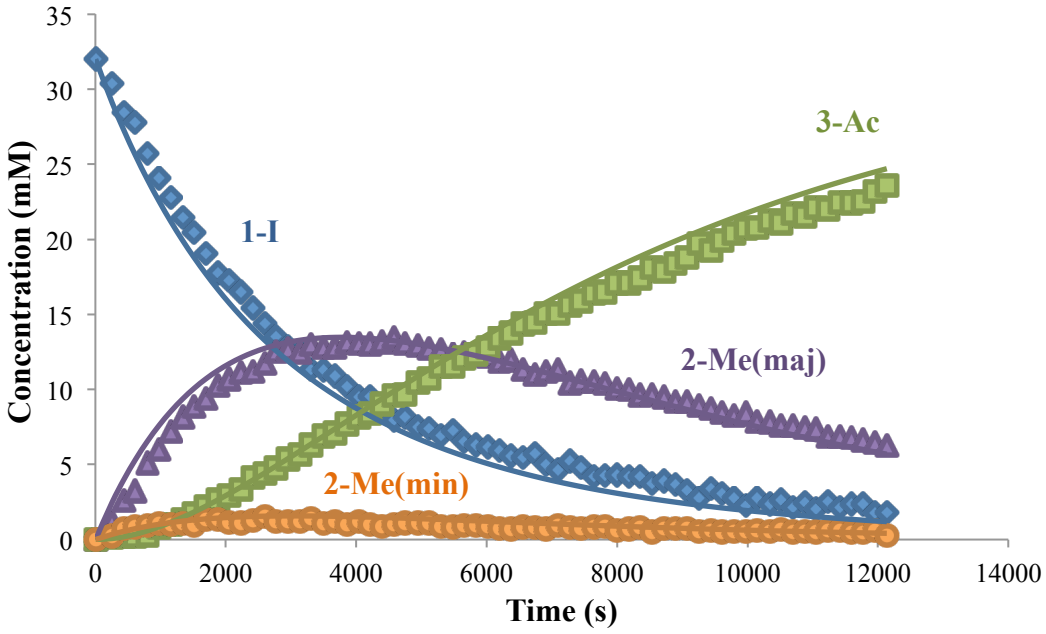

Figure A24. Oxidative addition of CH_3I to **1-I** monitoring by ^{31}P NMR spectroscopy, 0 °C in CH_2Cl_2, $[CH_3I]_0 = 256$ mM

A.3. X-ray Crystallography Data

A.3.1. [RhI(CO)(dppp)], ***1-I***

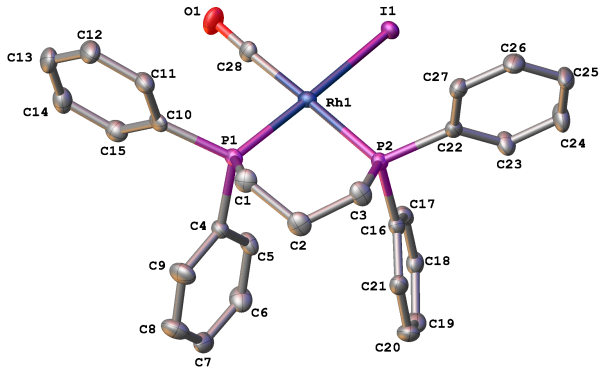

Figure A25. A molecular drawing of **1-I**. Only one conformer of the co-crystallized complex is shown. All atoms are shown as 50% thermal probability ellipsoids. All H atoms are omitted for clarity.

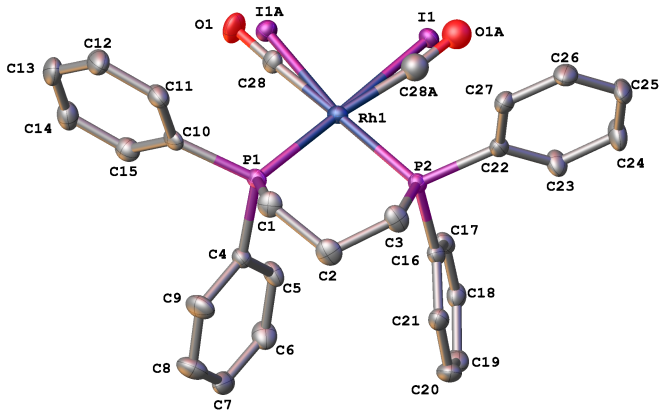

Figure A26. The asymmetric unit of **1-I**. The asymmetric unit consists of a disordered pair of conformers with the major component present 82.8(2)% of the time. All atoms are shown as 50% thermal probability ellipsoids. All H atoms are omitted for clarity.

Table A1. Crystal data and structure refinement for **1-I.**

Empirical formula	$C_{28}H_{26}IOP_2Rh$
Formula weight	670.24
Temperature/K	100.0
λ/Å	0.71073
Crystal system	monoclinic
Space group	$P2_1/n$
a/Å	13.026(4)
b/Å	9.313(3)
c/Å	21.323(7)
α/°	90
β/°	93.087(16)
γ/°	90
Volume/Å^3	2583.1(14)
Z	4
ρ_{calc} mg/mm^3	1.723
μ/mm^{-1}	1.999
F(000)	1320.0
Crystal size/mm^3	0.21 × 0.126 × 0.047
2Θ range for data collection	3.58 to 54.14°
Index ranges	$-16 \leq h \leq 16$, $-11 \leq k \leq 11$, $-27 \leq l \leq 27$
Reflections collected	54689
Independent reflections	5667[R(int) = 0.0570]
Data/restraints/parameters	5667/0/316
Goodness-of-fit on F^2	1.338
Final R indexes [I>=2σ (I)]	$R_1 = 0.0401$, $wR_2 = 0.0988$
Final R indexes [all data]	$R_1 = 0.0422$, $wR_2 = 0.0995$
Largest diff. peak/hole / e Å^{-3}	0.65/-0.74

Table A2. Fractional Atomic Coordinates ($\times 10^4$) and Equivalent Isotropic Displacement Parameters ($Å^2 \times 10^3$) for **1-I**. U_{eq} is defined as 1/3 of of the trace of the orthogonalised U_{IJ} tensor.

Atom	*x*	*y*	*z*	U(eq)
I1	4908.5(3)	11201.6(4)	3147.6(3)	17.69(14)
I1A	4383.2(17)	11478(3)	1642.1(14)	20.0(7)
Rh1	4371.5(3)	9200.0(4)	2307.60(17)	15.59(11)
P1	3965.6(9)	7571.5(13)	1553.9(6)	17.0(2)
P2	4466.8(9)	7353.7(13)	3049.6(6)	16.1(2)
O1	4310(5)	11588(7)	1338(4)	33.7(16)
O1A	4880(20)	11180(30)	3414(18)	34(9)
C1	3044(4)	6190(6)	1768(2)	23.5(10)
C2	3459(4)	5163(6)	2283(3)	26.1(11)
C3	3570(4)	5852(6)	2930(2)	24.7(11)
C4	5025(4)	6514(5)	1289(2)	18.8(10)
C5	6038(4)	6819(6)	1489(2)	22.8(10)
C6	6842(4)	5976(7)	1309(3)	30.8(12)
C7	6656(4)	4795(6)	922(2)	28.2(12)
C8	5661(5)	4474(6)	724(3)	35.3(13)
C9	4853(4)	5316(6)	897(3)	31.4(13)
C10	3360(4)	8307(5)	827(2)	20.3(10)
C11	2310(4)	8596(6)	794(2)	26.3(11)
C12	1873(4)	9279(7)	269(3)	31.4(12)
C13	2456(5)	9646(7)	-227(3)	33.0(13)
C14	3490(5)	9333(6)	-196(3)	31.1(12)
C15	3952(4)	8678(6)	325(2)	26.1(11)
C16	5754(4)	6570(5)	3084(2)	19.1(10)
C17	6604(4)	7482(6)	3086(2)	21(1)
C18	7587(4)	6925(6)	3088(2)	23.9(11)
C19	7738(4)	5449(6)	3064(3)	27.8(12)
C20	6905(4)	4539(6)	3067(3)	29.6(12)
C21	5910(4)	5089(6)	3078(2)	23.9(11)
C22	4232(4)	7794(5)	3864(2)	19.5(10)
C23	5018(4)	7835(6)	4334(2)	26.8(11)
C24	4804(4)	8171(7)	4947(3)	33.8(13)
C25	3809(5)	8439(7)	5103(2)	32.1(13)

C26	3008(4)	8391(6)	4641(3)	28.7(12)
C27	3226(4)	8085(6)	4026(2)	23.5(10)
C28	4327(5)	10664(10)	1697(3)	19.5(13)
C28A	4630(30)	10310(50)	3030(18)	38(8)

Table A3. Anisotropic Displacement Parameters ($Å^2 \times 10^3$) for **1-I**. The Anisotropic displacement factor exponent takes the form: $-2\pi^2[h^2a^{*2}U_{11}+...+2hka \times b \times U_{12}]$

Atom	U_{11}	U_{22}	U_{33}	U_{23}	U_{13}	U_{12}
I1	18.6(2)	16.3(2)	18.1(3)	-3.81(16)	0.47(15)	-1.55(14)
I1A	20.6(10)	17.6(14)	21.7(15)	1.0(12)	-0.7(10)	-1.7(9)
Rh1	13.11(17)	14.08(18)	19.53(19)	-1.91(14)	0.39(13)	-0.86(13)
P1	15.8(6)	17.6(6)	17.6(6)	-4.0(5)	-0.8(4)	-1.8(5)
P2	17.1(6)	16.2(6)	15.1(6)	-0.4(4)	2.0(4)	-0.9(5)
O1	48(4)	29(3)	24(3)	9(3)	-2(3)	-6(2)
C1	19(2)	24(3)	27(3)	-2(2)	-0.5(19)	-9(2)
C2	27(3)	22(3)	29(3)	-2(2)	2(2)	-9(2)
C3	27(3)	24(3)	24(3)	0(2)	7(2)	-9(2)
C4	20(2)	19(2)	17(2)	-3.2(18)	1.8(18)	1.7(18)
C5	20(2)	30(3)	19(2)	-6(2)	2.6(19)	-4(2)
C6	21(3)	44(3)	27(3)	-3(3)	3(2)	3(2)
C7	34(3)	31(3)	21(2)	5(2)	9(2)	10(2)
C8	40(3)	24(3)	42(3)	-11(3)	7(3)	3(2)
C9	29(3)	25(3)	39(3)	-13(2)	-2(2)	-2(2)
C10	22(2)	20(2)	19(2)	-7.5(19)	-4.0(18)	-0.1(19)
C11	24(3)	33(3)	22(2)	-7(2)	-1(2)	5(2)
C12	29(3)	40(3)	25(3)	-4(2)	-6(2)	9(2)
C13	42(3)	36(3)	19(3)	-1(2)	-8(2)	4(3)
C14	39(3)	34(3)	20(3)	-1(2)	0(2)	-2(3)
C15	24(3)	27(3)	27(3)	-4(2)	1(2)	-1(2)
C16	23(2)	20(2)	14(2)	-0.1(18)	3.2(18)	2.5(19)
C17	26(3)	20(2)	17(2)	-1.7(19)	4.4(19)	0(2)
C18	24(2)	31(3)	17(2)	2(2)	2.4(19)	1(2)
C19	25(3)	34(3)	24(3)	-2(2)	3(2)	10(2)
C20	38(3)	22(3)	29(3)	-4(2)	-2(2)	9(2)
C21	32(3)	19(2)	20(2)	0(2)	-1(2)	2(2)
C22	26(2)	16(2)	16(2)	0.6(18)	2.1(19)	1.7(19)
C23	22(2)	39(3)	20(2)	-5(2)	3(2)	3(2)

C24	33(3)	51(4)	17(2)	-6(2)	-2(2)	2(3)
C25	37(3)	44(3)	15(2)	-4(2)	3(2)	15(3)
C26	28(3)	35(3)	24(3)	0(2)	5(2)	12(2)
C27	27(3)	25(3)	19(2)	3(2)	0(2)	6(2)
C28	21(3)	19(4)	19(3)	-1(3)	-4(2)	-5(3)

Table A4. Bond Lengths for **1-I**.

Atom	Atom	Length/Å	Atom	Atom	Length/Å
I1	Rh1	2.6529(8)	C7	C8	1.374(8)
I1A	Rh1	2.553(3)	C8	C9	1.379(8)
Rh1	P1	2.2520(13)	C10	C11	1.393(7)
Rh1	P2	2.3354(14)	C10	C15	1.395(7)
Rh1	C28	1.884(9)	C11	C12	1.383(8)
Rh1	C28A	1.87(4)	C12	C13	1.379(8)
P1	C1	1.834(5)	C13	C14	1.377(8)
P1	C4	1.810(5)	C14	C15	1.377(8)
P1	C10	1.834(5)	C16	C17	1.394(7)
P2	C3	1.832(5)	C16	C21	1.395(7)
P2	C16	1.827(5)	C17	C18	1.382(7)
P2	C22	1.825(5)	C18	C19	1.390(8)
O1	C28	1.151(11)	C19	C20	1.377(8)
O1A	C28A	1.19(5)	C20	C21	1.395(8)
C1	C2	1.533(7)	C22	C23	1.395(7)
C2	C3	1.522(7)	C22	C27	1.400(7)
C4	C5	1.394(7)	C23	C24	1.385(7)
C4	C9	1.406(7)	C24	C25	1.379(8)
C5	C6	1.380(7)	C25	C26	1.396(8)
C6	C7	1.388(8)	C26	C27	1.387(7)

Table A5. Bond Angles for **1-I**.

Atom	Atom	Atom	Angle/°	Atom	Atom	Atom	Angle/°
P1	Rh1	I1	176.71(4)	C5	C6	C7	120.4(5)
P1	Rh1	I1A	99.86(8)	C8	C7	C6	119.1(5)
P1	Rh1	P2	89.40(5)	C7	C8	C9	121.0(5)
P2	Rh1	I1	93.29(4)	C8	C9	C4	120.7(5)
P2	Rh1	I1A	170.66(7)	C11	C10	P1	119.4(4)
C28	Rh1	I1	87.4(2)	C11	C10	C15	119.7(5)
C28	Rh1	P1	89.8(2)	C15	C10	P1	120.7(4)
C28	Rh1	P2	178.3(2)	C12	C11	C10	119.3(5)
C28A	Rh1	I1A	89.7(12)	C13	C12	C11	121.0(5)
C28A	Rh1	P1	169.9(12)	C14	C13	C12	119.2(5)
C28A	Rh1	P2	81.2(12)	C13	C14	C15	121.1(5)
C1	P1	Rh1	115.25(18)	C14	C15	C10	119.5(5)
C4	P1	Rh1	115.80(16)	C17	C16	P2	118.9(4)
C4	P1	C1	102.5(2)	C17	C16	C21	119.1(5)
C4	P1	C10	103.9(2)	C21	C16	P2	121.9(4)
C10	P1	Rh1	115.19(16)	C18	C17	C16	120.5(5)
C10	P1	C1	102.4(2)	C17	C18	C19	120.2(5)
C3	P2	Rh1	117.24(18)	C20	C19	C18	119.7(5)
C16	P2	Rh1	109.65(16)	C19	C20	C21	120.5(5)
C16	P2	C3	106.1(2)	C16	C21	C20	119.9(5)
C22	P2	Rh1	118.24(16)	C23	C22	P2	122.4(4)
C22	P2	C3	99.6(2)	C23	C22	C27	118.5(5)
C22	P2	C16	104.6(2)	C27	C22	P2	119.0(4)
C2	C1	P1	114.0(3)	C24	C23	C22	120.5(5)
C3	C2	C1	113.5(5)	C25	C24	C23	120.5(5)
C2	C3	P2	118.5(4)	C24	C25	C26	120.0(5)
C5	C4	P1	121.3(4)	C27	C26	C25	119.4(5)
C5	C4	C9	117.5(5)	C26	C27	C22	121.0(5)
C9	C4	P1	121.2(4)	O1	C28	Rh1	177.9(7)
C6	C5	C4	121.3(5)	O1A	C28A	Rh1	167(4)

Table A6. Torsion Angles for **1-I**.

A	B	C	D	Angle/°	A	B	C	D	Angle/°
I1	Rh1	C28A	O1A	-7(11)	C4	C5	C6	C7	-0.1(8)
I1A	Rh1	C28A	O1A	-31(15)	C5	C4	C9	C8	0.6(8)
Rh1	P1	C1	C2	-66.9(4)	C5	C6	C7	C8	-0.3(9)
Rh1	P1	C4	C5	-7.4(5)	C6	C7	C8	C9	0.9(9)
Rh1	P1	C4	C9	169.8(4)	C7	C8	C9	C4	-1.1(10)
Rh1	P1	C10	C11	-81.9(4)	C9	C4	C5	C6	-0.1(8)
Rh1	P1	C10	C15	93.3(4)	C10	P1	C1	C2	167.2(4)
Rh1	P2	C3	C2	48.1(5)	C10	P1	C4	C5	120.0(4)
Rh1	P2	C16	C17	43.7(4)	C10	P1	C4	C9	-62.8(5)
Rh1	P2	C16	C21	-133.2(4)	C10	C11	C12	C13	1.6(9)
Rh1	P2	C22	C23	-107.5(4)	C11	C10	C15	C14	0.3(8)
Rh1	P2	C22	C27	73.3(4)	C11	C12	C13	C14	-0.4(9)
P1	Rh1	C28A	O1A	170(10)	C12	C13	C14	C15	-0.8(9)
P1	C1	C2	C3	71.7(5)	C13	C14	C15	C10	0.9(9)
P1	C4	C5	C6	177.2(4)	C15	C10	C11	C12	-1.5(8)
P1	C4	C9	C8	-176.6(5)	C16	P2	C3	C2	-74.7(5)
P1	C10	C11	C12	173.7(4)	C16	P2	C22	C23	14.8(5)
P1	C10	C15	C14	-174.9(4)	C16	P2	C22	C27	-164.3(4)
P2	Rh1	C28A	O1A	148(15)	C16	C17	C18	C19	2.4(8)
P2	C16	C17	C18	-177.6(4)	C17	C16	C21	C20	-0.7(8)
P2	C16	C21	C20	176.2(4)	C17	C18	C19	C20	-2.9(8)
P2	C22	C23	C24	-179.8(5)	C18	C19	C20	C21	1.6(8)
P2	C22	C27	C26	178.4(4)	C19	C20	C21	C16	0.2(8)
C1	P1	C4	C5	-133.7(4)	C21	C16	C17	C18	-0.6(7)
C1	P1	C4	C9	43.5(5)	C22	P2	C3	C2	176.9(4)
C1	P1	C10	C11	44.0(5)	C22	P2	C16	C17	-84.1(4)
C1	P1	C10	C15	-140.8(4)	C22	P2	C16	C21	99.1(4)
C1	C2	C3	P2	-62.7(6)	C22	C23	C24	C25	1.5(10)
C3	P2	C16	C17	171.2(4)	C23	C22	C27	C26	-0.7(8)
C3	P2	C16	C21	-5.6(5)	C23	C24	C25	C26	-0.8(10)
C3	P2	C22	C23	124.3(5)	C24	C25	C26	C27	-0.6(9)
C3	P2	C22	C27	-54.8(5)	C25	C26	C27	C22	1.4(9)
C4	P1	C1	C2	59.8(4)	C27	C22	C23	C24	-0.7(8)
C4	P1	C10	C11	150.4(4)	C28	Rh1	C28A	O1A	-31(15)

C4 P1 C10 C15 -34.4(5)

Table A7. Hydrogen Atom Coordinates (Å×10^4) and Isotropic Displacement Parameters (Å^2×10^3) for **1-I**.

Atom	*x*	*y*	*z*	U(eq)
H1A	2420	6668	1912	28
H1B	2839	5624	1389	28
H2A	2989	4329	2301	31
H2B	4138	4799	2169	31
H3A	3779	5091	3235	30
H3B	2881	6189	3039	30
H5	6178	7623	1754	27
H6	7527	6204	1450	37
H7	7209	4216	795	34
H8	5528	3659	464	42
H9	4172	5084	749	38
H11	1897	8327	1129	32
H12	1160	9499	251	38
H13	2147	10109	-587	40
H14	3892	9572	-540	37
H15	4669	8481	343	31
H17	6505	8492	3085	25
H18	8162	7554	3105	29
H19	8413	5070	3046	33
H20	7009	3530	3062	36
H21	5339	4455	3081	29
H23	5705	7630	4234	32
H24	5348	8217	5261	41
H25	3668	8656	5525	38
H26	2321	8566	4748	34
H27	2684	8072	3710	28

A.3.2. [RhI(CO)(dpppOEt)], ***1-I$_{OEt}$***

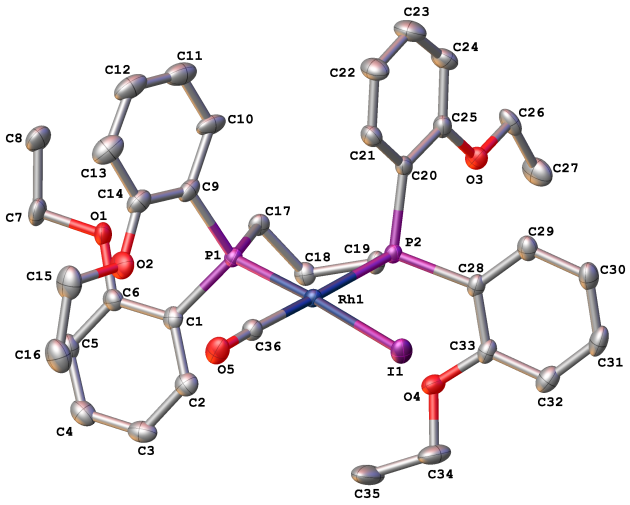

Figure A27. The rhodium complex of **1-I$_{OEt}$**. All atoms are drawn as 50% thermal probability ellipsoids. All H atoms and minor components of disorder are omitted for clarity.

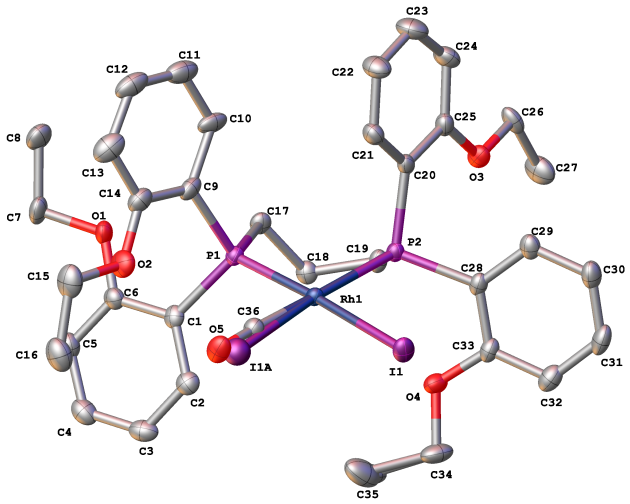

Figure A28. The asymmetric unit of **1-I$_{OEt}$**, including all disordered components. All atoms are drawn as 50% thermal probability ellipsoids. All H atoms are omitted for clarity.

Table A8. Crystal data and structure refinement for **1-I_{OEt}**.

Empirical formula	$C_{36}H_{42}IO_5P_2Rh$
Formula weight	846.44
Temperature/K	100.0
Crystal system	triclinic
Space group	$P\bar{1}$
a/Å	8.995(3)
b/Å	13.550(3)
c/Å	15.846(5)
α/°	105.554(15)
β/°	105.922(14)
γ/°	95.499(15)
Volume/$Å^3$	1759.3(9)
Z	2
$\rho_{calc}g/cm^3$	1.598
μ/mm^{-1}	1.494
F(000)	852.0
Crystal size/mm^3	0.05 × 0.04 × 0.03
Radiation	MoKα (λ = 0.71073)
2Θ range for data collection/°	2.808 to 61.414
Index ranges	$-12 \leq h \leq 12$, $-19 \leq k \leq 19$, $-22 \leq l \leq 22$
Reflections collected	51444
Independent reflections	10856 [R_{int} = 0.0719, R_{sigma} = 0.0649]
Data/restraints/parameters	10856/7/426
Goodness-of-fit on F^2	1.028
Final R indexes [I>=2σ (I)]	R_1 = 0.0409, wR_2 = 0.0817
Final R indexes [all data]	R_1 = 0.0720, wR_2 = 0.0933
Largest diff. peak/hole / e $Å^{-3}$	0.96/-0.93

Table A9. Fractional Atomic Coordinates ($\times 10^4$) and Equivalent Isotropic Displacement Parameters ($Å^2 \times 10^3$) for **1-I_{OEt}**. U_{eq} is defined as 1/3 of of the trace of the orthogonalised U_{IJ} tensor.

Atom	*x*	*y*	*z*	U(eq)
Rh1	9342.3(3)	5145.3(2)	2491.3(2)	15.48(7)
P1	7076.4(10)	4045.4(6)	2147.6(6)	16.90(16)
P2	8136.0(9)	6585.7(6)	2968.7(6)	16.70(16)
O1	4543(3)	2142.2(17)	1343.3(16)	23.7(5)
O2	8232(3)	2083.1(19)	2052.2(18)	30.2(6)
O3	6523(3)	8092.7(18)	4011.9(16)	24.6(5)
O4	8693(3)	7247.5(18)	1499.9(16)	24.6(5)
C1	6403(4)	3142(2)	968(2)	19.4(6)
C2	7066(4)	3325(3)	319(2)	22.8(7)
C3	6579(4)	2664(3)	-582(2)	27.5(8)
C4	5421(4)	1801(3)	-837(2)	28.5(8)
C5	4725(4)	1599(3)	-205(2)	26.1(7)
C6	5193(4)	2272(3)	689(2)	21.5(7)
C7	3676(4)	1137(3)	1201(3)	29.7(8)
C8	3409(5)	1145(3)	2099(3)	33.8(9)
C9	7166(4)	3274(3)	2938(2)	23.5(7)
C10	6694(4)	3660(3)	3734(2)	28.9(8)
C11	6883(4)	3112(3)	4377(3)	37.1(10)
C12	7523(4)	2226(3)	4242(3)	36.2(9)
C13	7987(4)	1830(3)	3482(3)	36.0(9)
C14	7812(4)	2382(3)	2825(2)	26.9(8)
C15	8859(5)	1152(3)	1849(3)	36.9(9)
C16	9074(5)	980(3)	907(3)	39.5(10)
C17	5342(4)	4640(3)	2153(2)	20.1(6)
C18	5279(4)	5431(2)	1615(2)	20.9(7)
C19	6129(4)	6514(2)	2218(2)	19.3(6)
C20	7953(4)	6744(2)	4112(2)	18.9(6)
C21	8644(4)	6123(3)	4620(2)	23.2(7)
C22	8479(5)	6169(3)	5468(2)	30.7(8)
C23	7562(5)	6831(3)	5815(3)	36.7(9)
C24	6881(4)	7485(3)	5342(2)	29.6(8)
C25	7095(4)	7455(3)	4504(2)	22.4(7)

C26	5473(4)	8748(3)	4284(2)	26.1(8)
C27	4971(5)	9268(3)	3559(3)	36.9(9)
C28	9172(4)	7865(2)	3082(2)	19.0(6)
C29	9861(4)	8628(3)	3926(2)	23.4(7)
C30	10733(4)	9563(3)	3983(3)	27.8(8)
C31	10920(4)	9734(3)	3204(3)	30.1(8)
C32	10257(4)	8979(3)	2356(3)	27.9(8)
C33	9389(4)	8050(3)	2301(2)	21.0(7)
C34	9099(5)	7248(3)	691(2)	35.9(9)
C35	8300(20)	6224(8)	-12(9)	48(3)
C35A	8830(60)	6118(12)	170(30)	57(8)
I1	12109.0(2)	6347.7(2)	2844.1(2)	24.09(7)
O5	11082(5)	3409(3)	2021(3)	31.5(10)
C36	10377(4)	4048(3)	2192(2)	21.6(7)
I1A	11070(30)	3713(14)	2032(14)	31(4)

Table A10. Anisotropic Displacement Parameters ($Å^2 \times 10^3$) for **1-I_{OEt}**. The Anisotropic displacement factor exponent takes the form: $-2\pi^2[h^2a^{*2}U_{11}+2hka^*b^*U_{12}+\ldots]$.

Atom	U_{11}	U_{22}	U_{33}	U_{23}	U_{13}	U_{12}
Rh1	15.08(12)	14.88(13)	18.54(12)	5.53(10)	7.77(9)	3.83(9)
P1	17.3(4)	14.8(4)	20.2(4)	6.4(3)	7.4(3)	3.0(3)
P2	16.2(4)	14.6(4)	20.3(4)	4.8(3)	7.9(3)	2.7(3)
O1	25.4(12)	14.8(12)	28.6(13)	2(1)	11(1)	-1.3(10)
O2	35.6(14)	23.4(13)	38.1(15)	13.7(12)	14.6(12)	14.5(11)
O3	27.2(13)	21.0(13)	32.7(13)	9.1(11)	17.7(11)	10.2(10)
O4	25.6(12)	26.9(13)	22.6(12)	8.6(10)	10(1)	0.6(10)
C1	18.8(15)	17.1(16)	23.0(16)	8.6(13)	4.1(13)	7.4(13)
C2	21.2(16)	23.9(18)	25.0(17)	10.1(14)	6.0(13)	8.0(14)
C3	29.3(19)	37(2)	23.5(17)	14.2(16)	11.0(15)	16.8(16)
C4	29.7(19)	30(2)	23.0(17)	5.1(15)	3.9(14)	11.3(16)
C5	25.0(17)	20.3(18)	30.1(18)	3.9(15)	8.0(15)	4.2(14)
C6	23.7(17)	18.8(17)	23.3(16)	5.8(13)	8.8(13)	7.2(13)
C7	28.1(19)	16.9(18)	43(2)	5.0(16)	15.4(17)	-3.1(15)
C8	31(2)	31(2)	42(2)	12.1(18)	17.7(17)	-2.6(17)
C9	20.7(16)	23.3(18)	26.1(17)	12.4(14)	4.6(13)	-2.6(14)
C10	19.4(17)	43(2)	26.0(18)	15.4(16)	7.7(14)	-5.0(16)
C11	29(2)	53(3)	29(2)	15.8(19)	9.1(16)	-5.3(19)

C12	23.5(19)	51(3)	40(2)	27(2)	8.8(17)	-0.3(18)
C13	23.9(19)	45(2)	46(2)	26(2)	8.8(17)	7.4(17)
C14	22.9(17)	27.9(19)	32.2(19)	13.8(16)	9.0(15)	1.2(15)
C15	31(2)	27(2)	53(3)	12.4(19)	12.4(19)	13.1(17)
C16	36(2)	31(2)	46(2)	3.1(19)	10.6(19)	11.3(18)
C17	14.5(14)	20.8(17)	26.2(16)	6.7(13)	8.9(13)	2.9(12)
C18	17.5(15)	20.8(17)	24.2(16)	6.7(14)	5.5(13)	6.7(13)
C19	15.7(15)	15.3(16)	27.4(17)	6.0(13)	7.7(13)	3.5(12)
C20	19.7(15)	14.5(16)	21.4(15)	2.0(12)	9.3(13)	0.2(12)
C21	25.3(17)	21.0(17)	23.3(17)	3.3(14)	10.4(14)	5.2(14)
C22	39(2)	35(2)	22.1(17)	11.5(16)	11.2(16)	14.7(17)
C23	43(2)	47(3)	23.0(18)	9.3(18)	15.8(17)	12(2)
C24	33(2)	32(2)	25.3(18)	3.9(16)	15.7(16)	9.5(16)
C25	23.7(17)	16.0(16)	27.4(17)	4.0(14)	10.8(14)	2.1(13)
C26	21.2(17)	23.1(18)	27.5(18)	-4.6(14)	8.1(14)	7.1(14)
C27	42(2)	37(2)	35(2)	9.7(18)	14.1(18)	22.7(19)
C28	15.9(15)	15.3(16)	27.2(17)	6.9(13)	8.6(13)	3.5(12)
C29	20.3(16)	18.9(17)	30.7(18)	4.5(14)	9.7(14)	5.3(13)
C30	23.5(17)	19.2(18)	36(2)	2.4(15)	9.6(15)	0.0(14)
C31	26.6(18)	17.6(18)	49(2)	13.9(17)	13.6(17)	3.6(14)
C32	23.8(17)	26.5(19)	39(2)	17.1(17)	11.0(15)	5.9(15)
C33	17.6(15)	16.9(16)	29.7(17)	9.6(14)	7.3(13)	3.0(13)
C34	35(2)	52(3)	26.2(19)	18.3(18)	14.0(16)	1.7(19)
C35	55(8)	60(5)	18(4)	2(3)	14(4)	-18(4)
C35A	44(15)	81(13)	21(12)	-8(10)	7(10)	-20(10)
I1	16.49(11)	22.03(13)	33.76(14)	5.32(10)	11.52(9)	2.20(9)
O5	29.1(17)	26(2)	48(2)	13.0(19)	22.3(13)	11.2(17)
C36	20.6(17)	21.0(18)	24.6(17)	8.0(14)	7.9(14)	4.8(15)

Table A11. Bond Lengths for **1-I_{OEt}**.

Atom	Atom	Length/Å	Atom	Atom	Length/Å
Rh1	P1	2.2463(11)	C9	C10	1.423(5)
Rh1	P2	2.3714(10)	C9	C14	1.381(5)
Rh1	I1	2.6706(8)	C10	C11	1.398(5)
Rh1	C36	1.853(4)	C11	C12	1.371(6)
Rh1	I1A	2.67(2)	C12	C13	1.374(6)
P1	C1	1.835(3)	C13	C14	1.421(5)

P1	C9	1.826(3)	C15	C16	1.517(6)
P1	C17	1.824(3)	C17	C18	1.535(4)
P2	C19	1.847(3)	C18	C19	1.510(4)
P2	C20	1.821(3)	C20	C21	1.390(4)
P2	C28	1.827(3)	C20	C25	1.412(5)
O1	C6	1.364(4)	C21	C22	1.378(5)
O1	C7	1.431(4)	C22	C23	1.383(5)
O2	C14	1.350(4)	C23	C24	1.389(5)
O2	C15	1.426(4)	C24	C25	1.385(5)
O3	C25	1.359(4)	C26	C27	1.494(5)
O3	C26	1.431(4)	C28	C29	1.387(5)
O4	C33	1.371(4)	C28	C33	1.387(4)
O4	C34	1.425(4)	C29	C30	1.392(5)
C1	C2	1.387(5)	C30	C31	1.367(5)
C1	C6	1.406(5)	C31	C32	1.384(5)
C2	C3	1.388(5)	C32	C33	1.384(5)
C3	C4	1.378(5)	C34	C35	1.491(7)
C4	C5	1.388(5)	C34	C35A	1.493(10)
C5	C6	1.387(5)	O5	C36	1.139(6)
C7	C8	1.504(5)			

Table A12. Bond Angles for **1-I$_{OEt}$**.

Atom	Atom	Atom	Angle/°	Atom	Atom	Atom	Angle/°
P1	Rh1	P2	90.37(4)	C14	C9	C10	119.6(3)
P1	Rh1	I1	176.24(2)	C11	C10	C9	118.7(4)
P1	Rh1	I1A	97.5(4)	C12	C11	C10	120.2(4)
P2	Rh1	I1	93.32(3)	C11	C12	C13	122.6(4)
P2	Rh1	I1A	172.1(4)	C12	C13	C14	117.7(4)
C36	Rh1	P1	91.57(11)	O2	C14	C9	115.2(3)
C36	Rh1	P2	176.39(10)	O2	C14	C13	123.8(3)
C36	Rh1	I1	84.78(11)	C9	C14	C13	121.1(4)
C1	P1	Rh1	114.22(11)	O2	C15	C16	107.3(3)
C9	P1	Rh1	112.66(11)	C18	C17	P1	109.3(2)
C9	P1	C1	107.80(15)	C19	C18	C17	112.8(3)
C17	P1	Rh1	116.09(11)	C18	C19	P2	115.1(2)
C17	P1	C1	100.06(15)	C21	C20	P2	119.3(2)
C17	P1	C9	104.82(15)	C21	C20	C25	117.8(3)

C19	P2	Rh1	115.13(11)	C25	C20	P2	122.9(2)
C20	P2	Rh1	111.77(11)	C22	C21	C20	122.0(3)
C20	P2	C19	105.25(15)	C21	C22	C23	119.2(3)
C20	P2	C28	103.13(15)	C22	C23	C24	120.8(3)
C28	P2	Rh1	116.43(11)	C25	C24	C23	119.5(3)
C28	P2	C19	103.81(14)	O3	C25	C20	115.9(3)
C6	O1	C7	118.3(3)	O3	C25	C24	123.4(3)
C14	O2	C15	119.9(3)	C24	C25	C20	120.7(3)
C25	O3	C26	120.4(3)	O3	C26	C27	106.5(3)
C33	O4	C34	119.7(3)	C29	C28	P2	122.7(3)
C2	C1	P1	119.8(3)	C33	C28	P2	118.5(2)
C2	C1	C6	118.3(3)	C33	C28	C29	118.5(3)
C6	C1	P1	122.0(2)	C28	C29	C30	120.5(3)
C1	C2	C3	121.4(3)	C31	C30	C29	120.0(3)
C4	C3	C2	119.5(3)	C30	C31	C32	120.4(3)
C3	C4	C5	120.6(3)	C31	C32	C33	119.5(3)
C6	C5	C4	119.8(3)	O4	C33	C28	114.6(3)
O1	C6	C1	116.2(3)	O4	C33	C32	124.4(3)
O1	C6	C5	123.4(3)	C32	C33	C28	121.0(3)
C5	C6	C1	120.5(3)	O4	C34	C35	106.3(6)
O1	C7	C8	107.1(3)	O4	C34	C35A	103.6(18)
C10	C9	P1	118.7(3)	O5	C36	Rh1	176.6(4)
C14	C9	P1	121.4(3)				

Table A13. Torsion Angles for **1-I_{OEt}**.

A	B	C	D	Angle/°	A	B	C	D	Angle/°
Rh1	P1	C1	C2	-14.5(3)	C12	C13	C14	O2	179.5(3)
Rh1	P1	C1	C6	167.2(2)	C12	C13	C14	C9	-1.3(5)
Rh1	P1	C9	C10	91.5(3)	C14	O2	C15	C16	175.0(3)
Rh1	P1	C9	C14	-82.4(3)	C14	C9	C10	C11	-0.8(5)
Rh1	P1	C17	C18	47.1(2)	C15	O2	C14	C9	-177.8(3)
Rh1	P2	C19	C18	21.2(3)	C15	O2	C14	C13	1.4(5)
Rh1	P2	C20	C21	6.7(3)	C17	P1	C1	C2	110.3(3)
Rh1	P2	C20	C25	-171.5(2)	C17	P1	C1	C6	-68.0(3)
Rh1	P2	C28	C29	-111.7(3)	C17	P1	C9	C10	-35.6(3)
Rh1	P2	C28	C33	62.9(3)	C17	P1	C9	C14	150.5(3)
P1	C1	C2	C3	-179.5(2)	C17	C18	C19	P2	49.3(3)

P1	C1	C6	O1	0.3(4)	C19	P2	C20	C21	132.3(3)
P1	C1	C6	C5	-179.3(2)	C19	P2	C20	C25	-45.8(3)
P1	C9	C10	C11	-174.9(3)	C19	P2	C28	C29	120.6(3)
P1	C9	C14	O2	-5.7(4)	C19	P2	C28	C33	-64.8(3)
P1	C9	C14	C13	175.1(3)	C20	P2	C19	C18	-102.4(3)
P1	C17	C18	C19	-90.0(3)	C20	P2	C28	C29	11.0(3)
P2	C20	C21	C22	-176.6(3)	C20	P2	C28	C33	-174.4(3)
P2	C20	C25	O3	-5.9(4)	C20	C21	C22	C23	1.9(6)
P2	C20	C25	C24	174.6(3)	C21	C20	C25	O3	176.0(3)
P2	C28	C29	C30	175.4(3)	C21	C20	C25	C24	-3.6(5)
P2	C28	C33	O4	4.0(4)	C21	C22	C23	C24	-3.4(6)
P2	C28	C33	C32	-175.6(3)	C22	C23	C24	C25	1.5(6)
C1	P1	C9	C10	-141.5(3)	C23	C24	C25	O3	-177.4(3)
C1	P1	C9	C14	44.5(3)	C23	C24	C25	C20	2.1(5)
C1	P1	C17	C18	-76.3(2)	C25	O3	C26	C27	-175.2(3)
C1	C2	C3	C4	-0.6(5)	C25	C20	C21	C22	1.6(5)
C2	C1	C6	O1	-178.0(3)	C26	O3	C25	C20	172.0(3)
C2	C1	C6	C5	2.4(5)	C26	O3	C25	C24	-8.4(5)
C2	C3	C4	C5	1.0(5)	C28	P2	C19	C18	149.6(2)
C3	C4	C5	C6	0.3(5)	C28	P2	C20	C21	-119.2(3)
C4	C5	C6	O1	178.4(3)	C28	P2	C20	C25	62.7(3)
C4	C5	C6	C1	-2.0(5)	C28	C29	C30	C31	-0.2(5)
C6	O1	C7	C8	167.7(3)	C29	C28	C33	O4	178.8(3)
C6	C1	C2	C3	-1.1(5)	C29	C28	C33	C32	-0.7(5)
C7	O1	C6	C1	-161.3(3)	C29	C30	C31	C32	-0.5(5)
C7	O1	C6	C5	18.3(5)	C30	C31	C32	C33	0.6(5)
C9	P1	C1	C2	-140.5(3)	C31	C32	C33	O4	-179.5(3)
C9	P1	C1	C6	41.2(3)	C31	C32	C33	C28	0.0(5)
C9	P1	C17	C18	172.1(2)	C33	O4	C34	C35	173.2(10)
C9	C10	C11	C12	0.5(5)	C33	O4	C34	C35A	152(2)
C10	C9	C14	O2	-179.5(3)	C33	C28	C29	C30	0.8(5)
C10	C9	C14	C13	1.2(5)	C34	O4	C33	C28	-166.8(3)
C10	C11	C12	C13	-0.7(6)	C34	O4	C33	C32	12.7(5)
C11	C12	C13	C14	1.1(6)					

Table A14. Hydrogen Atom Coordinates (Å×10^4) and Isotropic Displacement Parameters (Å^2×10^3) for **1-I$_{OEt}$**.

Atom	*x*	*y*	*z*	U(eq)
H2	7872	3916	494	27
H3	7040	2805	-1019	33
H4	5095	1341	-1450	34
H5	3931	1000	-385	31
H7A	4278	588	1016	36
H7B	2658	999	708	36
H8A	2786	474	2023	51
H8B	2844	1706	2284	51
H8C	4425	1258	2575	51
H10	6260	4277	3826	35
H11	6566	3354	4910	44
H12	7649	1872	4693	43
H13	8412	1208	3398	43
H15A	8129	554	1844	44
H15B	9881	1223	2321	44
H16A	8057	916	447	59
H16B	9496	340	742	59
H16C	9808	1573	922	59
H17A	4382	4095	1864	24
H17B	5389	4994	2796	24
H18A	5755	5194	1119	25
H18B	4166	5457	1321	25
H19A	5496	6813	2611	23
H19B	6190	6954	1816	23
H21	9249	5652	4375	28
H22	8988	5751	5810	37
H23	7396	6838	6383	44
H24	6273	7949	5592	35
H26A	6012	9274	4892	31
H26B	4550	8329	4329	31
H27A	4385	8741	2969	55
H27B	5902	9644	3496	55
H27C	4298	9761	3735	55

H29	9736	8512	4470	28
H30	11198	10082	4564	33
H31	11509	10375	3245	36
H32	10397	9096	1816	34
H34A	10253	7331	822	43
H34B	8734	7827	469	43
H34C	10212	7577	851	43
H34D	8419	7623	332	43
H35A	8690	5661	213	72
H35B	8528	6192	-589	72
H35C	7164	6147	-122	72
H35D	9365	5743	574	85
H35E	9242	6034	-354	85
H35F	7697	5836	-64	85

Table A15. Atomic Occupancy for **1-I_{OEt}**.

Atom	***Occupancy***	**Atom**	***Occupancy***	**Atom**	***Occupancy***
H34A	0.73(5)	H34B	0.73(5)	H34C	0.27(5)
H34D	0.27(5)	C35	0.73(5)	H35A	0.73(5)
H35B	0.73(5)	H35C	0.73(5)	C35A	0.27(5)
H35D	0.27(5)	H35E	0.27(5)	H35F	0.27(5)
I1	0.9749(9)	I1A	0.0251(9)		

A.3.3. [RhHI2(CO)(dppp)], ***2-H***

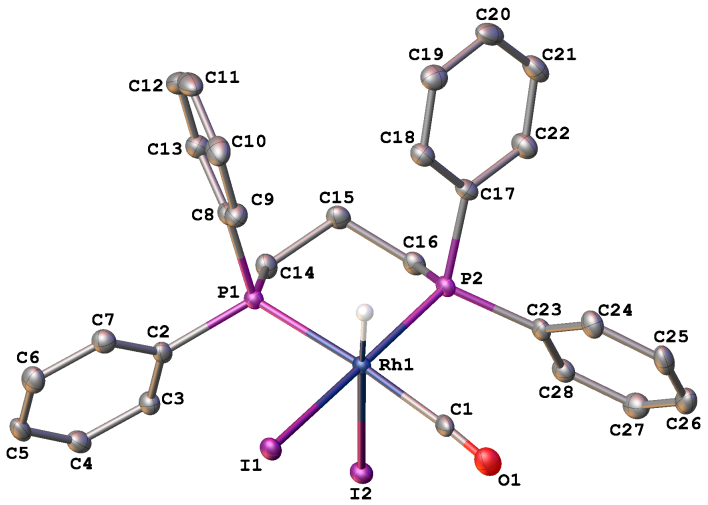

Figure A29. A molecular drawing of **2-H** shown with 50% probability ellipsoids. The solvent THF molecule and all H atoms except the hydride are omitted.

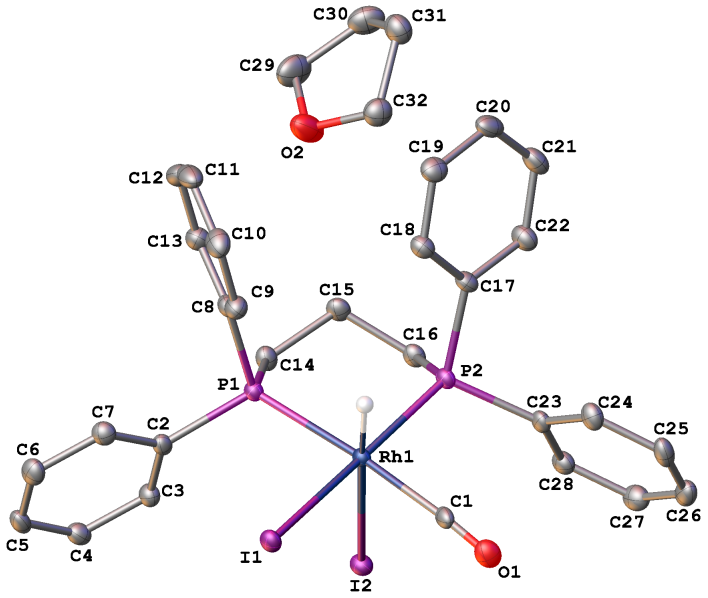

Figure A30. A molecular drawing of **2-H** shown with 50% probability ellipsoids. All H atoms except the hydride are omitted.

Table A16. Crystal data and structure refinement for **2-H**.

Empirical formula	$C_{28}H_{27}I_2OP_2Rh$. C_4H_8O
Formula weight	870.25
Temperature/K	99.98
Crystal system	monoclinic
Space group	$P2_1/n$
a/Å	10.0661(6)
b/Å	20.348(2)
c/Å	15.4681(8)
α/°	90
β/°	98.308(4)
γ/°	90
Volume/Å^3	3135.0(4)
Z	4
ρ_{calc}mg/mm^3	1.844
m/mm^{-1}	21.049
F(000)	1696.0
Crystal size/mm^3	0.238 × 0.129 × 0.098
Radiation	CuKα (λ = 1.54178)
2Θ range for data collection	7.226 to 144.56°
Index ranges	$-12 \leq h \leq 12$, $-21 \leq k \leq 24$, $-19 \leq l \leq 19$
Reflections collected	52989
Independent reflections	6150 [R_{int} = 0.0290, R_{sigma} = 0.0142]
Data/restraints/parameters	6150/0/356
Goodness-of-fit on F^2	1.103
Final R indexes [I>=2σ (I)]	R_1 = 0.0194, wR_2 = 0.0458
Final R indexes [all data]	R_1 = 0.0202, wR_2 = 0.0461
Largest diff. peak/hole / e Å^{-3}	0.68/-0.77

Table A17. Fractional Atomic Coordinates (×10^4) and Equivalent Isotropic Displacement Parameters (Å2×103) for **2-H**. Ueq is defined as 1/3 of of the trace of the orthogonalised UIJ tensor.

Atom	***x***	***y***	***z***	**U(eq)**
I1	1373.9(2)	5530.4(2)	7627.0(2)	12.83(4)
I2	4285.1(2)	4536.8(2)	6524.2(2)	13.16(4)
Rh1	4020.8(2)	5684.4(2)	7481.2(2)	8.53(5)
P1	3481.9(6)	6326.7(3)	6227.7(4)	9.95(11)

P2	6263.9(6)	5908.5(3)	7552.3(4)	10.28(11)
O1	4342.7(18)	4844(1)	9122.3(12)	20.8(4)
C1	4270(2)	5151.3(12)	8546.0(17)	14.7(5)
C2	1949(2)	6122.5(12)	5488.3(15)	12.2(5)
C3	1938(3)	5601.2(12)	4905.5(16)	14.6(5)
C4	788(3)	5459.1(12)	4322.5(16)	16.5(5)
C5	-358(3)	5838.8(13)	4310.8(16)	17.4(5)
C6	-361(3)	6355.2(13)	4898.4(17)	18.3(5)
C7	786(2)	6497.8(13)	5485.7(16)	15.9(5)
C8	3265(2)	7196.5(12)	6453.0(15)	13.7(5)
C9	2676(3)	7380.2(13)	7185.9(16)	16.7(5)
C10	2521(3)	8035.6(14)	7383.0(18)	22.3(6)
C11	2928(3)	8521.6(14)	6852(2)	24.7(6)
C12	3470(3)	8346.0(14)	6119.3(19)	24.1(6)
C13	3651(3)	7691.2(13)	5914.2(17)	18.7(5)
C14	4741(2)	6280.1(13)	5490.8(15)	14.6(5)
C15	6193(2)	6432.1(13)	5878.8(16)	15.0(5)
C16	6857(2)	5896.5(12)	6490.4(15)	13.5(5)
C17	6914(2)	6700.6(12)	7984.0(15)	13.1(5)
C18	6087(3)	7229.6(13)	8106.4(15)	15.4(5)
C19	6629(3)	7845.7(13)	8322.3(16)	18.8(5)
C20	8004(3)	7939.7(14)	8412.0(16)	21.1(6)
C21	8843(3)	7411.8(14)	8320.6(17)	21.7(6)
C22	8310(3)	6794.9(14)	8105.9(17)	19.2(5)
C23	7292(2)	5320.0(12)	8231.0(15)	12.9(5)
C24	7466(2)	5403.6(13)	9141.2(17)	17.0(5)
C25	8184(3)	4946.0(14)	9682.5(16)	19.8(5)
C26	8746(3)	4402.6(14)	9324.4(18)	21.3(6)
C27	8588(3)	4319.5(14)	8427.9(18)	20.6(5)
C28	7856(2)	4774.3(13)	7878.2(16)	15.8(5)
O2	7469(2)	7777.1(12)	5186.9(13)	35.0(5)
C29	8207(4)	8095.1(16)	4586.3(19)	34.3(7)
C30	9558(3)	8294.9(16)	5090(2)	30.7(7)
C31	9218(3)	8367.0(15)	6013.3(19)	25.3(6)
C32	8183(3)	7832.1(14)	6050.6(17)	23.0(6)

Table A18. Anisotropic Displacement Parameters ($Å^2 \times 10^3$) for **2-H**. The Anisotropic displacement factor exponent takes the form: $-2\pi^2[h^2a^{*2}U_{11}+2hka^*b^*U_{12}+\ldots]$.

Atom	U_{11}	U_{22}	U_{33}	U_{23}	U_{13}	U_{12}
I1	9.05(8)	15.11(8)	14.55(8)	0.52(5)	2.47(5)	-0.68(5)
I2	12.74(8)	11.63(8)	15.18(8)	-2.91(5)	2.24(6)	0.12(5)
Rh1	7.57(8)	8.71(9)	9.29(8)	-0.56(6)	1.18(6)	-0.15(6)
P1	9.6(3)	10.1(3)	10.1(3)	-0.3(2)	1.1(2)	-0.3(2)
P2	7.9(3)	11.5(3)	11.5(3)	-1.4(2)	1.5(2)	-0.1(2)
O1	19.4(9)	26.8(11)	16.6(9)	1.8(8)	3.7(7)	-3.5(8)
C1	9.1(11)	11.4(12)	22.1(13)	-2.8(10)	-3.2(9)	1.4(9)
C2	12.0(11)	14.2(12)	10.1(10)	2.4(9)	0.1(9)	-2.5(9)
C3	12.6(12)	14.4(13)	16.2(12)	0.3(9)	-0.2(9)	0.6(9)
C4	18.6(13)	16.2(13)	14.2(12)	-0.8(9)	0.9(10)	-4.3(10)
C5	12.9(12)	21.5(14)	16.3(12)	3.9(10)	-2.6(9)	-6.4(10)
C6	11.7(12)	22.0(14)	21.2(13)	2.6(10)	2.7(10)	1.1(10)
C7	14.8(12)	16.6(13)	16.6(12)	0.1(9)	3.4(9)	-0.3(9)
C8	12.1(11)	12.0(12)	15.5(11)	-2.3(9)	-2.8(9)	0.9(9)
C9	17.2(12)	13.7(13)	18.3(12)	-0.4(9)	-0.4(10)	1.6(10)
C10	20.1(14)	19.6(14)	25.8(14)	-5.0(11)	-1.8(11)	6.1(11)
C11	20.0(14)	12.4(14)	38.7(16)	-3.8(11)	-6.1(12)	0.4(10)
C12	20.4(14)	16.8(14)	33.5(15)	7.6(11)	-2.0(11)	-4.3(11)
C13	18.4(13)	16.6(14)	20.3(12)	1.8(10)	0.1(10)	-2.7(10)
C14	13.8(12)	18.5(13)	11.4(11)	1.1(9)	1.4(9)	-0.4(9)
C15	12.9(12)	18.2(13)	14.8(11)	1.5(9)	4.7(9)	-2.7(9)
C16	10.2(11)	17.1(13)	13.6(11)	-0.6(9)	3.3(9)	-1.1(9)
C17	13.7(12)	13.7(12)	11.5(10)	-3.0(9)	1.0(9)	-3.6(9)
C18	14.8(12)	16.1(13)	15.4(11)	-2.2(9)	2.2(9)	-2.3(10)
C19	24.5(14)	17.0(13)	14.8(12)	-3.5(9)	2.4(10)	-1.1(10)
C20	29.1(15)	18.3(14)	14.7(12)	-1.7(10)	-1(1)	-9.9(11)
C21	15.7(13)	27.8(16)	20.8(13)	-2.0(11)	0.2(10)	-7.8(11)
C22	14.7(12)	20.4(14)	22.2(13)	-3(1)	2.2(10)	-1.5(10)
C23	7.3(11)	15.4(13)	15.4(11)	1.5(9)	-0.4(9)	-0.9(9)
C24	11.5(12)	22.2(14)	17.1(12)	-1.8(10)	1.6(9)	1.4(10)
C25	12.7(12)	30.5(16)	15.2(12)	3.9(10)	-1.8(9)	-2.3(10)
C26	12.6(13)	22.4(14)	27.6(14)	8.7(11)	-1.2(10)	0.4(10)
C27	15.6(13)	18.2(14)	28.1(14)	-1.4(11)	3.6(11)	1.7(10)
C28	11.8(12)	16.2(13)	18.9(12)	-1.1(9)	1.1(9)	-0.7(9)
O2	41.3(13)	38.1(13)	23.5(10)	5.2(9)	-2.6(9)	-19.5(10)
C29	53(2)	31.0(18)	18.3(14)	5.3(12)	4.4(13)	-4.3(15)

C30	37.7(18)	26.0(16)	31.1(16)	4.6(12)	14.7(13)	-3.8(13)
C31	19.8(14)	29.3(16)	26.3(14)	0.2(12)	1.5(11)	-1.3(11)
C32	26.7(15)	23.5(15)	19.2(13)	1.6(10)	4.7(11)	-0.5(11)

Table A19. Bond Lengths for **2-H**

Atom	Atom	Length/Å	Atom	Atom	Length/Å
I1	Rh1	2.7243(3)	C11	C12	1.374(4)
I2	Rh1	2.7980(3)	C12	C13	1.388(4)
Rh1	P1	2.3363(6)	C14	C15	1.529(3)
Rh1	P2	2.2905(6)	C15	C16	1.532(3)
Rh1	C1	1.958(3)	C17	C18	1.390(4)
P1	C2	1.830(2)	C17	C22	1.404(4)
P1	C8	1.823(3)	C18	C19	1.388(4)
P1	C14	1.825(2)	C19	C20	1.385(4)
P2	C16	1.827(2)	C20	C21	1.386(4)
P2	C17	1.829(2)	C21	C22	1.387(4)
P2	C23	1.815(2)	C23	C24	1.404(3)
O1	C1	1.083(3)	C23	C28	1.394(4)
C2	C3	1.391(3)	C24	C25	1.384(4)
C2	C7	1.398(3)	C25	C26	1.393(4)
C3	C4	1.391(4)	C26	C27	1.383(4)
C4	C5	1.386(4)	C27	C28	1.393(4)
C5	C6	1.390(4)	O2	C29	1.426(4)
C6	C7	1.392(4)	O2	C32	1.427(3)
C8	C9	1.404(3)	C29	C30	1.522(5)
C8	C13	1.397(4)	C30	C31	1.523(4)
C9	C10	1.382(4)	C31	C32	1.514(4)
C10	C11	1.385(4)			

Table A20. Bond Angles for **2-H**

Atom	Atom	Atom	Angle/°	Atom	Atom	Atom	Angle/°
I1	Rh1	I2	96.702(8)	C13	C8	P1	122.28(19)
P1	Rh1	I1	91.171(16)	C13	C8	C9	118.4(2)
P1	Rh1	I2	93.223(16)	C10	C9	C8	120.6(2)
P2	Rh1	I1	171.128(16)	C9	C10	C11	120.4(3)
P2	Rh1	I2	91.324(16)	C12	C11	C10	119.4(3)
P2	Rh1	P1	92.15(2)	C11	C12	C13	121.3(3)
C1	Rh1	I1	82.78(7)	C12	C13	C8	119.9(3)
C1	Rh1	I2	88.41(7)	C15	C14	P1	117.05(16)
C1	Rh1	P1	173.89(7)	C14	C15	C16	113.9(2)

C1	Rh1	P2	93.70(7)	C15	C16	P2	112.07(17)
C2	P1	Rh1	117.72(8)	C18	C17	P2	122.85(19)
C8	P1	Rh1	113.85(8)	C18	C17	C22	118.9(2)
C8	P1	C2	103.08(11)	C22	C17	P2	117.88(19)
C8	P1	C14	106.45(12)	C19	C18	C17	120.6(2)
C14	P1	Rh1	112.97(8)	C20	C19	C18	120.1(3)
C14	P1	C2	101.33(11)	C19	C20	C21	119.8(2)
C16	P2	Rh1	113.70(8)	C20	C21	C22	120.4(2)
C16	P2	C17	101.18(11)	C21	C22	C17	120.1(2)
C17	P2	Rh1	119.41(8)	C24	C23	P2	118.59(19)
C23	P2	Rh1	111.85(8)	C28	C23	P2	121.98(18)
C23	P2	C16	106.16(11)	C28	C23	C24	119.4(2)
C23	P2	C17	103.08(11)	C25	C24	C23	120.3(2)
O1	C1	Rh1	176.3(2)	C24	C25	C26	120.0(2)
C3	C2	P1	120.35(19)	C27	C26	C25	120.1(2)
C3	C2	C7	119.1(2)	C26	C27	C28	120.3(3)
C7	C2	P1	120.53(19)	C27	C28	C23	120.0(2)
C2	C3	C4	120.4(2)	C29	O2	C32	109.6(2)
C5	C4	C3	120.4(2)	O2	C29	C30	107.4(2)
C4	C5	C6	119.6(2)	C29	C30	C31	101.6(2)
C5	C6	C7	120.3(2)	C32	C31	C30	102.4(2)
C6	C7	C2	120.2(2)	O2	C32	C31	106.1(2)
C9	C8	P1	119.29(19)				

Table A21. Torsion Angles for **2-H**

A	B	C	D	Angle/°	A	B	C	D	Angle/°
Rh1	P1	C2	C3	-79.1(2)	C11	C12	C13	C8	0.7(4)
Rh1	P1	C2	C7	102.55(19)	C13	C8	C9	C10	-2.0(4)
Rh1	P1	C8	C9	-36.1(2)	C14	P1	C2	C3	44.6(2)
Rh1	P1	C8	C13	144.68(18)	C14	P1	C2	C7	-133.7(2)
Rh1	P1	C14	C15	-53.8(2)	C14	P1	C8	C9	-161.24(19)
Rh1	P2	C16	C15	63.53(18)	C14	P1	C8	C13	19.6(2)
Rh1	P2	C17	C18	-13.7(2)	C14	C15	C16	P2	-75.3(2)
Rh1	P2	C17	C22	173.31(16)	C16	P2	C17	C18	111.9(2)
Rh1	P2	C23	C24	-81.1(2)	C16	P2	C17	C22	-61.1(2)
Rh1	P2	C23	C28	95.8(2)	C16	P2	C23	C24	154.4(2)
P1	C2	C3	C4	-177.81(19)	C16	P2	C23	C28	-28.7(2)
P1	C2	C7	C6	177.54(19)	C17	P2	C16	C15	-65.77(19)
P1	C8	C9	C10	178.8(2)	C17	P2	C23	C24	48.4(2)
P1	C8	C13	C12	-179.6(2)	C17	P2	C23	C28	-134.7(2)
P1	C14	C15	C16	71.9(3)	C17	C18	C19	C20	0.4(4)

P2	C17	C18	C19	-171.20(19)	C18	C17	C22	C21	-1.8(4)
P2	C17	C22	C21	171.5(2)	C18	C19	C20	C21	-2.6(4)
P2	C23	C24	C25	176.6(2)	C19	C20	C21	C22	2.5(4)
P2	C23	C28	C27	-177.1(2)	C20	C21	C22	C17	-0.3(4)
C2	P1	C8	C9	92.6(2)	C22	C17	C18	C19	1.7(4)
C2	P1	C8	C13	-86.6(2)	C23	P2	C16	C15	-173.07(17)
C2	P1	C14	C15	179.31(19)	C23	P2	C17	C18	-138.4(2)
C2	C3	C4	C5	0.5(4)	C23	P2	C17	C22	48.6(2)
C3	C2	C7	C6	-0.8(4)	C23	C24	C25	C26	0.5(4)
C3	C4	C5	C6	-1.3(4)	C24	C23	C28	C27	-0.2(4)
C4	C5	C6	C7	1.1(4)	C24	C25	C26	C27	0.0(4)
C5	C6	C7	C2	0.0(4)	C25	C26	C27	C28	-0.7(4)
C7	C2	C3	C4	0.6(4)	C26	C27	C28	C23	0.7(4)
C8	P1	C2	C3	154.7(2)	C28	C23	C24	C25	-0.4(4)
C8	P1	C2	C7	-23.7(2)	O2	C29	C30	C31	-26.6(3)
C8	P1	C14	C15	71.9(2)	C29	O2	C32	C31	16.0(3)
C8	C9	C10	C11	1.0(4)	C29	C30	C31	C32	34.8(3)
C9	C8	C13	C12	1.2(4)	C30	C31	C32	O2	-32.2(3)
C9	C10	C11	C12	0.9(4)	C32	O2	C29	C30	7.0(3)
C10	C11	C12	C13	-1.8(4)					

Table A22. Hydrogen Atom Coordinates ($Å \times 10^4$) and Isotropic Displacement Parameters ($Å^2 \times 10^3$) for **2-H**

Atom	***x***	***y***	***z***	**U(eq)**
H	3900(40)	6264(18)	8010(20)	37(10)
H3	2721	5341	4906	18
H4	788	5100	3930	20
H5	-1136	5747	3904	21
H6	-1149	6612	4900	22
H7	777	6851	5886	19
H9	2380	7051	7550	20
H10	2133	8154	7886	27
H11	2834	8972	6993	30
H12	3725	8679	5746	29
H13	4036	7580	5408	22
H14A	4714	5831	5241	18
H14B	4475	6588	5001	18
H15A	6212	6851	6206	18
H15B	6727	6494	5395	18
H16A	7842	5960	6576	16

H16B	6662	5461	6215	16
H18	5142	7169	8042	19
H19	6055	8203	8409	23
H20	8372	8365	8536	25
H21	9788	7473	8406	26
H22	8890	6436	8041	23
H24	7090	5776	9387	20
H25	8294	5003	10298	24
H26	9238	4089	9696	26
H27	8981	3951	8186	25
H28	7741	4712	7263	19
H29A	7715	8488	4333	41
H29B	8337	7792	4105	41
H30A	9878	8715	4871	37
H30B	10245	7951	5060	37
H31A	10019	8294	6456	30
H31B	8840	8807	6104	30
H32A	8626	7411	6238	28
H32B	7564	7951	6468	28

A.3.4. [RhI(CH$_3$)(dpppOEt)]BF$_4$, ***[8$_{OEt}$]BF$_4$***

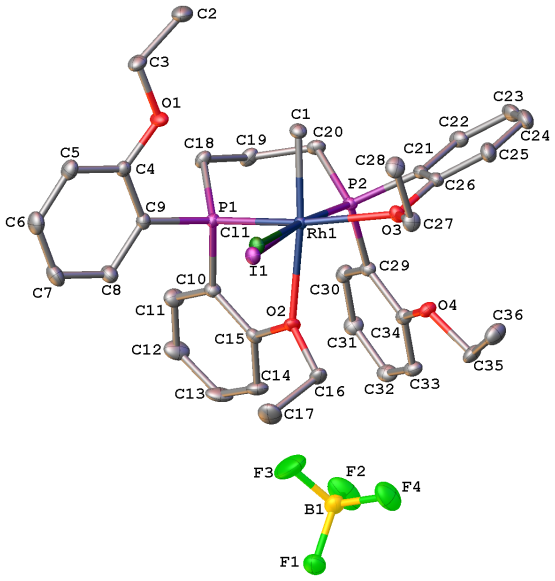

Figure A31. A molecular drawing of **[8$_{OEt}$]BF$_4$** shown with 50% probability ellipsoids. All H atoms are omitted, but both disordered atoms (I1 and Cl1) are shown. The major disorder component, I1 is present 72.51(17)% of the time.

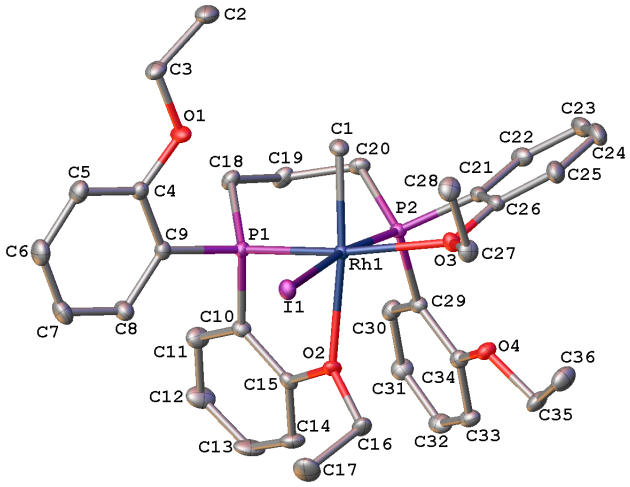

Figure A32. A molecular drawing of the Rh cation of **[8$_{OEt}$]BF$_4$** shown with 50% probability ellipsoids. All H atoms, anion, and minor component of the compositional disorder are omitted.

Table A23. Crystal data and structure refinement for **[8_{OEt}]BF_4**

Empirical formula	$C_{36}H_{45}BCl_{0.27485}F_4I_{0.72515}O_4P_2Rh$
Formula weight	895.14
Temperature/K	100.0
Crystal system	orthorhombic
Space group	Fdd2
a/Å	32.999(10)
b/Å	45.313(14)
c/Å	9.645(4)
α/°	90
β/°	90
γ/°	90
Volume/Å^3	14422(8)
Z	16
ρ_{calc}mg/mm^3	1.649
m/mm^{-1}	1.263
F(000)	7234.0
Crystal size/mm^3	0.447 × 0.081 × 0.078
Radiation	MoKα (λ = 0.71073)
2Θ range for data collection	3.054 to 61.042°
Index ranges	$-47 \leq h \leq 46$, $-64 \leq k \leq 64$, $-13 \leq l \leq 13$
Reflections collected	102613
Independent reflections	11027 [R_{int} = 0.0315, R_{sigma} = 0.0171]
Data/restraints/parameters	11027/1/452
Goodness-of-fit on F^2	1.068
Final R indexes [I>=2σ (I)]	R_1 = 0.0198, wR_2 = 0.0474
Final R indexes [all data]	R_1 = 0.0206, wR_2 = 0.0478
Largest diff. peak/hole / e Å^{-3}	0.49/-0.40
Flack parameter	-0.006(11)

Table A24. Fractional Atomic Coordinates ($\times 10^4$) and Equivalent Isotropic Displacement Parameters ($Å^2 \times 10^3$) for **[8$_{OEt}$]BF$_4$**. U_{eq} is defined as 1/3 of of the trace of the orthogonalised U_{IJ} tensor.

Atom	*x*	*y*	*z*	U(eq)
Rh1	6400.9(2)	4351.5(2)	2509.7(2)	9.25(4)
I1	7203.4(2)	4357.5(2)	3067.0(3)	12.80(8)
Cl1	7129.6(13)	4367.7(11)	2865(5)	12.80(8)
P1	6302.6(2)	4813.5(2)	3103.4(7)	10.55(10)
P2	5737.4(2)	4285.0(2)	2170.5(6)	10.37(11)
O1	6796.6(5)	5083.7(4)	903.5(19)	16.8(4)
O2	6304.6(5)	4294.1(4)	4895.0(18)	13.3(3)
O3	6403.5(5)	3880.3(4)	1672.9(19)	13.4(3)
O4	5818.0(6)	3753.4(4)	3956.5(19)	14.0(3)
C1	6465.9(7)	4456.7(5)	446(3)	14.5(4)
C2	6738.7(10)	5109.2(7)	-1553(3)	25.0(6)
C3	6970.4(8)	5217.9(6)	-308(3)	18.5(5)
C4	6938.7(7)	5168.9(5)	2161(3)	13.1(4)
C5	7270.3(8)	5356.7(6)	2338(3)	18.6(5)
C6	7392.7(9)	5430.8(6)	3670(3)	22.0(5)
C7	7198.2(9)	5318.1(6)	4826(3)	23.3(5)
C8	6869.3(8)	5129.6(6)	4642(3)	17.7(5)
C9	6732.9(7)	5056.5(5)	3321(3)	13.4(4)
C10	6068.7(7)	4787.9(5)	4797(2)	13.2(4)
C11	5849.9(8)	5022.0(6)	5368(3)	19.5(5)
C12	5656.4(9)	4992.0(7)	6634(3)	25.2(6)
C13	5676.4(9)	4722.2(7)	7319(3)	24.6(6)
C14	5898.7(8)	4487.8(6)	6796(3)	18.8(5)
C15	6094.1(6)	4521.0(5)	5531(2)	12.5(4)
C16	6476.5(8)	4062.0(5)	5761(3)	16.6(5)
C17	6796.4(9)	4180.7(7)	6725(3)	26.1(6)
C18	5947.5(7)	5019.9(5)	2031(3)	14.2(4)
C19	5519.5(7)	4895.6(5)	1940(3)	15.8(5)
C20	5471.2(7)	4585.1(5)	1304(3)	14.8(4)
C21	5724.4(7)	3975.1(5)	1000(2)	13.1(4)
C22	5379.3(8)	3905.4(6)	228(3)	17.7(5)
C23	5387.2(9)	3674.2(7)	-712(3)	22.3(5)
C24	5740.0(9)	3512.4(6)	-882(3)	23.0(6)
C25	6086.2(8)	3574.4(6)	-112(3)	19.7(5)
C26	6076.0(7)	3804.5(6)	846(3)	14.2(4)

C27	6779.5(8)	3709.5(6)	1516(3)	16.4(5)
C28	7023.9(8)	3798.2(6)	265(3)	20.6(5)
C29	5437.4(7)	4190.1(5)	3683(2)	12.6(4)
C30	5125.0(8)	4375.0(5)	4143(3)	16.0(5)
C31	4916.1(8)	4317.2(6)	5362(3)	18.1(5)
C32	5013.2(8)	4070.1(6)	6137(3)	18.4(5)
C33	5310.8(8)	3876.1(6)	5682(3)	16.5(4)
C34	5522.5(7)	3934.0(5)	4457(3)	13.4(4)
C35	5866.0(8)	3467.8(5)	4616(3)	18.6(5)
C36	6185.2(9)	3300.5(6)	3823(3)	23.6(6)
F1	4462.1(6)	4333.7(4)	11216.7(19)	27.1(4)
F2	3927.5(7)	4397.5(5)	9773(3)	46.8(6)
F3	4557.0(9)	4549.4(6)	9152(3)	64.1(8)
F4	4409.7(7)	4062.8(5)	9242(2)	39.1(5)
B1	4337.2(10)	4336.7(7)	9825(3)	22.0(6)

Table A25. Anisotropic Displacement Parameters ($Å^2 \times 10^3$) for **[8$_{OEt}$]BF$_4$**. The Anisotropic displacement factor exponent takes the form: $-2\pi^2[h^2a^{*2}U_{11}+2hka^*b^*U_{12}+\ldots]$.

Atom	U_{11}	U_{22}	U_{33}	U_{23}	U_{13}	U_{12}
Rh1	7.88(8)	10.10(8)	9.77(7)	-0.29(6)	-0.15(6)	0.02(6)
I1	7.40(16)	14.46(10)	16.53(15)	-1.59(10)	-0.06(9)	-0.56(11)
Cl1	7.40(16)	14.46(10)	16.53(15)	-1.59(10)	-0.06(9)	-0.56(11)
P1	10.3(2)	10.4(2)	10.9(2)	-0.1(2)	0.7(2)	0.08(19)
P2	9.0(2)	12.6(2)	9.6(2)	0.72(19)	-0.83(19)	-0.3(2)
O1	16.8(9)	21.7(9)	11.8(8)	2.3(6)	1.7(7)	-6.0(7)
O2	15.3(8)	13.4(7)	11.3(7)	1.7(6)	-2.9(6)	2.4(6)
O3	11.4(8)	14.3(8)	14.6(8)	-3.0(6)	-1.4(6)	0.8(6)
O4	14.7(8)	13.0(8)	14.4(8)	3.4(6)	1.7(6)	1.1(6)
C1	15.3(10)	17.3(11)	11.0(9)	-0.6(8)	2.2(8)	-1.2(8)
C2	36.5(16)	24.2(14)	14.4(12)	2.7(10)	2.0(11)	-3.0(12)
C3	22.3(12)	17.8(11)	15.3(11)	2.9(9)	6.2(9)	-1.6(9)
C4	13(1)	11.7(10)	14.6(10)	0.9(8)	-1.6(8)	0.1(8)
C5	15.1(11)	16.9(11)	23.9(13)	2.1(10)	-0.4(9)	-3.3(9)
C6	17.7(12)	19.9(12)	28.4(14)	-3.0(11)	-2.8(10)	-5.1(10)
C7	23.9(13)	24.2(13)	21.9(13)	-7.5(10)	-4.6(10)	-3.7(10)
C8	18.6(12)	19.6(12)	14.9(11)	-2.2(9)	0.8(9)	-3.2(9)
C9	13(1)	11.5(10)	15.6(11)	-0.9(8)	-0.6(8)	-0.6(8)
C10	12.5(10)	15.8(10)	11.3(11)	-0.6(8)	1.4(8)	0.0(8)
C11	21.7(12)	19.0(11)	17.8(12)	-1.3(9)	3.5(9)	5.1(10)
C12	27.1(14)	30.6(15)	17.8(12)	-3.3(11)	5.3(10)	10.8(12)

C13	26.2(13)	37.9(16)	9.8(11)	0.7(10)	5.1(9)	8.7(12)
C14	20.7(12)	24.5(13)	11.3(10)	4.7(9)	1.0(9)	2.4(10)
C15	11.3(10)	15.2(10)	11.1(9)	-2.7(8)	-1.9(8)	0.6(7)
C16	17.4(11)	14.8(10)	17.5(11)	4.3(9)	-5.4(9)	0.4(9)
C17	23.0(14)	29.6(15)	25.7(14)	2.4(11)	-12.6(11)	4.1(11)
C18	12.1(10)	12.2(10)	18.4(10)	3.4(8)	-0.3(8)	0.8(8)
C19	10.5(10)	15.2(11)	21.7(12)	5.3(9)	0.1(9)	1.7(8)
C20	12(1)	18.7(11)	13.8(10)	3.8(9)	-2.4(8)	1.2(8)
C21	14.7(10)	14.6(10)	9.9(9)	0.8(8)	-0.9(8)	-4.0(8)
C22	14.7(11)	22.6(12)	16.0(12)	3.0(9)	-2.2(8)	-4.6(9)
C23	24.2(13)	26.8(14)	15.9(12)	-0.8(10)	-4.7(10)	-10.2(11)
C24	30.3(15)	21.7(13)	17.1(11)	-5.6(10)	0.2(10)	-9.5(11)
C25	24.7(12)	16.4(11)	18.1(12)	-4.7(10)	1.9(10)	-3.1(9)
C26	17.1(11)	14.8(10)	10.7(10)	0.1(8)	-0.6(8)	-3.1(8)
C27	13.9(11)	14.6(11)	20.8(11)	-1.5(9)	1.1(9)	4.3(9)
C28	19.3(12)	19.8(12)	22.8(13)	-3.3(9)	5.6(9)	1.9(9)
C29	11(1)	15.3(11)	11.5(10)	0.4(8)	0.3(8)	-1.9(8)
C30	13.8(11)	15.2(11)	19.1(11)	2.0(9)	0.6(9)	-0.7(9)
C31	13.8(11)	21.0(12)	19.7(12)	0.1(9)	3.2(9)	0.4(9)
C32	14.5(11)	25.0(13)	15.6(11)	1.1(10)	3.3(9)	-2.2(9)
C33	16.0(11)	19.3(11)	14.2(11)	4.1(9)	-0.1(9)	-1.9(9)
C34	11(1)	15.0(11)	14.2(10)	0.9(8)	-1.1(8)	-0.8(8)
C35	21.5(12)	13.5(10)	20.7(11)	6.2(9)	2.6(9)	0.2(9)
C36	26.7(14)	16.4(12)	27.7(14)	3.8(10)	6.4(11)	5.3(10)
F1	30.5(10)	26.5(9)	24.2(9)	1.0(7)	-8.1(7)	1.4(7)
F2	30.7(11)	60.1(14)	49.7(15)	-20.0(12)	-16.1(10)	21.9(10)
F3	84(2)	60.8(16)	47.1(14)	31.6(13)	-11.1(14)	-34.7(15)
F4	44.7(12)	34.8(11)	38.0(11)	-15.2(9)	-6.6(9)	12.0(9)
B1	23.9(15)	19.3(14)	22.7(14)	2.8(11)	-5.1(12)	1.2(11)

Table A26. Bond Lengths for **[8_{OEt}]BF_4.**

Atom	Atom	Length/Å	Atom	Atom	Length/Å
Rh1	I1	2.7021(9)	C10	C11	1.397(3)
Rh1	Cl1	2.430(4)	C10	C15	1.404(3)
Rh1	P1	2.1943(8)	C11	C12	1.385(4)
Rh1	P2	2.2343(9)	C12	C13	1.391(4)
Rh1	O2	2.337(2)	C13	C14	1.386(4)
Rh1	O3	2.2828(18)	C14	C15	1.388(3)
Rh1	C1	2.058(3)	C16	C17	1.506(4)
P1	C9	1.809(3)	C18	C19	1.523(3)
P1	C10	1.810(2)	C19	C20	1.544(4)

P1	C18	1.822(3)	C21	C22	1.397(3)
P2	C20	1.822(2)	C21	C26	1.402(4)
P2	C21	1.802(3)	C22	C23	1.386(4)
P2	C29	1.815(3)	C23	C24	1.385(4)
O1	C3	1.436(3)	C24	C25	1.391(4)
O1	C4	1.356(3)	C25	C26	1.393(3)
O2	C15	1.384(3)	C27	C28	1.506(4)
O2	C16	1.458(3)	C29	C30	1.400(3)
O3	C26	1.386(3)	C29	C34	1.408(3)
O3	C27	1.470(3)	C30	C31	1.388(4)
O4	C34	1.362(3)	C31	C32	1.384(4)
O4	C35	1.451(3)	C32	C33	1.389(4)
C2	C3	1.506(4)	C33	C34	1.397(3)
C4	C5	1.397(3)	C35	C36	1.507(4)
C4	C9	1.404(3)	F1	B1	1.404(4)
C5	C6	1.388(4)	F2	B1	1.381(4)
C6	C7	1.383(4)	F3	B1	1.370(4)
C7	C8	1.392(4)	F4	B1	1.384(4)
C8	C9	1.392(3)			

Table A27. Bond Angles for **[8_{OEt}]BF_4**.

Atom	Atom	Atom	Angle/°	Atom	Atom	Atom	Angle/°
P1	Rh1	I1	94.779(19)	C9	C8	C7	121.0(2)
P1	Rh1	Cl1	94.63(11)	C4	C9	P1	120.54(18)
P1	Rh1	P2	91.26(2)	C8	C9	P1	120.33(19)
P1	Rh1	O2	80.16(5)	C8	C9	C4	119.1(2)
P1	Rh1	O3	170.11(5)	C11	C10	P1	121.87(19)
P2	Rh1	I1	172.241(19)	C11	C10	C15	119.1(2)
P2	Rh1	Cl1	173.96(12)	C15	C10	P1	118.99(18)
P2	Rh1	O2	89.77(5)	C12	C11	C10	120.8(3)
P2	Rh1	O3	79.96(5)	C11	C12	C13	118.9(3)
O2	Rh1	I1	86.48(4)	C14	C13	C12	121.7(2)
O2	Rh1	Cl1	89.94(12)	C13	C14	C15	118.9(2)
O3	Rh1	I1	94.37(4)	O2	C15	C10	116.5(2)
O3	Rh1	Cl1	94.27(12)	O2	C15	C14	122.8(2)
O3	Rh1	O2	104.15(6)	C14	C15	C10	120.6(2)
C1	Rh1	I1	95.04(7)	O2	C16	C17	111.6(2)
C1	Rh1	Cl1	91.52(13)	C19	C18	P1	116.04(17)
C1	Rh1	P1	92.69(7)	C18	C19	C20	117.1(2)
C1	Rh1	P2	89.52(7)	C19	C20	P2	116.61(17)
C1	Rh1	O2	172.80(8)	C22	C21	P2	122.0(2)

C1	Rh1	O3	82.77(8)	C22	C21	C26	119.5(2)
C9	P1	Rh1	119.66(8)	C26	C21	P2	118.47(18)
C9	P1	C10	105.61(11)	C23	C22	C21	120.3(3)
C9	P1	C18	104.95(11)	C22	C23	C24	119.6(3)
C10	P1	Rh1	103.73(8)	C23	C24	C25	121.3(3)
C10	P1	C18	105.72(12)	C24	C25	C26	119.0(3)
C18	P1	Rh1	115.90(9)	O3	C26	C21	116.6(2)
C20	P2	Rh1	116.05(8)	O3	C26	C25	123.2(2)
C21	P2	Rh1	102.72(8)	C25	C26	C21	120.2(2)
C21	P2	C20	106.42(12)	O3	C27	C28	113.2(2)
C21	P2	C29	107.82(11)	C30	C29	P2	120.96(19)
C29	P2	Rh1	116.66(8)	C30	C29	C34	118.2(2)
C29	P2	C20	106.41(11)	C34	C29	P2	120.85(18)
C4	O1	C3	118.0(2)	C31	C30	C29	121.4(2)
C15	O2	Rh1	114.96(14)	C32	C31	C30	119.7(2)
C15	O2	C16	118.51(19)	C31	C32	C33	120.3(2)
C16	O2	Rh1	126.24(15)	C32	C33	C34	120.1(2)
C26	O3	Rh1	115.61(14)	O4	C34	C29	116.7(2)
C26	O3	C27	117.93(19)	O4	C34	C33	123.0(2)
C27	O3	Rh1	122.13(14)	C33	C34	C29	120.2(2)
C34	O4	C35	117.32(19)	O4	C35	C36	107.6(2)
O1	C3	C2	107.9(2)	F2	B1	F1	108.9(3)
O1	C4	C5	123.6(2)	F2	B1	F4	109.5(3)
O1	C4	C9	116.2(2)	F3	B1	F1	107.7(3)
C5	C4	C9	120.2(2)	F3	B1	F2	111.2(3)
C6	C5	C4	119.2(2)	F3	B1	F4	110.3(3)
C7	C6	C5	121.4(2)	F4	B1	F1	109.2(2)
C6	C7	C8	119.0(3)				

Table A28. Torsion Angles for **[8_{OEt}]BF_4**.

A	**B**	**C**	**D**	**Angle/°**	**A**	**B**	**C**	**D**	**Angle/°**
Rh1	P1	C9	C4	75.7(2)	C11	C10	C15	O2	178.1(2)
Rh1	P1	C9	C8	-103.0(2)	C11	C10	C15	C14	1.2(4)
Rh1	P1	C10	C11	-160.7(2)	C11	C12	C13	C14	2.8(5)
Rh1	P1	C10	C15	16.6(2)	C12	C13	C14	C15	-2.3(4)
Rh1	P1	C18	C19	58.5(2)	C13	C14	C15	O2	-176.5(2)
Rh1	P2	C20	C19	-53.4(2)	C13	C14	C15	C10	0.3(4)
Rh1	P2	C21	C22	-162.89(19)	C15	O2	C16	C17	-63.6(3)
Rh1	P2	C21	C26	15.6(2)	C15	C10	C11	C12	-0.7(4)
Rh1	P2	C29	C30	118.33(19)	C16	O2	C15	C10	156.4(2)
Rh1	P2	C29	C34	-59.3(2)	C16	O2	C15	C14	-26.7(3)

Rh1	O2	C15	C10	-17.8(2)	C18	P1	C9	C4	-56.6(2)
Rh1	O2	C15	C14	159.09(19)	C18	P1	C9	C8	124.8(2)
Rh1	O2	C16	C17	109.9(2)	C18	P1	C10	C11	-38.3(2)
Rh1	O3	C26	C21	-21.6(3)	C18	P1	C10	C15	139.05(19)
Rh1	O3	C26	C25	157.6(2)	C18	C19	C20	P2	59.7(3)
Rh1	O3	C27	C28	-77.1(2)	C20	P2	C21	C22	-40.5(2)
P1	C10	C11	C12	176.7(2)	C20	P2	C21	C26	138.03(19)
P1	C10	C15	O2	0.7(3)	C20	P2	C29	C30	-13.0(2)
P1	C10	C15	C14	-176.27(19)	C20	P2	C29	C34	169.41(19)
P1	C18	C19	C20	-62.0(3)	C21	P2	C20	C19	-166.92(18)
P2	C21	C22	C23	176.8(2)	C21	P2	C29	C30	-126.8(2)
P2	C21	C26	O3	3.3(3)	C21	P2	C29	C34	55.6(2)
P2	C21	C26	C25	-176.0(2)	C21	C22	C23	C24	-0.1(4)
P2	C29	C30	C31	-174.6(2)	C22	C21	C26	O3	-178.2(2)
P2	C29	C34	O4	-4.6(3)	C22	C21	C26	C25	2.6(4)
P2	C29	C34	C33	174.82(19)	C22	C23	C24	C25	1.0(4)
O1	C4	C5	C6	-180.0(2)	C23	C24	C25	C26	-0.1(4)
O1	C4	C9	P1	-0.2(3)	C24	C25	C26	O3	179.1(2)
O1	C4	C9	C8	178.5(2)	C24	C25	C26	C21	-1.7(4)
C3	O1	C4	C5	-6.6(4)	C26	O3	C27	C28	78.5(3)
C3	O1	C4	C9	173.5(2)	C26	C21	C22	C23	-1.7(4)
C4	O1	C3	C2	-174.9(2)	C27	O3	C26	C21	-178.8(2)
C4	C5	C6	C7	1.3(4)	C27	O3	C26	C25	0.5(3)
C5	C4	C9	P1	179.92(19)	C29	P2	C20	C19	78.3(2)
C5	C4	C9	C8	-1.4(4)	C29	P2	C21	C22	73.4(2)
C5	C6	C7	C8	-0.9(4)	C29	P2	C21	C26	-108.1(2)
C6	C7	C8	C9	-0.7(4)	C29	C30	C31	C32	-0.9(4)
C7	C8	C9	P1	-179.5(2)	C30	C29	C34	O4	177.7(2)
C7	C8	C9	C4	1.8(4)	C30	C29	C34	C33	-2.8(4)
C9	P1	C10	C11	72.6(2)	C30	C31	C32	C33	-1.7(4)
C9	P1	C10	C15	-110.03(19)	C31	C32	C33	C34	1.9(4)
C9	P1	C18	C19	-167.15(19)	C32	C33	C34	O4	179.9(2)
C9	C4	C5	C6	-0.1(4)	C32	C33	C34	C29	0.4(4)
C10	P1	C9	C4	-168.01(19)	C34	O4	C35	C36	175.7(2)
C10	P1	C9	C8	13.3(2)	C34	C29	C30	C31	3.1(4)
C10	P1	C18	C19	-55.8(2)	C35	O4	C34	C29	-170.6(2)
C10	C11	C12	C13	-1.3(4)	C35	O4	C34	C33	9.9(3)

Table A29. Hydrogen Atom Coordinates (Å×10^4) and Isotropic Displacement Parameters (Å^2×10^3) for **[8$_{OEt}$]BF$_4$**.

Atom	*x*	*y*	*z*	U(eq)
H1A	6748	4513	262	22
H1B	6287	4622	215	22
H1C	6394	4285	-124	22
H2A	6836	5211	-2385	38
H2B	6449	5149	-1425	38
H2C	6780	4896	-1658	38
H3A	7260	5163	-390	22
H3B	6951	5435	-242	22
H5	7411	5433	1556	22
H6	7615	5562	3792	26
H7	7288	5369	5731	28
H8	6736	5050	5430	21
H11	5834	5204	4883	23
H12	5512	5153	7029	30
H13	5534	4698	8168	30
H14	5917	4307	7294	23
H16A	6597	3908	5161	20
H16B	6258	3969	6312	20
H17A	7010	4277	6182	39
H17B	6913	4018	7261	39
H17C	6674	4325	7358	39
H18A	5931	5224	2395	17
H18B	6060	5032	1080	17
H19A	5353	5035	1390	19
H19B	5405	4891	2889	19
H20A	5565	4593	330	18
H20B	5179	4536	1286	18
H22	5138	4017	347	21
H23	5152	3627	-1236	27
H24	5746	3356	-1537	28
H25	6326	3462	-238	24
H27A	6711	3497	1443	20
H27B	6947	3736	2358	20
H28A	6861	3769	-574	31
H28B	7269	3677	213	31
H28C	7100	4007	343	31
H30	5055	4544	3609	19

H31	4707	4447	5664	22
H32	4876	4033	6984	22
H33	5370	3704	6205	20
H35A	5606	3358	4599	22
H35B	5950	3493	5593	22
H36A	6096	3273	2863	35
H36B	6228	3108	4258	35
H36C	6439	3412	3832	35

A.3.5. [RhI(CO)$_2$(dppp)], ***4-I***[4]

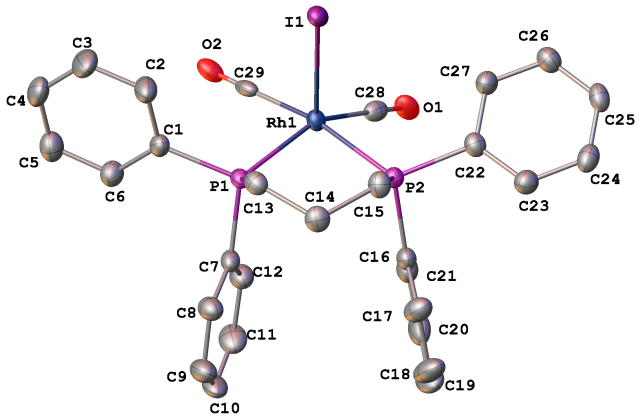

Figure A33. The rhodium complex of **4-I**. All atoms are drawn as 50% thermal probability ellipsoids. All H atoms are omitted and disordered parts are omitted for clarity.

---

[4] A crystal containing compound X was examined on a Bruker APEXII diffractometer with Cu Kα radiation at 100 K. The unit cell was determined to be: monoclinic, $P2_1/n$, a = 11.2738(7) Å, b = 17.7360(16) Å, c = 13.904(3) Å, β = 95.237(4)°, V = 2768.6(6). The structural solution revealed that the crystal contained more than one chemical compound and compositional disorder was observed. The major component of the crystal structure was the desired rhodium(I) complex Rh(dppp)$_2$(CO)$_2$I. Unfortunately, the chemical identity of the other components could not be unequivocally established (but they are likely to be $RhCl_2$ starting material), making the exact composition of the crystal ambiguous. The current structural model has been refined to R1=0.0232 (based on F^2 for I≥2σ), wR2 = 0.0549 (based on F^2 for all data).

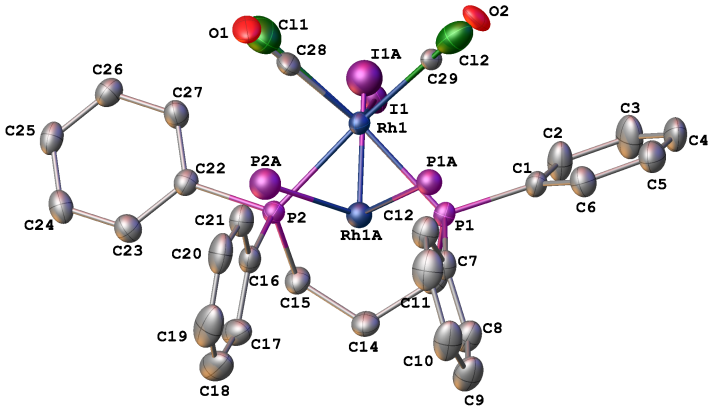

Figure A34. The asymmetric unit of **4-I** showing all disordered parts. All atoms are drawn as 50% thermal probability ellipsoids. All H atoms are omitted for clarity.